

AD-A178 821

PROCESSING STUDIES FOR OPTICALLY TRANSPARENT
LA(2)O(3)-DOPED Y(2)O(3)(U) GTE LABS INC WALTHAM MA
M H RHODES ET AL 31 JUL 86 TR-86-818.1

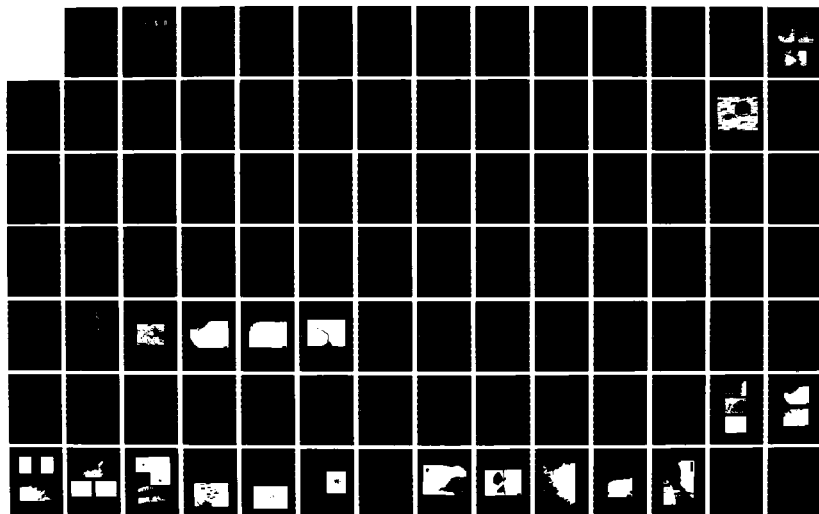
1/2

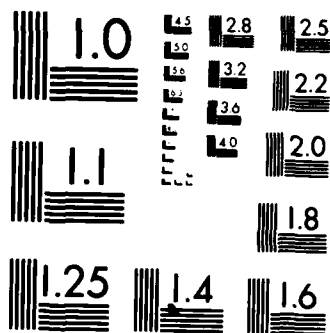
UNCLASSIFIED

N00014-82-C-0452

F/G 20/6

NL





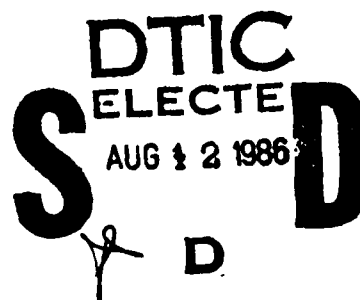
MICROCOPY RESOLUTION TEST CHART
NATIONAL BUREAU OF STANDARDS 1963-A

AD-A170 821

Research and
Development

TR 86-818.1

14



**Processing Studies for Optically
Transparent La_2O_3 -Doped Y_2O_3**

Office of Naval Research
Contract N00014-82-C-0452

Final Report
June 1982 - May 1986

W.H. Rhodes
E.A. Trickett
G.C. Wei

July 31, 1986

Reproduction in whole or in part is permitted for any
purpose of the United States Government.

This document has been approved for public release
and sale; its distribution is unlimited.

GTE Laboratories Incorporated
40 Sylvan Road
Waltham, MA 02254

86 8 12 05 4

GTE

DTIC FILE COPY

Unclassified

SECURITY CLASSIFICATION OF THIS PAGE

AD A170821

REPORT DOCUMENTATION PAGE

1a. REPORT SECURITY CLASSIFICATION Unclassified			1b. RESTRICTIVE MARKINGS		
2a. SECURITY CLASSIFICATION AUTHORITY			3. DISTRIBUTION AVAILABILITY OF REPORT This document has been approved for public release and sale; its distribution is unlimited.		
2b. DECLASSIFICATION/DOWNGRADING SCHEDULE			5. MONITORING ORGANIZATION REPORT NUMBER S. Defense Contract Administration Service Plant		
4. PERFORMING ORGANIZATION REPORT NUMBER(S) TR-86-818-1			7a. NAME OF MONITORING ORGANIZATION Office of Naval Research		
5a. NAME OF PERFORMING ORGANIZATION GTE Laboratories, Incorporated		5b. OFFICE SYMBOL (If applicable)		7b. ADDRESS (City, State and ZIP Code) 800 N. Quincy Street Arlington, VA 22217	
6a. ADDRESS (City, State and ZIP Code) 40 Sylvan Road Waltham, MA 02254		6b. OFFICE SYMBOL (If applicable) Code 614A-PAH		9. PROCUREMENT INSTRUMENT IDENTIFICATION NUMBER N-00014-82-C-0452	
8a. NAME OF FUNDING/SPONSORING ORGANIZATION Office of Naval Research		8b. OFFICE SYMBOL (If applicable) Code 614A-PAH		10. SOURCE OF FUNDING NOS.	
3c. ADDRESS (City, State and ZIP Code) Department of the Navy 800 North Quincy Street Arlington, VA 22217-5000		PROGRAM ELEMENT NO		PROJECT NO	TASK NO
11. TITLE (Include Security Classification) Processing Studies for Optically Transparent La_2O_3 -doped Y_2O_3		13b. TIME COVERED FROM 6/1/82 TO 5/31/86		15. PAGE COUNT	
12. PERSONAL AUTHOR(S) W. H. Rhodes, E. A. Trickett, G. C. Wei		14. DATE OF REPORT (Yr., Mo., Day) July 31, 1986		15. PAGE COUNT	
13a. TYPE OF REPORT FINAL		13b. TIME COVERED FROM 6/1/82 TO 5/31/86		15. PAGE COUNT	
26. SUPPLEMENTARY NOTATION Includes Subcontract Report by Mufit Akinc and Daniel Sordelet, Iowa State Univesity, Ames, Iowa					
17. COSATI CODES			18. SUBJECT TERMS (Continue on reverse if necessary and identify by block number)		
FIELD	GROUP	SUB GR	Powder Synthesis, Yttria, Y_2O_3 , Sintering, Transparent Optical Properties, Mechanical Properties, Infrared Windows, Stoichiometry Control, OH ⁻ absorption, Ion Implantation		
19. ABSTRACT (Continue on reverse if necessary and identify by block number) The processing and properties of La_2O_3 -doped Y_2O_3 were studied with emphasis on increased understanding and control of processing to achieve improved optical and mechanical properties. The program resulted in a successful demonstration of prototype infrared windows. This report is a compilation of the following papers which cover the major findings and accomplishments of this program: "Lanthana-Doped Yttria: A New Infrared Window Material" by W. H. Rhodes, G. C. Wei and E. A. Trickett. "Infrared Transmitting Lanthana-doped Yttria" by E. A. Trickett, W. H. Rhodes, and G. C. Wei.					
20. DISTRIBUTION/AVAILABILITY OF ABSTRACT UNCLASSIFIED/UNLIMITED <input type="checkbox"/> SAME AS RPT <input checked="" type="checkbox"/> DTIC USERS <input type="checkbox"/>			21. ABSTRACT SECURITY CLASSIFICATION Unclassified		
22a. NAME OF RESPONSIBLE INDIVIDUAL Robert W. Schwartz Naval Weapons Center			22b. TELEPHONE NUMBER (Include Area Code) 619-939-1655		22c. OFFICE SYMBOL Code 3854

19. "Effect of point defects on high-temperature properties in transparent polycrystalline lanthana-doped yttria" by G. C. Wei, C. Brecher, and W. H. Rhodes.

"The Mechanical Properties of La_2O_3 -doped Y_2O_3 " by W. H. Rhodes, J. G. Baldoni and G. C. Wei.

"Analytical Microscopy Study of Phases and Fracture in Y_2O_3 - La_2O_3 Alloys" by G. E. Wei, T. Emma, and W. H. Rhodes

"Extrinsic OH^- Absorption in Transparent Polycrystalline Lanthana-doped Yttria" by G. C. Wei.

"Adsorbed Gases As A Source of Residual Porosity in Sintered Transparent Yttria" by Daniel Sordelet, W. H. Rhodes, E. A. Trickett.

"Polycrystalline Oxides for Optical Applications" by W. H. Rhodes.

"Preparation and Characterization of Yttria Monosize Powders" by Mufit Akinc and Daniel Sordelet.

Processing Studies for Optically Transparent La_2O_3 -Doped Y_2O_3

**Office of Naval Research
Contract N00014-82-C-0452**

**Final Report
June 1982 - May 1986**

**W.H. Rhodes
E.A. Trickett
G.C. Wei**

July 31, 1986

Reproduction in whole or in part is permitted for any purpose of the United States Government.

This document has been approved for public release and sale; its distribution is unlimited.

**GTE LABORATORIES INCORPORATED
40 Sylvan Road
Waltham, MA 02254**

FOREWORD

This program has centered on the processing and properties of La_2O_3 -doped Y_2O_3 . The studies dealt with increased understanding and control over processing to achieve improved optical and mechanical properties. It was found that markedly improved mechanical properties were possible, but optical properties were compromised due to scattering from the toughening phase. Trade-off studies identified process schedules and microstructures where some toughening could be retained at little sacrifice to optical properties.

Heat treatment schedules were identified which removed the hydroxol ion from the lattice. This was important in removing a near infrared absorption peak. A second heat treatment cycle was devised to adjust stoichiometry for maximum transmittance and minimum absorption. Processing was scaled from 1 cm diameter discs to discs and complex shapes > 4 cm diameter by pressureless sintering to near net shape.

This final report contains seven new papers dealing with various aspects of this program. In many cases, these are a culmination of four years of research and development. In others, just the last year's research is emphasized. Also included is a short review article on "Transparent Polycrystalline Oxides," which was an invited paper presented at the 20th Anniversary Symposium of the Basic Science Division of the Japanese Ceramic Society in November 1985. Finally, an annual report on a subcontract to produce "Monosize Yttria Powders" by Iowa State University is included.

The following papers have already been published on this topic:

- "Controlled Transient Solid Second-Phase Sintering of Yttria," *J. Am. Ceram.* 64, 144 (1981).
- "Transparent Polycrystalline Yttria for IR Applications," *Proceedings of the 16th Electromagnetic Window Symposium*, Atlanta, Georgia (1982).
- "Progress on Transparent Yttria," *Proceedings of the 17th Electromagnetic Window Symposium*, Atlanta, Georgia (1984).
- "Transparent Polycrystalline Lanthana-doped Yttria," *SPIE 505, Advanced in Optical Materials* (1984).



Accession For	
NTIS	CRA&I <input checked="" type="checkbox"/>
DTIC	TAB <input type="checkbox"/>
Unannounced <input type="checkbox"/>	
Justification	
By	
Distribution /	
Availability Codes	
Dist	Avail and/or Special
A-1	

ACKNOWLEDGMENTS

The authors acknowledge the support of R. Pohanka, the Scientific Officer from the Office of Naval Research, throughout the course of this contract. Appreciation is expressed to R. Thibodeau for his versatility and practical expertise and his invaluable contributions to all aspects of this project. The authors thank B. Hawkins for his assistance in the construction of the high-temperature laser transmittance measuring facility, and the annealing experiments on OH⁻ removal and stoichiometry adjustment. R. Assmus is recognized with thanks for his excellent slip casting and powder preparation techniques. We gratefully acknowledge the technical assistance of T. Emma and K. Ostreicher on the STEM; J. Hefter on SEM; S. Hankin for coordination of materials characterization tasks and transmittance measurement; G. Maklae on the Spark-Source Mass Spectrograph; E. Gutman on ICP, C. Beck on BET; R. Hammond on the FTIR and Lambda-9 Spectrophotometer; G. Werber on Microprobe and SEM; M. Downey and J. Mullins on x-ray; M. Ames on the mass spectrometer; and G. Robinson on ceramographic preparations. Thanks too are expressed to the staff of the Polishing Shop for their invaluable contributions of sample polishing. Grateful appreciation is due to G. Baldoni for his useful discussions on mechanical toughness and the assistance of M. Katsoulakos and W. Van Schalkwyk in making measurements. The authors especially acknowledge the cooperative assistance of V. Meyer and R. Clark at the Technical Assistance Laboratory of GTE Lighting Products Group in obtaining sedimentographic data for this investigation. Gratitude is also expressed to the staff at Union Carbide and Rhone-Poulenc for their continued cooperative excellence. The collaborative studies conducted at Iowa State University have been particularly useful and are included as a chapter. Grateful acknowledgment is also made to H. Bennett, R. Schwartz, D. Burge, and P. Archibald of the Naval Weapons Center for optical characterization and guidance.

TABLE OF CONTENTS

"Lanthana-Doped Yttria: A New Infrared Material," by W.H. Rhodes, G.C. Wei, and E.A. Trickett.

"Infrared Transmitting Lanthana-Doped Yttria," by E.A. Trickett, W.H. Rhodes, and G.C. Wei.

"Effect of Point Defects on High-Temperature Properties in Transparent Polycrystalline Lanthana-Doped Yttria," by G.C. Wei, C. Brecher, and W.H. Rhodes.

"The Mechanical Properties of La_2O_3 -Doped Y_2O_3 ," by W.H. Rhodes, J.G. Baldoni, and G.C. Wei.

"Analytical Microscopy Study of Phases and Fracture in Y_2O_3 - La_2O_3 Alloys," by G.C. Wei, T. Emma, and W.H. Rhodes.

"Extrinsic OH^- Absorption in Transparent Polycrystalline Lanthana-Doped Yttria," by G.C. Wei.

"Adsorbed Gases as a Source of Residual Porosity in Sintered Transparent Yttria," by D. Sordélet, W.H. Rhodes, and E.A. Trickett.

"Polycrystalline Oxides for Optical Applications," by W.H. Rhodes.

"Preparation and Characterization of Yttria Monosize Powders," by Mufit Akinc and Daniel Sordélet.

LANTHANA-DOPED YTTRIA: A NEW INFRARED MATERIAL

by

W.H. Rhodes
G.C. Wei
E.A. Trickett

Lanthana-doped yttria: a new infrared window material

W.H. Rhodes, G.C. Wei, and E.A. Trickett

GTE Laboratories Inc., 40 Sylvan Road, Waltham, Massachusetts 02254

Abstract

Lanthana-doped yttria has a number of favorable intrinsic properties for infrared window applications. La_2O_3 is a sintering aid which makes possible pore-free transparent polycrystalline near-net-shape domes and windows by a unique transient second solid-phase sintering technique. This same second phase can be retained by special anneals to impart mechanical toughening by a second-phase crack-deflection mechanism. Transmission electron microscopy has been utilized to characterize crack deflection and the complex second phase nucleation and growth process. Reduced absorption coefficients have been achieved through improved processing, OH^- removal, and stoichiometry adjustments. The trade-off between mechanical and optical properties has been quantified, and a region of promising compromise identified.

Introduction

Infrared windows with improved optical/thermal/mechanical properties are of interest for advanced applications. La_2O_3 -doped Y_2O_3 is a new transparent polycrystalline window material that offers excellent promise for many of these applications. The long wavelength transmission ($9\text{ }\mu\text{m}$) is among the longest for oxides. This results in low emissivity and tolerance for heating without interference from phonon edge migration. Studies will be reported on lowering the overall absorption and, in particular, a band at $3.1\text{ }\mu\text{m}$. The thermal expansion coefficient is moderate ($8 \times 10^{-6}\text{ }^\circ\text{C}^{-1}$), which favors thermal shock resistance. Other factors such as thermal diffusivity and good mechanical properties are important for thermal shock, rain, and dust-erosion resistance. These are judged to be adequate, and have led to serious efforts to fully develop this material. The mechanical strength and toughness, in particular, are properties in which the unique phase relations available in the La_2O_3 - Y_2O_3 system can be applied to improve properties. Scanning transmission electron microscopy studies, which were used to understand the phases and microstructures, will be presented together with the trade-off relationships between optical and mechanical properties. In addition, ion implantation has been utilized to improve the surface hardness and toughness.

Absorption

The absorption in La_2O_3 -doped Y_2O_3 in the 3.5 to $5.5\text{ }\mu\text{m}$ range can be described by two terms: intrinsic and extrinsic. The relationship between absorption coefficient and wavelength for the recent La_2O_3 -doped Y_2O_3 materials is presented in Figure 1 and illustrates the effect of extrinsic absorption. Theoretically, $\log[\text{absorption coefficient}]$ is proportional to wavelength for wavelengths several times greater than the cutoff wavelength. The straight line in Figure 1 is the experimental data confirming the theoretical linear dependence, and the extrapolation is extended to the 3.5 to $5.5\text{ }\mu\text{m}$ range to obtain the intrinsic absorption coefficient. The extrapolated multiphonon edge shows that the intrinsic absorption coefficient is on the order of 10^{-3} to 10^{-4} cm^{-1} . The actual absorption coefficient in the current materials is typically on the order of 10^{-1} to 10^{-2} cm^{-1} , which is about one to two orders of magnitude higher than the intrinsic absorption. This is caused by extrinsic absorption in the samples. The extrinsic absorption can be due to stoichiometry-related point defects, surface defects, and impurities. All of these are believed to make significant contributions to the total absorption. One major source of the extrinsic absorption is a strong absorption band near 2.7 to $3.5\text{ }\mu\text{m}$, with a peak at $3.08\text{ }\mu\text{m}$ (3246 cm^{-1}).¹ This is indicated by the fact that the absorption coefficient increases significantly as λ approaches $3\text{ }\mu\text{m}$ in stage 2 material. A major effort has been devoted to understanding the cause and removing this absorption peak.

Three stages in this study are shown in the FTIR spectra of Figure 2. Curve (a) of Figure 2 shows a deep band at 3246 cm^{-1} ($3.08\text{ }\mu\text{m}$). A similar absorption band at $3\text{ }\mu\text{m}$ has been reported in single-crystal Y_2O_3 .^{2,3} However, the sources of the absorption peak were not specifically identified. Based on an assumption that the peak was related to OH^- in the crystal lattice, gas exchange experiments were initiated with heavy water (D_2O) and deuterium gas (D_2). Any shift in the absorption peak could be compared to that expected for the mass difference between H_2 and D_2 . Samples having the 3246 cm^{-1} absorption band were heat treated in an atmosphere of D_2 which had been

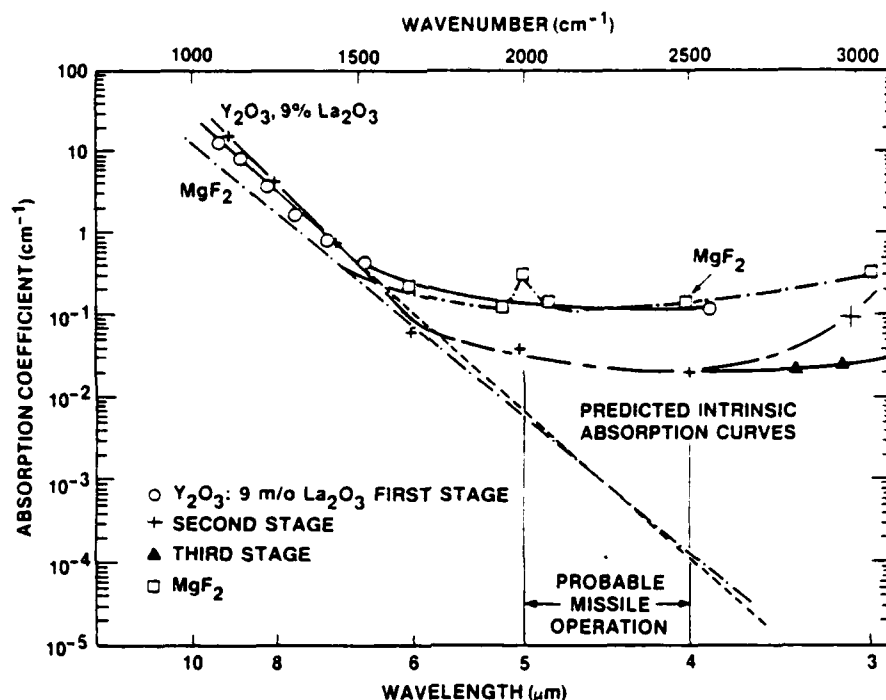


Figure 1. Absorption coefficients of La_2O_3 -doped Y_2O_3 showing three stages of development and comparison with MgF_2 .

bubbled through D_2O at 23°C . The FTIR spectra of such a sample is shown in Figure 2(b). The major absorption peak has shifted from 3246 cm^{-1} to 2420 cm^{-1} . Several side peaks at 2515 cm^{-1} ($3.98\text{ }\mu\text{m}$), 2396 cm^{-1} ($4.20\text{ }\mu\text{m}$), and 2660 cm^{-1} ($3.76\text{ }\mu\text{m}$) were also observed. The shift of the major absorption peak from 3246 cm^{-1} (a factor of 1.34) upon deuteration agrees very well with the theoretical shift. For perfect bond stretching (no mode mixing), the frequency of the OH^- vibration should be, in theory, larger than that of OD^- by a factor of 1.37. The results clearly showed that the $3.08\text{ }\mu\text{m}$ (3246 cm^{-1}) absorption band was due to OH^- rather than oxygen vacancies or some cation impurity center. The side peaks have not been unambiguously assigned. They might be related to the many possible distributions and orientations of OH^- ions in the lattice and interactions with point defects and impurities.

Annealing studies developed cycles that eliminated the absorption peak, as shown in Figure 2(c). The hydrogen defect diffusivity has been determined by an infrared absorbance technique to assist in designing appropriate cycles for various thickness samples. The effect of annealing on absorption at $2.5\text{ }\mu\text{m}$ is shown in Table 1. Obviously, the greatest effect is in the region of $3.08\text{ }\mu\text{m}$, but the absorption band width results in an overall reduction in absorption coefficient.

Another major factor in the overall absorption is stoichiometry. A nonstoichiometric sample has point defects

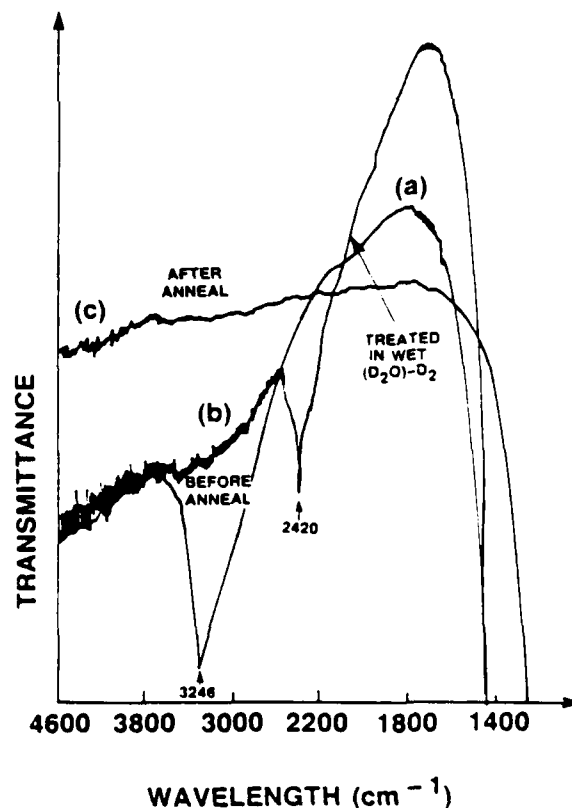


Figure 2. Spectra of 5 mm thick specimens: (a) as-sintered (before anneal); (b) treated in D_2 saturated with 23°C D_2O ; and (c) after anneal to diffuse out defects.

such as O_i'' or V_O which affect the UV band edge and consequently can have a broad effect on absorption. This aspect is discussed separately in this conference.

Table 1
Absorption coefficient (cm^{-1}) at $2.5 \mu\text{m}$ in 2-mm-thick samples

Sample	Preheat Treatment*	Post-Heat Treatment†
YL 213D	0.12	0.05
YL 73CZ	0.15	0.04

*Data from Naval Weapons Center, China Lake, CA, using two-thickness techniques.

†Data obtained at GTE Labs using single-sample technique.

Mechanical properties

The mechanical properties of infrared window materials are important for rain, dust, and thermal-shock resistance. The mechanical strength and fracture toughness are microstructure-dependent properties. This has been a major area of study. Samples quenched from the two-phase cubic plus hexagonal field in the $\text{La}_2\text{O}_3\text{-Y}_2\text{O}_3$ system are fully dense, with a grain size in the 3 to $6 \mu\text{m}$ range. Although this material has the highest strength and toughness, a high concentration of second phase causes considerable scattering. Consequently, it is necessary to find a trade-off between optical and mechanical properties. Alternative methods of strengthening the material without degrading optical properties may be possible. In the former category, trade-off studies were performed versus second-phase concentration. In the latter category, upquench studies were performed to precipitate submicron second-phase particles. In addition, ion implantation of La^{+3} has been attempted to toughen a submicron surface layer.

Several different sintering cycles have been employed to study the effect of second-phase content on fracture toughness. These data have been normalized to single-crystal toughness ($0.9 \text{ MN}\cdot\text{m}^{-3/2}$) and are compared to the model of Faber and Evans⁴ for predicting toughening by crack deflection in Figure 3. The lower bound of the model is for uniform spacing of spheres, while second-phase rods with an aspect ratio of 3 set the upper limit. The data fall between these limits, and appear to vary depending on the process route. The morphology of the second phase also varied with process conditions.

Scanning transmission electron microscopic (STEM) analyses of two-phase samples showed equiaxed cubic matrix and two types of morphology for the intragranular, lathlike, monoclinic, second-phase particles: (1) twinned, Figure 4(a), and (2) untwinned, Figure 4(b). Dark field images of the areas shown in Figures 4(a) and (b) indicated the matrix phase surrounding the second phase to be of the same crystallographic orientation. The lathlike second phase was within a single cubic matrix grain, and, thus, the term "intragranular" was used to describe it. The symmetry of the second phase shown in Figures 4(a) and (b) was identified as monoclinic through selected area electron diffraction and convergent beam electron diffraction analyses. The $(\bar{2}2\bar{2})_c$ and $(402)_m$ planes were approximately parallel in adjacent phases. The twin plane in monoclinic phase was $(313)_m$. Microchemical analyses showed 34 to 38 m/o La_2O_3 in the second phase and 6.1 to 9.1 m/o La_2O_3 content in the cubic matrix. these values

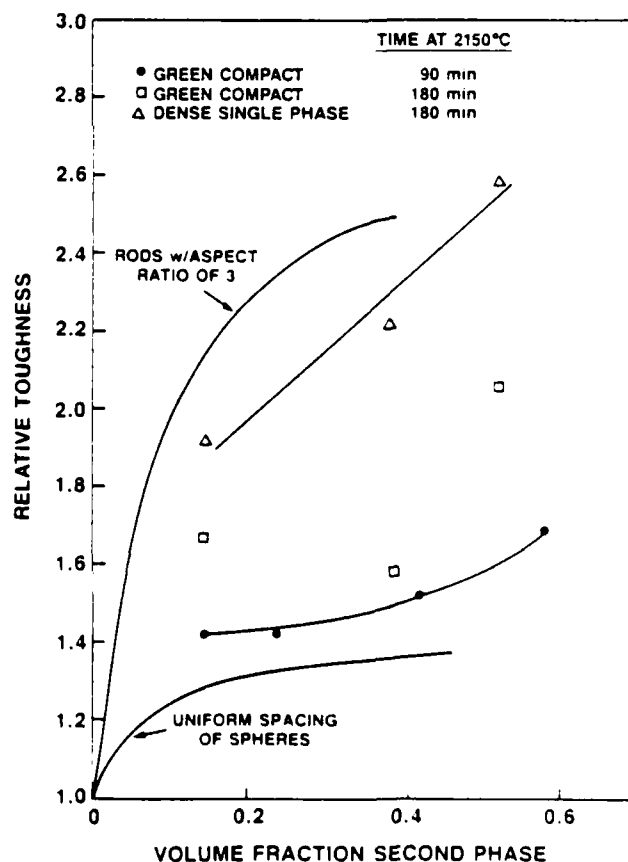


Figure 3. Relative toughness of two-phase material compared with theory of Faber and Evans.

were different from those (27 m/o La_2O_3 and 15 m/o La_2O_3) indicated in the equilibrium phase diagram, suggesting the development of nonequilibrium compositions in cooling or adjustments to the phase boundaries of the C and H phase fields.

In-situ STEM fracture experiments were conducted on two-phase specimens. Figure 5 illustrates the interaction of a matrix cubic-phase crack with the intragranular monoclinic second phase. The crack has deflected around the second phase due to the strain field surrounding this phase. The strain field results from thermal expansion and/or elastic modulus mismatch between the phases. Deflection of the crack around the second-phase particles increases the crack length and, therefore, consumes the excess energy associated with breaking atomic bonds over the straight crack path. This energy can be sufficient to halt the crack propagation prior to catastrophic failure. As noted in Figure 3, the relative toughening depends on sample history. This appears to correlate with the morphology of the second phase with the greater toughening being associated with rod- or plate-like second phases.



Figure 4(a). Bright-field TEM micrograph showing twinned intragranular second phase.



Figure 4(b). Bright-field TEM micrograph showing untwinned intragranular second phase.



Figure 5. TEM micrograph showing crack deflection at second-phase/matrix interface.

The trade-off between optical and mechanical properties has been studied in a number of ways. One controlled experiment is shown in Figure 6. Samples 2 mm thick were annealed at intervals above and below the phase boundary. The specular transmittance and indentation fracture toughness were measured on polished and strain-relieved discs. The discs were then thinned to 1 mm and remeasured for transmittance. The toughness is highest for the two-phase microstructure, but transmittance is degraded due to refraction from the high concentration of second phase. As the phase boundary is approached, the second-phase concentration decreases due to the lever rule controlling the phase content. The transmittance rises rapidly without significant loss in toughness. A suggested phase boundary is indicated in Figure 6, which agrees quite well with the published diagram.⁵ It is interesting to note that the toughness appears to remain near the level of the two-phase structures, slightly below the presumed phase boundary. The mechanism for this apparent toughening is not known, but it may be associated with grain size. Samples annealed farther below the phase boundary have larger grain sizes. Transmittance is 2%–4% below the maximum and theoretical value (82.1% at $2.5\ \mu\text{m}$) for these partially toughened microstructures. This trade-off in optical properties for improved mechanical properties may prove viable in the application of this material.

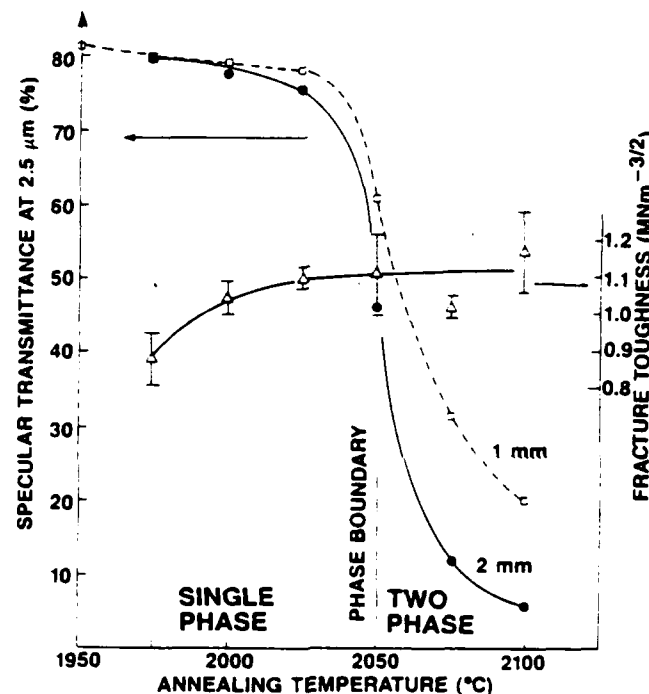


Figure 6. Effect of annealing temperature on transmittance and toughness.

Surface strengthening

Many ceramics and glass components have been strengthened by surface treatments. In most cases, the surface has been placed in a permanent compressive stress state. Since this class of material is stronger in compression than tension, the compressive stress provides a margin which must be overcome by applied tensile stress before failure occurs. This concept has been adapted to La_2O_3 -doped Y_2O_3 through experimentation with pack cementation, solution dipping, and ion implantation. This latter method proved most successful. Polished specimens were implanted* with La ions at an energy of 195 to 200 keV perpendicular to the sample surface. A La ion beam of $75\ \mu\text{A}$ was aimed at the target chamber using LaCl_3 salt as the source material in conjunction with an Ar/Cl_2 carrier gas. The ion beam was stationary and the samples, mounted on a mechanical assembly, were transported across the beam numerous times to attain the required fluence.

*Spire Corporation, Bedford, MA.

The evaluation of the effect of implantation on mechanical properties was difficult because of the extremely thin affected layer. A 50-nm penetration was calculated, which may in turn affect the structure of a somewhat deeper layer, especially after annealing. The crack-indentation technique was employed to measure the effect of implantation on mechanical properties. Light loads of 25 and 50 g were used in an attempt to characterize the surface. The results are reported in Table 2. The hardness data was separated by indentation load and combined (shown in the table), and no reliable trend was revealed. The fracture toughness is shown together with a crack-length parameter employed in calculating toughness. This crack-length parameter, which is a normalized measure of crack propagation distance, is smaller for the tougher samples. Both the fracture toughness and crack parameter indicate that the implanted surfaces have improved properties. The standard deviations overlap the nonimplanted surfaces in several cases, so the value of the implantation cannot be concluded forcefully based on these tests. Additional tests will be required to conclusively prove the value of ion implantation. Other methods of affecting a deeper surface layer may be required to build a sufficiently high compressive stress to significantly influence mechanical properties.

Table 2
Mechanical properties of implanted yttria

Property	Sample 192J		Sample 221M	
	Implanted Side	Nonimplanted Side	Implanted Side	Nonimplanted Side
Treatment	$10 \times 10^{16} \text{ La/cm}^2$	None	$10 \times 10^{16} \text{ La/cm}^2$ and annealed	Annealed
Hardness (MN/m ²)	$10,407 \pm 297$	$12,375 \pm 2011$	$11,434 \pm 1730$	$11,329 \pm 937$
K_{IC} (MN/m ^{3/2})	1.19 ± 0.14	0.97 ± 0.10	1.06 ± 0.05	0.95 ± 0.02
Crack parameter ($1 + C_L/2\bar{D}$)	2.09 ± 0.16	2.57 ± 0.23	2.28 ± 0.21	2.54 ± 0.24

Surface treatment can affect optical properties in several ways. The La ion implantation disturbed local stoichiometry, resulting in a dark surface film which reduced transmission by several percent. Post-implantation anneals returned the samples to the colorless condition, but some loss of transmission remained. Composition or strain changes at the surface will also affect the local refractive index, resulting in an optical component with nonuniform optical properties. In certain cases, this may be intolerable to the optical design.

Conclusions

Polycrystalline La₂O₃-doped Y₂O₃ has been developed for optical applications. Low absorption coefficients have been achieved through improved processing, identification and removal of OH⁻ defects, and stoichiometry adjustments. Mechanical strengthening and toughening has been realized through controlled second-phase precipitation. STEM studies have identified the mechanism of toughening to be crack deflection around the monoclinic second-phase particles. Studies have shown the trade-off between optical and mechanical properties, and have identified a microstructure where 2%–4% loss of transmission is accompanied by 20% improvement in toughness. These samples are a fine-grain, single-phase material. This trade-off may prove viable for many optical applications. Some surface strengthening was realized by La ion implantation. The effect was small, and further testing is required to prove the usefulness of this treatment. The processing, properties, and development of La₂O₃-doped Y₂O₃ has progressed significantly toward the infrared-window application.

Acknowledgment

This work was partially supported by the Office of Naval Research. We thank the many contributors from GTE, especially R. Thibodeau, R. Assmus, B. Hawkins, and G. Baldoni. The optical characterization studies by the Naval Weapons Laboratory under H. Bennett and D. Burge were invaluable.

REFERENCES

1. "Processing Studies for Optically Transparent La_2O_3 -doped Y_2O_3 ," W.H. Rhodes, E.A. Trickett, and G.C. Wei, GTE Labs Technical Report No. TR 84-818.1 (July 1984).
2. "Measurements of the Optical Constants of Yttrium Oxide," Y. Nigara, *Jpn. J. Appl. Phys.* 7, pp. 404-408 (1968).
3. "Infrared Transmittance of Crystalline Yttrium Oxide and Related Compounds," K.A. Weckersheim and R.A. Leferer, *J. Opt. Soc. Am.* 51, p. 1147 (1961).
4. "Crack Deflection Processes — I. Theory," K.T. Faber and A.G. Evans, *Acta Metal.* 31, p. 565 (1983).
5. "High Temperature Equilibria in the System La_2O_3 - Y_2O_3 ," J. Coutures and M. Foex, *J. Solid State Chem.* 11, pp. 194-300 (1974).

INFRARED TRANSMITTING LANTHANA-DOPED YTTRIA

by

E.A. Trickett
W.H. Rhodes
G.C. Wei

INFRARED TRANSMITTING LANTHANA-DOPED YTTRIA

E.A. Trickett, W.H. Rhodes, G.C. Wei, and D. Sordelet*

GTE Laboratories Incorporated
40 Sylvan Road
Waltham, MA 02254

ABSTRACT

Improved materials are needed for infrared windows. Lanthana-doped yttria is a leading candidate due to its long wavelength cutoff ($9\text{ }\mu\text{m}$) and its excellent high-temperature properties (M.P. 2464°C). This material is fabricated from powders by a unique transient solid second-phase sintering technique. The second phase can be removed through annealing for single-phase highly transmitting material. Near-net-shape fabrication of domes or plates is achieved by pressureless sintering. Residual porosity has been traced in part to the presence of adsorbed gases which are not removed by calcination or prefiring. Removal of these gases by tailored sintering schedules has resulted in reduced absorption. Further optical property improvement has been accomplished by anneals to remove OH^- from the lattice.

INTRODUCTION

The long wavelength cutoff ($9\text{ }\mu\text{m}$) and low emissivity of lanthana-doped yttria are characteristics which indicate an ideal development material for infrared windows. Samples are fabricated from powders by a unique transient solid second-phase sintering technique¹ which presents several advantages over HIPing or other consolidation methods in that it produces near-net-shape products and also presents the possibility of mechanical toughening.² Figure 1 illustrates the close geometrical relationship between the sintered piece and the polished dome, which is highly favorable for economic fabrication and finishing costs. Other advantages of the lanthana-doped yttria are numerous. The cubic crystal structure makes possible a high-transmittance polycrystalline material; it has excellent high-temperature properties (M.P. 2464°C) and a moderate expansion coefficient ($8 \times 10^{-6}^{\circ}\text{C}^{-1}$).

EMITTANCE AND ABSORPTION

The long wavelength cutoff of La_2O_3 -doped Y_2O_3 results in little overlap of the elevated temperature spectral radiosity curve and hence also results in low emittance. Obviously the low-emittance characteristics favorably influence the hot transmission. In addition, the phonon edge is known to move to shorter wavelengths as a material is heated. Lanthana-doped yttria has a greater tolerance for heating than other ceramics, e.g., Al_2O_3 . The absorption edge of this material is very close to that of MgF_2 (Figure 2). It is interesting to note that the intrinsic absorption curves

* Present address: Iowa State University, Materials Science and Engineering Department, Ames, IA, 50011.

for MgF_2 and La_2O_3 -doped Y_2O_3 are nearly equivalent, and that the extrinsic data for improved yttria is significantly lower than the state-of-the-art MgF_2 infrared material; however, in initial research specimens, the absorption coefficient was close to that of MgF_2 . Subsequent stages of research have effectively lowered the absorption of the Y_2O_3 material. The improvement is a result of the process refinement. Further, the extrinsic absorption included a strong absorption band at $3.08 \mu\text{m}$. Deuteration experiments and the absorption band shift unequivocally identified this band to be due to the stretching-mode vibration of OH^- impurities. Elimination of this band and the accompanying decrease in absorption coefficient was accomplished by appropriate annealing schedules.³ Both the one- and two-sample methods have been employed in calculating the absorption coefficient. The two-sample technique gives more accurate values, making it possible to measure levels below 0.05 cm^{-1} . Table I shows samples which demonstrate low absorption with a minimum effect of impurities and only moderate interference from OH^- and stoichiometry. Nevertheless a marked reduction in absorption is observed after OH^- removal in samples 73CZ and 213D. This low absorption leads to transmittance close to the estimated theoretical value. Using a measured refractive-index value of 1.9699³ to account for the Fresnel losses, the calculated theoretical transmittance is 80.7% at $0.546 \mu\text{m}$. Based on the dispersion relationship reported for pure yttria,⁴ the theoretical transmittance of La_2O_3 -doped Y_2O_3 was estimated as 82.1% at $2.5 \mu\text{m}$, 82.3% at $3.0 \mu\text{m}$, and 83.1% at $5 \mu\text{m}$.

TABLE I. Absorption coefficient (cm^{-1}) in selected samples

WAVELENGTH $\lambda (\mu\text{m})$	YL 107C YL 107D	YL 73CZ YL 73CW	YL 73CZ		YL 213D	
2.0	0.21	0.12	0.12	0.05*	0.15	0.04*
2.5						
3.0	0.18	0.18				
3.8						
4.0	0.02	0.08				
5.0	0.04	0.09				
6.0	0.06	0.16				
7.0	0.76					
8.0	3.91					
9.0	14.30					

* OH^- removed — single sample technique.

GAS DESORPTION/POROSITY STUDIES

Optical microscopic observation shows that some fine porosity in samples has remained to impair the optical parameters. As with other ceramics, powder processing procedures are of extreme importance in accomplishing the ultimate goals of consolidation and sintered properties. Even small levels of porosity will induce scattering and interfere with UV and VIS transmittance. Total integrated scatter measurements indicate that the fraction of scattered light increases with decreasing wavelength and that the scattering site is on the order of $0.64 \mu\text{m}$ or smaller. One possible explanation for retained porosity is the desorption and entrapment during final sintering of gases that are not completely removed during calcining and pre firing. The origin of these gases could be incomplete calcination, hydration and conversion to carbonate prior to pressing, binders,

and/or liquid media pickup during wet processing. The addition of binder systems is often necessary to aid compaction, reducing the tendency for cracking and improving packing uniformity in the compact. In general ceramists believe that high-temperature calcining or air prefiring removes these gases. It was hypothesized that this may not be the case for ceramics in which optical clarity and complete pore removal are desired. Experiments were conducted to study binder-free lanthana-doped yttria desorption during the early stages of processing. In this study three powders were compacted and then individually analyzed at several temperatures by both mass spectrometry and thermal gravimetric analysis. A high surface area ($43 \text{ m}^2/\text{g}$) material served as the control powder. The effects on gas desorption of ball milling and/or calcining at 1000°C were determined after compaction and analyses in the mass spectrometer.

The analysis was accomplished in the following manner. The compacted sample was stored at 200°C until ready for analysis to avoid atmospheric gas pickup. It was then placed in a side arm of a quartz oven attached to the mass spectrometer. While the sample was isolated from the heat, the oven was heated to 1000°C and then cooled to 400°C , at which time a blank analysis of the oven and entire system was taken. The sample was then introduced into the 400°C oven, and after equilibration the desorbed gas pressure was measured and then introduced into the mass spectrometer for quantitative analysis. After evacuating the collection system from the previous analysis, the temperature was then raised to the next level of interest. The system was allowed to equilibrate and the evolved gases were again measured. This procedure was repeated at 200°C temperature intervals to 1000°C .

Surprisingly, the study shows that residual gases remain even after a 1000°C calcination of the powder and a subsequent 1200°C prefire of the compact. Figure 3 shows the gases desorbed from a sample of binder-free unmilled powder which had been calcined at 600°C . Also shown are the methane gases which result when the powder is (a) ball milled in organic liquid or when b) the powder is calcined at 1000°C to reduce the surface area to $11.6 \text{ m}^2/\text{g}$ and then ball milled. The highest gas level of these residuals was observed in the high surface area ball-milled sample, as would be expected. The lowest gas content was observed in the low surface area ball-milled sample, indicating that either a) a portion of the gases remaining on the standard powder were removed in the 1000°C calcine prior to milling and that the milling did not appreciably increase the overall gas levels or b) the surface reactivity of the high surface area powder with its environment results in higher gas adsorption.

The total measured gas pressures from the three green compacts and their prefired counterparts are compared in Figure 4. Considerable gas is removed by the 1200°C prefire, but it becomes obvious that not all volatiles are removed from precursor powders during calcination or prefiring at 1200°C .

Organic milling aids were determined to be the source of the CH_4 which was observed in milled samples. The higher surface area powder adsorbed the most liquid, and much of it remained after a 200°C drying step; some of it was retained at temperatures far above those characteristic of physically adsorbed species. Desorption of CH_4 at 600°C suggests chemical bonding of liquid media organics to the powder during milling. Because the CH_4 remains after a 1200°C prefiring, and partial sintering at 1500°C (Figure 5), it is believed that the presence of other gases is the result of incomplete burnout during firing and not due to resorption during cooling and storage. Between 70% and 98% of the gases produced in three green compacts proved to be CO_2 . This may be attributed to either decomposition of any precursor not totally converted during calcination or adsorption of CO_2 and/or formation of carbonates during exposure to air.

Water observed between 600°C and 800°C even after the 1500°C sinter was at higher temperatures than would be expected for the loss of chemical water and may indicate complex gaseous thermodynamic and kinetic relationships. The T.G.A. results supported the validity of the individual mass spectrometer experiments. A separate study of atmospheric moisture adsorption determined that there is apparently a stronger tendency for the powder to hydrate than to combine with CO₂ to form carbonate. In conclusion, nonoxidized species resulting from incomplete calcination as well as adsorbed species during processing can remain as residual porosity and scattering sites in the final sintered product.

Sintering studies have shown that a consideration of these gas desorption findings can result in considerable adsorbed gas removal and markedly lower porosity. Table II shows the effect of both prefire and sintering on several compact thicknesses. Little or no measurable improvement in transmittance is observed in 1-mm or 2-mm-thick samples by increasing the length of prefire at a given temperature or by changing the sintering rate and/or holding at a suitable temperature to allow for gas desorption and diffusion. However in 6-mm-thick samples given a short prefire, transmittance is increased from 39.3% at 1.0 μ m and 64.9% at 2.5 μ m to 74.8% and 78.4% by slowing the rate of sintering and incorporating a suitable hold at temperature. Under these conditions there is a further increase in transmittance when the prefire is increased. A long prefire and a rapid sintering regime gave 49.8% transmittance at 1.0 μ m and 68.3% at 2.5 μ m; whereas an identical prefire and slow sintering regime, including a hold for gas diffusion, produced 75.7% at 1.0 μ m and 79.3% at 2.5 μ m. Clearly, when large samples are carefully and slowly sintered to avoid shrinkage stress cracking, a benefit of the slow sintering regime is masked. Even slower sintering may be a prerequisite to producing transmittant materials with intrinsic properties.

TABLE II. Effect of prefire and sintering on transmittance

Sample Ref. No.	Thickness (mm)	Prefire	Sinter Heating Rate	Intermediate Hold	Transmittance		α at 2.5 μ m
					1.0 μ m	2.5 μ m	
332B	1	Short	Fast	No	80.8	82.7	0
332J	1	Long	Fast	No	81.2	82.6	0
332N	1	Long	Slow	Yes	79.6	81.6	0.06
332C	2	Short	Fast	No	81.2	82.4	0
332I	2	Long	Fast	No	77.4	81.4	0.04
332O	2	Long	Slow	Yes	78.1	80.4	0.11
332D	6	Short	Fast	No	39.3	64.9	0.39
332H	6	Long	Fast	No	49.8	68.3	0.31
332P	6	Short	Slow	Yes	74.8	78.4	0.08
332Q	6	Long	Slow	Yes	75.7	79.3	0.06

The hot isostatic pressing (HIP) technique is a method of consolidation which is often employed to eliminate the last residual porosity in metals or ceramics. Experiments were conducted to determine if this technique could improve the optical properties of La₂O₃-doped Y₂O₃. Preliminary work showed that HIPing fully sintered single-phase 50 μ m grain size material did not improve transmittance nor eliminate scattered porosity or pore nests. It was reasoned that the grain size was too large for differential creep to be effective in pore elimination for the process conditions employed. Therefore a series of samples were sintered at one of four different times in

the two-phase field. Grain sizes ranged from 1 to 8 μm , and densities from 99.2% to 99.6% of theoretical for the two-phase structures. HIP runs that contained one sample from each sintering time were conducted. The residual porosity was completely entrapped, so the specimen acted as its own container; the isostatic pressure promoted further densification. Various times, temperatures, and pressures were explored in the single-phase field. The transmittances of polished specimens 1-mm thick were measured between 0.3 μm and 3.2 μm . The best sample from each starting series is reported in Table III. Three different HIP cycles are represented in this table, indicating that the optimum HIP cycle depends on the starting microstructure. A control sample which was pressureless sintered by a standard cycle resulted in 79.4% transmittance at 1 μm and 81.3% transmittance at 2.5 μm with a 44 μm grain size. Thus the HIP process is capable of achieving transmittances at 2.5 μm (and presumable beyond) which are equal to or better than that achieved in pressureless sintered material. In general the transmittance at 1 μm and below is lower for HIP samples, indicating that there is a population of fine porosity. It was originally thought that this particular microstructural feature could be improved upon or eliminated by HIPing over pressureless sintering. In conclusion, it appears that samples with excellent infrared properties can be produced by HIP; visible transmittance is inferior, however, and it is not clear that there is an overall advantage of HIPing over pressureless sintering.

TABLE III. Transmittance of hot isostatically pressed La_2O_3 -doped Y_2O_3

Grain Size		Specular Transmittance	
Starting (μm)	Final (μm)	1 μm (%)	2.5 μm (%)
1	54	63.7	80.9
2	37	54.2	79.0
6	38	73.1	81.2
8	43	71.1	82.9

DIELECTRIC CONSTANT

Some applications require both infrared and radio-frequency transmittance. The dielectric constant and loss will govern the suitability of Y_2O_3 for this multimode application. Table IV shows data measured at the MIT Laboratory for Insulation Research⁵ on pure, moderately dense Y_2O_3 , and measurements on the La_2O_3 -doped material at GTE.

TABLE IV. Dielectric properties of yttria at ambient temperature

Frequency	97% Dense Pure Y_2O_3		100% Dense 0.09 La_2O_3 - 0.91 Y_2O_3	
	Dielectric Constant	Loss Factor	Dielectric Constant	Loss Factor
10 ³	11.1	0.012	12.2	<0.0001
10 ⁵				
10 ⁶				
10 ¹⁰	11.1	0.0045		

The measurements were performed on electroded samples. The dielectric constant of this material is obviously high, but the low loss factor indicates it may have applicability for dual-mode applications.

CONCLUSIONS

Due to its intrinsic properties, La_2O_3 -doped Y_2O_3 continues to show promise as an infrared material. A versatile sintering process and significant strides in the understanding of powder processing and impurity removal have produced discs and domes with optical properties closer to intrinsic than previously reported. Ongoing modification to all aspects of processing promises even further improvement.

In addition, excellent infrared properties can be produced by hot isostatic pressing; however, samples to date have inferior visible transmittance. Pressureless sintering and powder studies may lead to information which can be translated into better HIP results, but at this time there appears no overall advantage over pressureless sintering.

ACKNOWLEDGMENTS

This work was partially supported by the Office of Naval Research. We thank the many contributors from GTE, especially R. Thibodeau, R. Assmus, B. Hawkins, M. Ames, and F. Avella. The optical characterization studies by the Naval Weapons Laboratory under H. Bennett and D. Burge were invaluable.

REFERENCES

1. "Continued Transient Solid Second Phase Sintering of Yttria," W.H. Rhodes, *J. Am. Cer. Soc.* 64, No. 1, pp. 13-19 (1981).
2. "Second Phase Toughening in Y_2O_3 - La_2O_3 System," W.H. Rhodes and J.G. Baldoni, *Ceramic Bulletin*, 64, No. 3 (1985).
3. "Transparent Polycrystalline Lanthana-Doped Yttria," W.H. Rhodes, E.A. Trickett, G.C. Wei, *SPIE Vol. 505, Advances in Optical Materials*, pp. 9-14 (1984).
4. "Measurement of the Optical Constants of Yttrium Oxide," Y. Nigara, *Jpn. J. Appl. Phys.* 7, pp. 404-408 (1968).
5. "Dielectric Constant and Loss Data," W.B. Westphal and A. Sils, AFML-TR-72-39.

TABLES

Table I. Absorption coefficient (cm^{-1}) in selected samples

Table II. The effect of prefire and sintering on transmittance

Table III. Transmittance of hot isostatically pressed La_2O_3 -doped Y_2O_3

Table IV. Dielectric properties of yttria at ambient temperatures

FIGURES

Figure 1. Prototype infrared domes, showing near-net-shape sintered dome on right and polished dome on left.

Figure 2. Absorption coefficients of La_2O_3 -doped Y_2O_3 at initial, intermediate, and current stage of development.

Figure 3. Mass spectrometer analysis of gas desorption from green compact.

Figure 4. Comparison of gas pressure/g vs temperature of green and 1200°C prefired compacts.

Figure 5. Gas evolution from prefired Sample C after partial sinter to 1500°C .

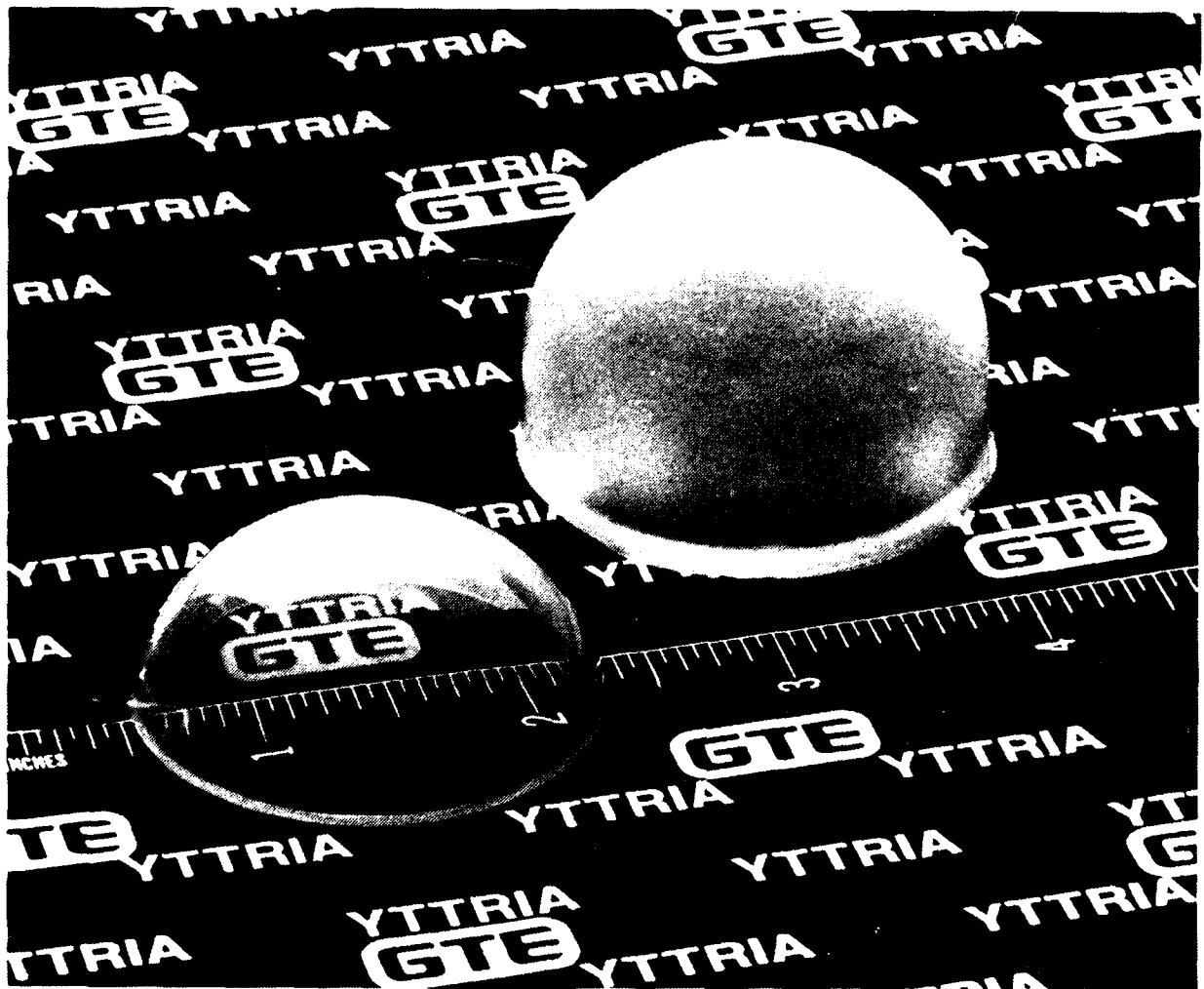


Figure 1. Prototype infrared domes, showing near-net-shape sintered dome on right and polished dome on left.

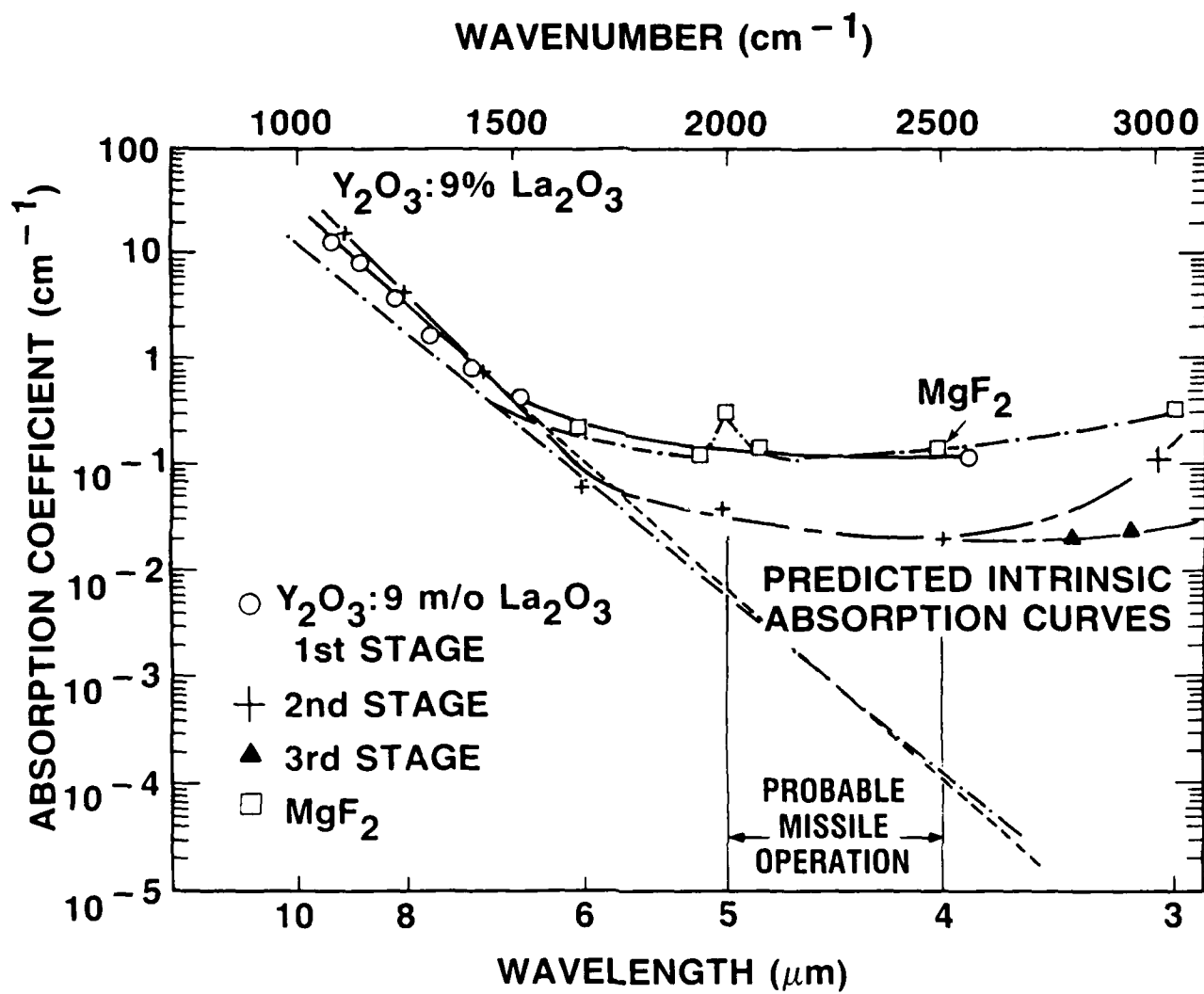


Figure 2. Absorption coefficients of La₂O₃-doped Y₂O₃ at initial, intermediate, and current stage of development.

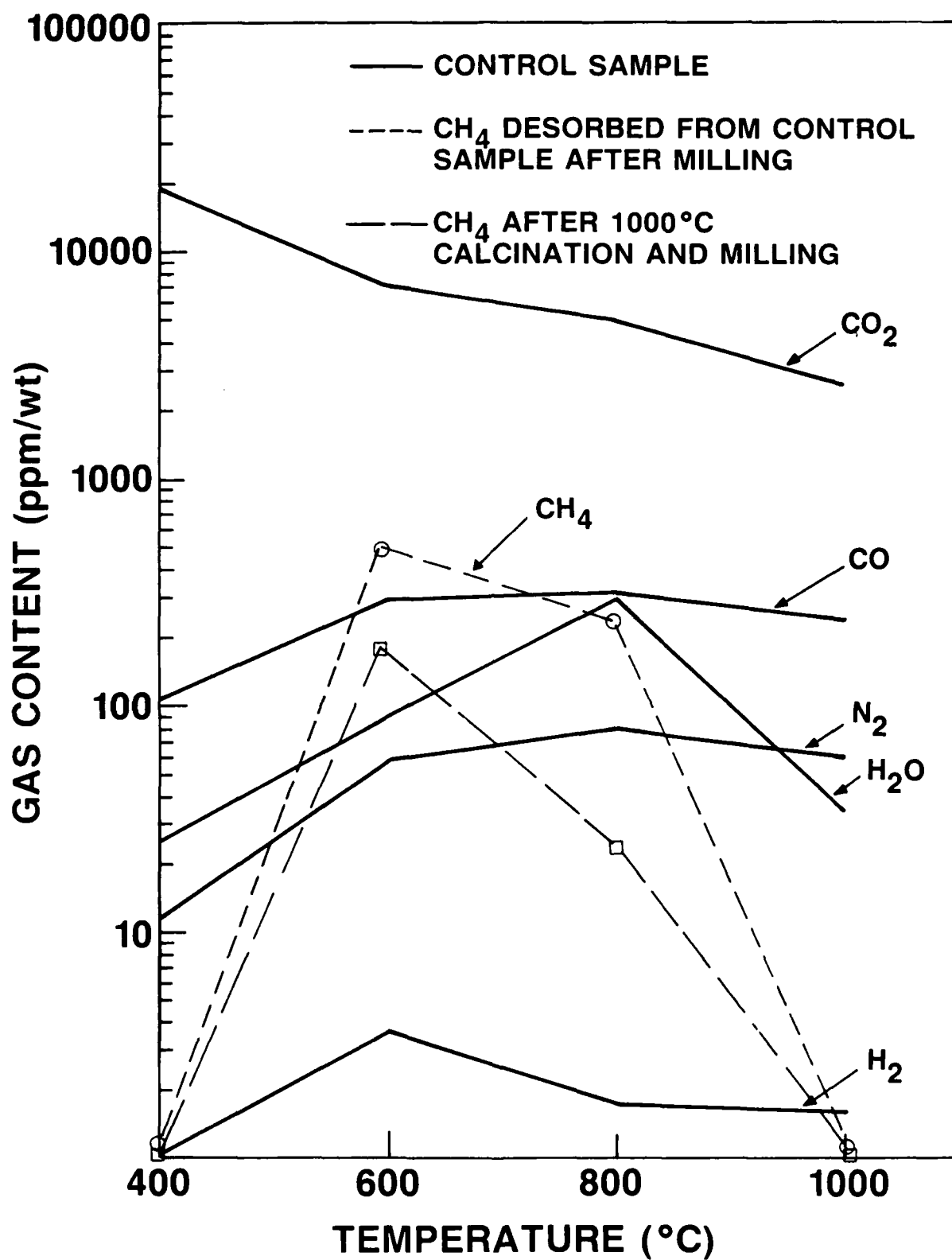


Figure 3. Mass spectrometer analysis of gas desorption from green compact.

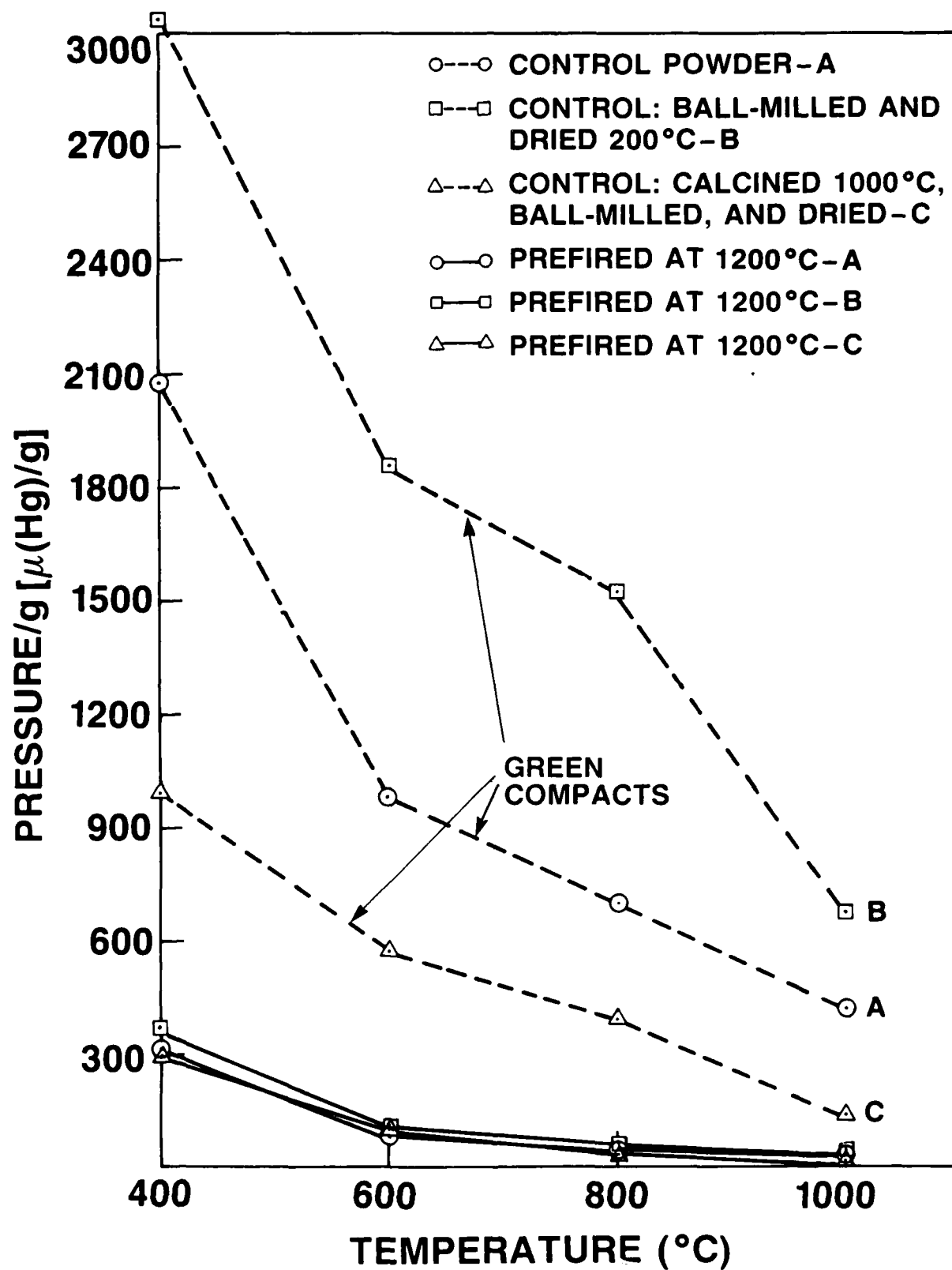


Figure 4. Comparison of gas pressure/g vs temperature of green and 1200°C prefired compacts.

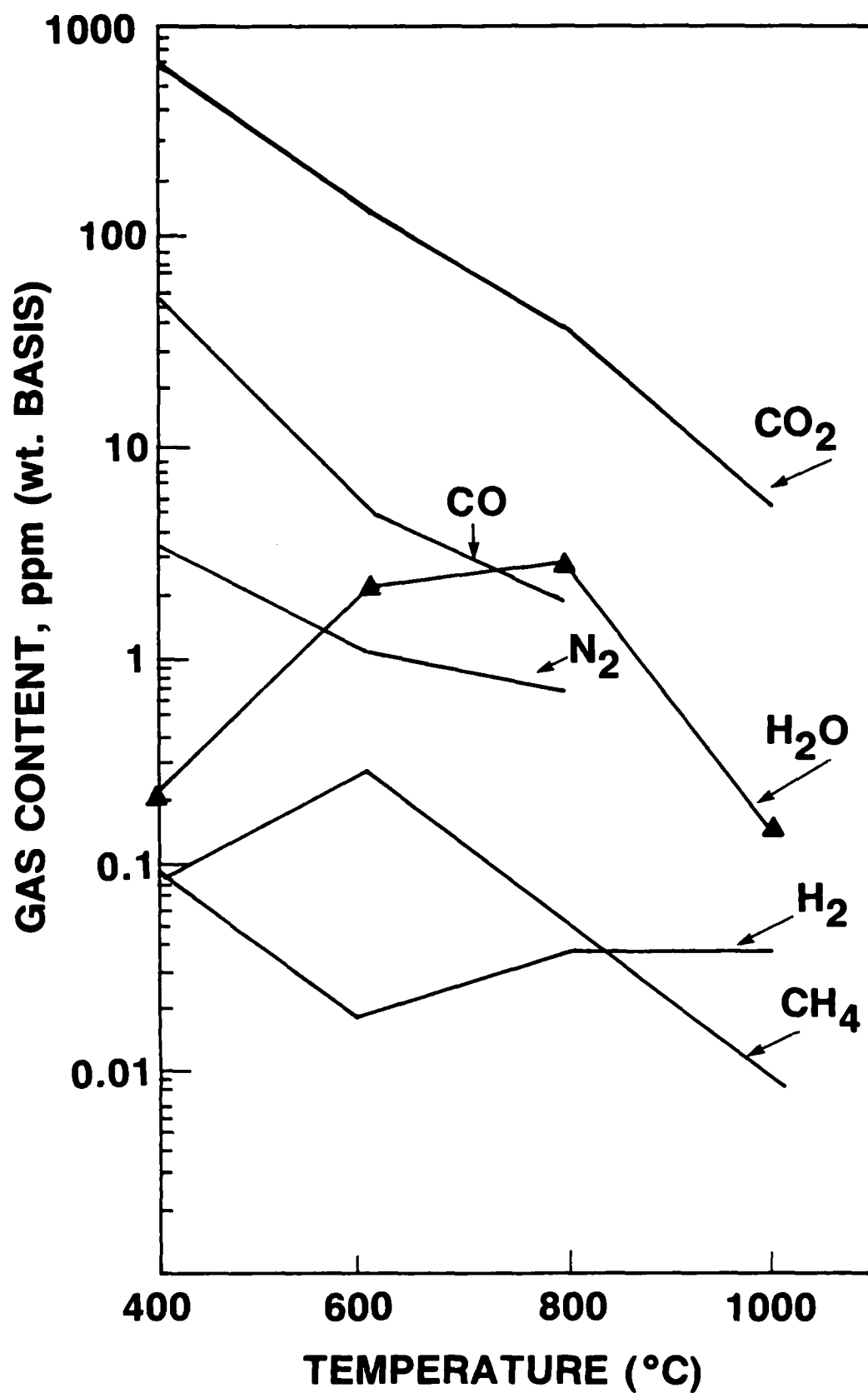


Figure 5. Gas evolution from prefired Sample C after partial sinter to 1500°C.

**EFFECT OF POINT DEFECTS ON HIGH-TEMPERATURE
PROPERTIES IN TRANSPARENT POLYCRYSTALLINE
LANTHANA-DOPED YTTRIA**

by

G.C. Wei
C. Brecher
W.H. Rhodes

**EFFECT OF POINT DEFECTS ON HIGH-TEMPERATURE
PROPERTIES IN TRANSPARENT POLYCRYSTALLINE
LANTHANA-DOPED YTTRIA**

by

G.C. Wei
C. Brecher
W.H. Rhodes

Effect of point defects on high-temperature optical properties in transparent polycrystalline lanthana-doped yttria

G.C. Wei, C. Brecher, and W.H. Rhodes

GTE Laboratories Inc., 40 Sylvan Road, Waltham, Massachusetts 02254

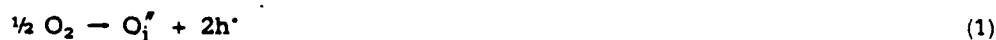
ABSTRACT

The effect of point defects on absorption in transparent polycrystalline lanthana-doped yttria was investigated by measuring the absorption coefficient as a function of temperature and oxygen partial pressure P_{O_2} at two wavelengths (0.357 and 3.39 μm). The composition of the specimens was controlled by preannealing at 1400°C in appropriate oxygen pressures ranging from 10^{-16} to 10^{-5} atm. The technique used for determining the absorption coefficient consisted of measuring the transmittance of two samples of different thicknesses. The absorption at 0.357 μm showed a sharp increase with temperature beginning at about 1000°C. The magnitude of this increase was a function of P_{O_2} . A broad minimum was found in the high-temperature absorption at 1400°C, ranging from 10^{-13} to 10^{-10} atm P_{O_2} ; this represents the stoichiometry range. Initial absorption measurements in the infrared (3.39 μm) indicated much less temperature dependence, with little or no absorption increase above 1000°C at 3×10^{-13} atm P_{O_2} and only a small increase at 2×10^{-3} atm P_{O_2} . Also reported in this paper are other optical properties, including refractive index, temperature coefficient of refractive index, and scattering in lanthana-doped yttria.

INTRODUCTION

Transparent lanthana-doped yttria fabricated by transient solid second-phase sintering is a candidate infrared window material.¹ High-temperature optical properties in lanthana-doped yttria, including absorption, refractive index, scattering, and multiphonon edge shift, are important parameters for processing and design considerations.

The effect of temperature and stoichiometry on visible (0.6328 μm) He-Ne laser transmittance in La_2O_3 -doped Y_2O_3 was previously investigated.² Temperature and oxygen partial pressure were found to affect the transmittance significantly. The results were interpreted in terms of stoichiometry. Studies in the literature on the electrical and optical properties of pure yttria³⁻⁵ and Nd-doped yttria⁴ showed Frenkel disorders on the oxygen sublattice as the principal defects. The same type of defects are believed to be the dominating point defects in La_2O_3 -doped Y_2O_3 . Oxygen interstitials (O_i'') are created in oxidizing atmospheres, while oxygen vacancies ($\text{V}_\text{O}^{\bullet\bullet}$) are produced in reducing environments through the following reactions:



The oxygen vacancies and interstitials can have multiple valences on the gain or loss of an electron or hole. They can act as donors or acceptors of electrons in the crystal. The energy of an electron in the valence band can, for example, be elevated to that of an acceptor defect, or an electron from a donor defect can be elevated to the conduction band. These transitions in La_2O_3 -doped Y_2O_3 can cause strong UV absorption bands that would tail off far into the infrared range.

La_2O_3 -doped Y_2O_3 is transparent from about 250 nm to 9 μm at room temperature. In 1-mm-thick samples sintered in wet hydrogen, the uncoated UV (350 nm) transmittance values ($\approx 75\%$) are close to those ($\approx 80\%$) in the infrared range (3 μm), with the difference attributed to surface and bulk scattering and nonstoichiometry-related absorption. Figure 1 shows the transmittance curve throughout the entire spectrum of 200 nm to 3200 nm.

The band gap is 5.5 eV. The sharpness of the electron transition edge in the UV range is affected by absorption related to nonstoichiometry and by scattering related to residual pore and surface defects. The UV and visible spectra of La_2O_3 -doped Y_2O_3 treated in strongly oxidizing or reducing environments show broad electron transition edges in contrast to the relatively sharp edge near 300 nm typically observed in samples sintered and annealed in wet hydrogen. This indicates that the broad, stoichiometry-related absorption bands are at, near to, or shorter than 300 nm wavelength. Therefore, transmittance of the UV light (0.357 μm) in La_2O_3 -doped Y_2O_3 should be a sensitive measure of the absorption caused by the point defects.

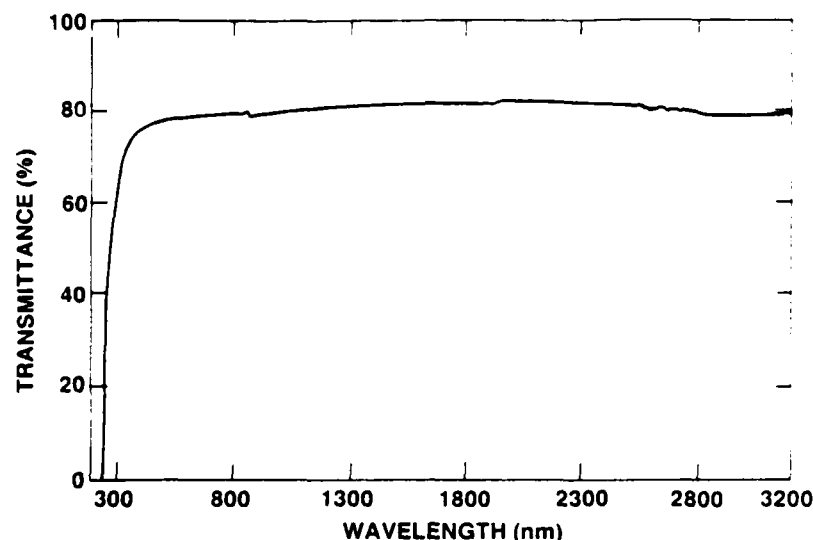


Figure 1. Transmittance in 1-mm-thick sample vs wavelength from 200 to 3200.

A high-temperature laser absorption measuring facility using the UV emission ($0.357 \mu\text{m}$) from an argon ion laser and the infrared emission ($3.39 \mu\text{m}$) from an He-Ne laser was established at GTE Labs. The methodology of the experiments on the high-temperature laser absorption measuring facility was basically the same as that of the previous experiments using the $0.6328 \mu\text{m}$ He-Ne laser. The objective was to conduct transmittance/stoichiometry experiments using more sophisticated instrumentation along with the Ar UV laser and He-Ne infrared laser for greater accuracy in order to obtain a thorough understanding of the stoichiometry-related absorption. The goal was to develop procedures of controlled P_{O_2} treatment to achieve the intrinsic absorption.

EXPERIMENTAL PROCEDURE

An optical diagram of the high-temperature laser absorption measuring system is shown in Figure 2. Absorption and transmittance can be measured by passing two beams through two samples of different thicknesses at normal incidence for several laser wavelengths extending from the ultraviolet to the infrared. The light sources included: (1) an Ar laser which produces 100 mW at 0.351 to $0.364 \mu\text{m}$, 1.3 W at $0.4880 \mu\text{m}$, and 1.7 W at $0.5145 \mu\text{m}$; and (2) an He-Ne laser which produces 15 mW at 632.8 nm , 2.5 mW at $1.15 \mu\text{m}$, and 5 mW at $3.39 \mu\text{m}$. Photomultipliers and pyroelectric detectors were employed. A light chopper, a beam splitter, along with a detector (D1), provided a reference signal to which all transmittance data were referenced. Two samples of different thicknesses (2 mm and 1 mm) were placed in a sample holder located in the center of the furnace. The furnace was an alumina tube furnace heated by globar elements and having a maximum temperature of 1500°C . Quartz windows were used for the furnace. Detectors (D2 and D3) received the specularly transmitted light beams. The output signals of these detectors were fed to lock-in amplifiers which were locked to the frequency of the chopper for signal averaging and noise reduction. Filters and apertures were placed in front of the detectors (D2 and D3) to minimize furnace radiation into the detectors. This resulted in moderate transmitted signals, but the effects of temperature and atmosphere were still observable. Transmittance in the two samples at room temperature was measured on a Perkin-Elmer Lambda-9 spectrophotometer (300 nm – 3200 nm) prior to placing the samples into the furnace. The transmitted signals from the detectors (D2 and D3) were normalized to the the spectrometer transmittance to obtain the transmittance values (T_1 and T_2) for use in Equations (3) and (4).

$$T_1 = \frac{(1 - r - s)^2 \exp(-\alpha d_1)}{1 - s^2 r^2 \exp(-2\alpha d_1)} \quad (3)$$

$$\frac{T_1}{T_2} = \exp[-\alpha(d_1 - d_2)] \cdot \frac{1 - s^2 r^2 \exp(-2\alpha d_2)}{1 - s^2 r^2 \exp(-2\alpha d_1)} \quad (4)$$

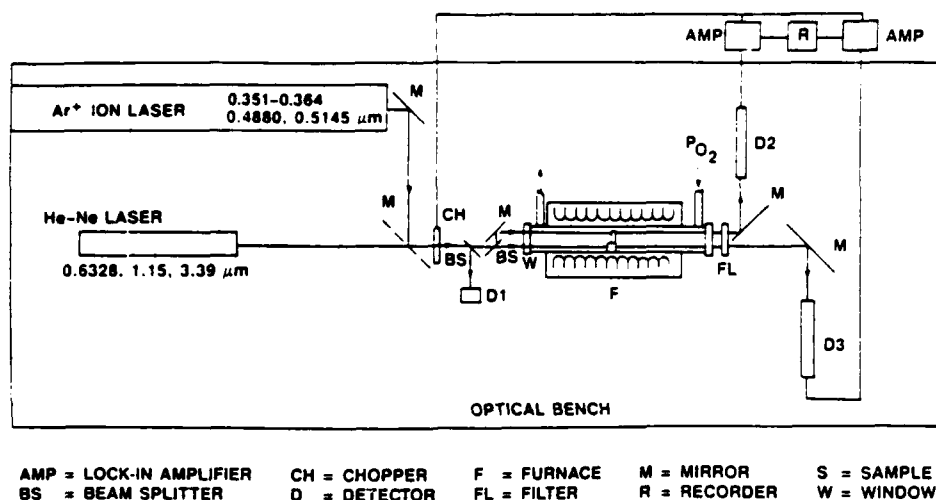


Figure 2. High-temperature laser transmittance/absorption measurement apparatus.

where T_1 = transmittance in the thick sample, T_2 = transmittance in the thin sample, r = reflectivity = $(n-1)^2/(n+1)^2$, n = refractive index, α = absorption coefficient, d_1 = thick sample thickness (2 mm), d_2 = thin sample thickness (1 mm), and s = surface scattering.

The above equations were used in calculating the absorption coefficient and surface scattering at various temperatures and under various P_{O_2} . The calculation involved an iterative computer fit of Equations (3) and (4) to solve for α and s .

In the course of the laser absorption experiments, it was discovered that the fringes in the transmitted signals, obtained in the cooling cycle along with the known thermal expansion of La_2O_3 -doped Y_2O_3 ($8.0 \times 10^{-6}/^\circ C$) and sample thickness, could be used in deriving the temperature coefficient of the refractive index. A recent measurement on La_2O_3 -doped Y_2O_3 found the refractive index at room temperature to be 1.9699 at 546.1 nm, and the room-temperature refractive indices (Figure 3) at 1, 2.5, 3, and 5 μm were estimated to be 1.935, 1.914, 1.907, and 1.872, respectively, by using the dispersion relationship for Y_2O_3 .⁶

Prior to each laser absorption experiment for a specific P_{O_2} , samples were preannealed at 1400°C under the appropriate P_{O_2} , and then lightly polished to remove thermal etching. These samples were single-phase, cubic, 9 mol % La_2O_3 -doped Y_2O_3 . The preanneal treatment was necessary to bring the defects in the samples into equilibrium with the annealing P_{O_2} . An annealing time of 3 hr was used because of the following. It was found that 88 hr would be required to convert a 5-mm-thick black La_2O_3 - Y_2O_3 prepared under dry H_2 to transparency by annealing at 1400°C in Ar-5 ppm O_2 . A color boundary diffusion front was observed to migrate about 1.3 mm (x) in the first 4 hr (t) anneal. This color boundary migration indicated a defect diffusivity ($D = x^2/4t$) of $2.9 \times 10^{-7} cm^2/s$, in good agreement with the literature value ($1.8 \times 10^{-7} cm^2/s$ at 1400°C).⁷ Thus an anneal time of 3 hr would be sufficient for defect equilibrium at 1400°C in samples with thickness up to 2 mm.

Each laser absorption run consisted of (1) purging the furnace with the appropriate gas at room temperature for 30 min, (2) adjusting the gas flow to 100 cc/min and heating the samples from room temperature to 1400°C in about 2 hr, (3) holding the temperature at 1400°C for 10 min, and (4) decreasing the furnace power and allowing the samples to cool to room temperature in 5 hr.

Samples were removed and repolished between runs. The following gases were used for the designated P_{O_2} (at 1400°C): Ar-5 ppm O_2 ($P_{O_2} = 5 \times 10^{-6}$ atm), $CO/CO_2 = 1/2$ (1×10^{-8} atm), $CO/CO_2 = 2/1$ (5×10^{-10} atm), $CO/CO_2 = 100/1$ (3×10^{-13} atm), wet Ar-8% H_2 with 23°C dew point (5×10^{-11} atm), wet H_2 with 23°C dew point (3×10^{-13} atm), wet H_2 with 6°C dew point (3×10^{-14} atm), and dry H_2 (10^{-16} atm).

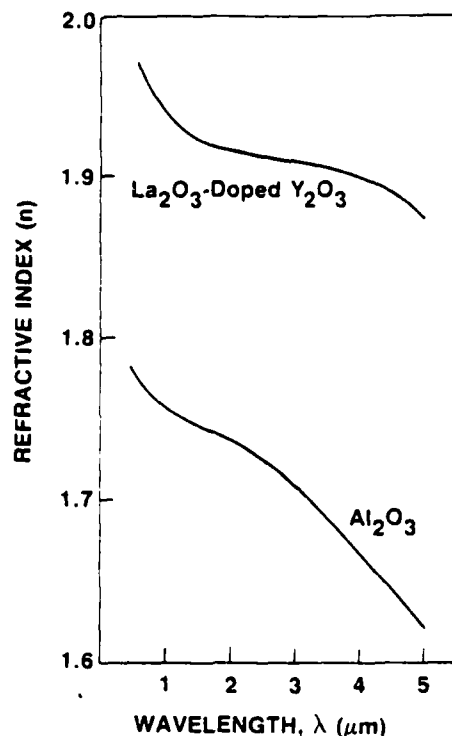


Figure 3. Refractive index vs wavelength at room temperature.

RESULTS AND DISCUSSION

Absorption at $0.357 \mu\text{m}$

The results of experiments at $0.357 \mu\text{m}$ showed strong effects of temperature and P_{O_2} on transmittance. Rapid increases in transmittance were observed during 1400°C isothermal anneals when the atmosphere was altered from air to Ar-5 ppm O_2 , from pure O_2 to dry H_2 , and from Ar-5 ppm O_2 to wet H_2 . The transmittance at $0.357 \mu\text{m}$ in the single-phase cubic La_2O_3 -doped Y_2O_3 samples generally decreased with increasing temperature above about 1000°C . Figure 4 shows absorption coefficient at $0.357 \mu\text{m}$ as a function of temperature in wet Ar-8% H_2 atmosphere. The onset of absorption increase was at about 1000°C . The absorption coefficient increased from 0.5 cm^{-1} at room temperature to 11.6 cm^{-1} at 1400°C (see Figure 4). The onset temperature for UV absorption increase in La_2O_3 -doped Y_2O_3 was about the same (1000°C) for all the gases used. The 1400°C absorption in single-phase, cubic, La_2O_3 -doped Y_2O_3 under various P_{O_2} atmospheres ranged from 11 to 13 cm^{-1} , a factor of 22 to 26 higher than the room-temperature values. Variation of band gap with temperature could account for part of the absorption at high temperatures. The increase in absorption with increasing temperature above 1000°C is thought to be largely due to stoichiometry-related absorption.

The heating and cooling portions of the curves in Figure 4 were transient phenomena in terms of defect equilibration. The 1400°C absorption, however, represented equilibrium values, since the samples were preannealed under the appropriate P_{O_2} . The relationship of the equilibrium 1400°C absorption vs P_{O_2} is shown in Figure 5. There was a broad region in the curve at $\text{P}_{\text{O}_2} = 10^{-13}$ to 10^{-10} atm, where absorption was at a minimum and the material was considered to reach the stoichiometric composition. Reproducibility in the measurement of 1400°C absorption was reasonable ($\pm 0.2 \text{ cm}^{-1}$), about 15% of the total range of the stoichiometry effect. Absorption increased in both the high and low P_{O_2} region as the defect concentration and deviation from stoichiometry increased. This is consistent with the proposed point defect structure consisting of oxygen vacancies ($\text{V}_{\text{O}}^\bullet$) and interstitials (O_{I}'').

The results indicated that optical absorption in single-phase cubic La_2O_3 -doped Y_2O_3 caused by O_{I}'' and $\text{V}_{\text{O}}^\bullet$ could be improved by annealing in the range of $\text{P}_{\text{O}_2} = 10^{-13}$ to 10^{-10} atm. The residual absorption at the stoichiometric composition was probably due to equilibrium concentrations of Frenkel defects pairs ($\text{V}_{\text{O}}^\bullet$ and O_{I}'').

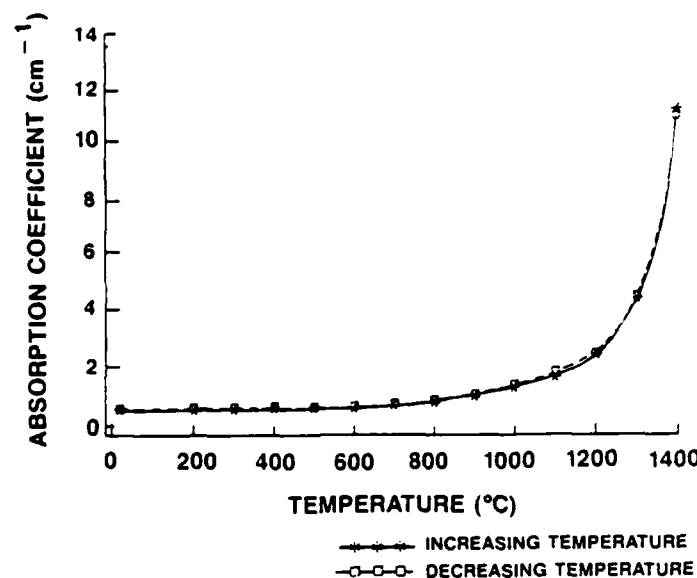


Figure 4. High-temperature UV (357 μm) absorption in La_2O_3 -doped Y_2O_3 .

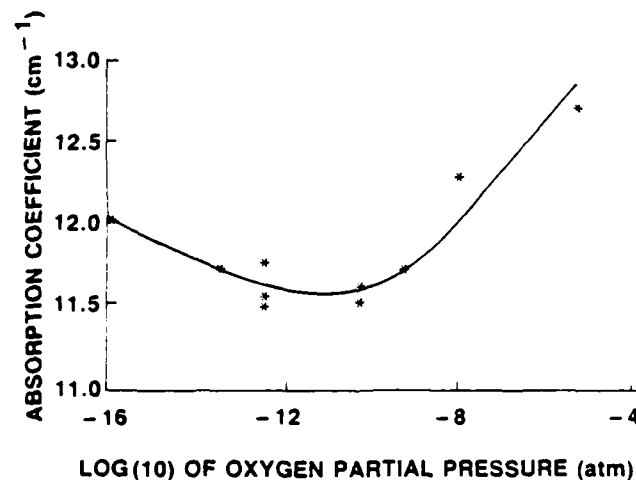


Figure 5. Dependence of 0.357 μ absorption coefficient in La_2O_3 -doped Y_2O_3 at 1400 °C upon P_{O_2} .

Oxygen self diffusivity (D^*) in pure Y_2O_3 in air was measured as $1.0 \times 10^{-11} \text{ cm}^2/\text{s}$ by Ando et al.⁸ This coupled with an oxygen defect diffusivity ($D_{\text{d}} = 2.9 \times 10^{-7} \text{ cm}^2/\text{s}$, discussed earlier) indicated an oxygen defect concentration ($C_{\text{d}} = D^*/D_{\text{d}}$) of 34 ppm. The weight gain ($\approx 10^{-4}$ fraction) during an Ar-5 ppm O_2 anneal (88 hr) of one sample that was prepared under dry H_2 indicated an oxygen defect concentration of 27 ppm. The defect concentration level is slightly higher than the concentrations of aliovalent impurities such as Si^{4+} , Fe^{2+} , Ca^{2+} , Na^{+1} , and Cl^{-1} . Thus, the Y_2O_3 - La_2O_3 is probably in the intrinsic range at 1400 °C, where the concentration of the predominant point defect is largely determined by P_{O_2} .

The curves of 1400 °C absorption coefficient vs $\log P_{\text{O}_2}$ were qualitatively similar to the 1400 °C transmittance (0.6328 μm) results obtained in the previous study² and the room-temperature curves of absorption coefficient (at 1.08 and 0.4 μm) vs P_{O_2} obtained by Tsuiji et al.³ in pure Y_2O_3 . The previous study² showed a 1400 °C stoichiometry

point at $\sim 10^{-9} - 10^{-10}$ atm P_{O_2} . Tsuiki et al constructed the Kroger-Vink diagram based on the results of their studies on optical absorption (at 1.08 and 0.4 μm) and electrical conductivity in pure Y_2O_3 . They showed that the stoichiometric composition in pure Y_2O_3 and 1 m/o Nd-doped Y_2O_3 at 1450°C were near $P_{O_2} = 10^{-9.2}$ and $10^{-7.5}$ atm, respectively. The present results are generally consistent with the results of previous work² or the study by Tsuiki et al.³

Absorption at 3.39 μm

Initial measurements were performed on the transmittance and absorption in La_2O_3 -doped Y_2O_3 as a function of temperature using the 3.39 μm He-Ne laser. Two atmospheres including $CO/CO_2 = 100/1$ ($P_{O_2} = 3 \times 10^{-13}$ atm at 1400°C) and Ar-1% air (2×10^{-3} atm P_{O_2}) were used in the experiments. The effect of temperature appeared to be smaller than was found at 0.357 μm . Little or no increase in the absorption at 3.39 μm at temperatures up to 1400°C was found in $P_{O_2} = 3 \times 10^{-13}$ atm, and a small but definite increase was observed in $P_{O_2} = 2 \times 10^{-3}$ atm at temperatures above 1000°C. This is a subject of continuing study, and the results on the 3.39 μm absorption will be completed with additional experiments.

Scattering

Scattering in two as-sintered and polished disks (2 mm thick) was measured at the Naval Weapons Center (NWC), China Lake, CA. The total integrated scattering ranged from 2% to 5% at 0.6471 μm and 0.6% to 1% at 3.39 μm . These samples were annealed at 1000°C in Ar-1 ppm O_2 to remove OH⁻ absorption at 3.1 μm . The scattering in the annealed and repolished samples was measured. There was no change in scattering at the short wavelength (0.6471 μm) or in the infrared range (3.39 μm) upon the anneal.

Surface scattering at 0.357 μm calculated from Equations (3) and (4) was on the order of 5%-10% at room temperature and 10%-15% at 1400°C. The surface scattering was not related to bulk stoichiometry. The relatively high surface scattering in the samples used in the laser absorption experiments occurred because these two samples were only lightly polished (<40 μm removal) to conserve thickness rather than subjected to the regular procedure of mirror/window polishing. The surface scattering in the samples used in the laser experiments increased with increasing temperature primarily because of increase in refractive index.

Temperature Coefficient of Refractive Index

As described in the Experimental Procedure section, the fringes (due to interference in the samples) shown in the transmitted signals obtained in the cooling cycle of the laser absorption/stoichiometry experiments can be used to calculate the temperature coefficient of the refractive index. The results indicated a temperature coefficient of $50 \times 10^{-6}/^\circ\text{C}$ at 0.357 μm and $23 \times 10^{-6}/^\circ\text{C}$ at 3.39 μm (Figure 6).

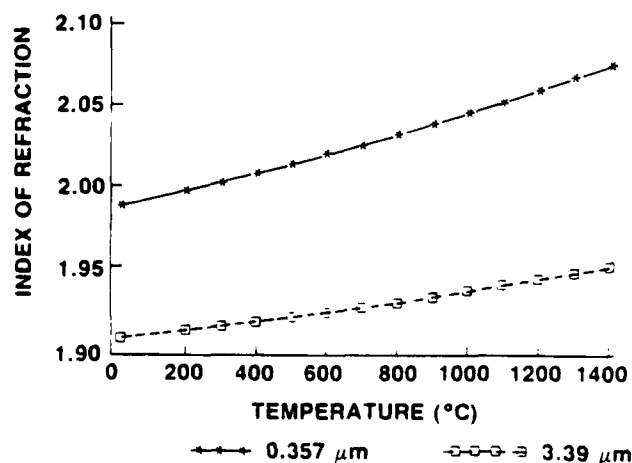


Figure 6. Temperature dependence of index of refraction in lanthana-doped yttria.

SUMMARY AND CONCLUSIONS

In summary, high-temperature controlled atmosphere studies showed the 1400°C absorption (0.357 μm) reached minimum in a region near $P_{\text{O}_2} = 10^{-13}$ to 10^{-10} atm. where the material was considered to have attained stoichiometric composition. When La_2O_3 -doped Y_2O_3 was annealed in an oxidizing atmosphere, $\text{O}_i^{\cdot\cdot}$ were created, while $\text{V}_{\text{O}}^{\cdot}$ were created in a reducing atmosphere. These defects gave rise to absorption. The concentrations of these defects could be minimized by annealing the single-phase La_2O_3 -doped Y_2O_3 in an appropriate P_{O_2} so that the composition was brought to the stoichiometry composition. Infrared absorption at 3.39 μm showed little or no increase at temperatures up to 1400°C under $P_{\text{O}_2} = 3 \times 10^{-13}$ atm.

REFERENCES

1. W.H. Rhodes, G.C. Wei, and E.A. Trickett, "Lanthana-Doped Yttria: A New Infrared Window Material," *SPIE Proc.* this issue.
2. W.H. Rhodes, E.A. Trickett, and G.C. Wei, "Transparent Polycrystalline Lanthana-Doped Yttria," *SPIE Proceedings* 505, San Diego, CA, pp. 9-14 (1984).
3. H. Tsuiki, T. Masumoto, K. Kitazawa, and K. Fueki, "Effect of Point Defects on Laser Oscillation Properties of Nd-Doped Y_2O_3 ," *Jpn. J. Appl. Phys.* 21, (7) pp. 1017-1021 (July 1980).
4. N.M. Tallen and R.W. Vest, "Electrical Properties and Defect Structure of Y_2O_3 ," *J. Am. Ceram. Soc.* 49, p. 401 (1966).
5. P. Odier and J. Loup, "An Unusual Technique for the Study of Nonstoichiometry: The Thermal Emission of Electrons. Results for Y_2O_3 and TiO_2 ," *J. Solid State Chem.* 34, pp. 107-119 (1980).
6. Y. Nigara, "Measurement of the Optical Constants of Yttrium Oxide," *Jpn. J. Appl. Phys.* 7, (4) pp. 404-408 (1968).
7. M.B. Berard, C.D. Wirkus, and D.R. Wilder, "Diffusion of Oxygen in Selected Monocrystalline Rare Earth Oxides," *J. Am. Ceram. Soc.* 51, p. 643 (1968).
8. K. Ando, Y. Oishi, and H. Hase, "Oxygen Self-Diffusion in Single Crystal Y_2O_3 ," *J. Am. Ceram. Soc.* C-222 (1983).

THE MECHANICAL PROPERTIES OF La_2O_3 -DOPED Y_2O_3

by

W.H. Rhodes
J.G. Baldoni
G.C. Wei

THE MECHANICAL PROPERTIES OF La_2O_3 -DOPED Y_2O_3 *

W.H. Rhodes, J.G. Baldoni, and G.C. Wei
GTE Laboratories Inc.
40 Sylvan Road, Waltham, MA 02254

I. INTRODUCTION

La_2O_3 -doped Y_2O_3 is sintered to full density by a controlled transient solid second-phase sintering technique.¹ High density and optical clarity is achieved by sintering in a solid, two-phase cubic (C) plus hexagonal (H) phase field and subsequently annealing at a lower temperature where the equilibrium structure is single-phase C for compositions between 0 and ~14 m/o La_2O_3 . The H phase is effective in retarding grain growth due to the Ostwald ripening mechanism controlling growth. Apparently, pores remain on grain boundaries until they are eliminated by the normal diffusional processes.

A variety of pore-free microstructures are attainable within this system. Quenching from the two-phase field produces varying concentrations and morphologies of the second phase, depending on starting composition and temperature. Single-phase structures with grain sizes from 10–200 μm can be produced by varying the annealing time. Dense, single-phase samples that are subsequently heat treated and quenched from the two-phase field develop different structures compared to those sintered and cooled directly from the two-phase field.

Samples cooled from the C + H field were found to be C plus monoclinic (M), which is expected for a displacive transformation of the H phase. It was of interest to determine whether this transformation was capable of toughening yttria in an analogous manner to partially stabilized zirconia. The fracture toughness data were also compared with other models to explain the observations.

*Presented at the Annual Meeting of the American Ceramic Society, May 8, 1985, Cincinnati, Ohio (Basic Science Session, Fracture II 175-B-85).

The presence of second phase in a transparent medium is known to scatter light from multiple refraction events. The degree of scattering depends on both the size of the second-phase particles and the wavelength of light, and is governed by the Raleigh scattering law. The interrelationships between toughening, second-phase contents, and optical properties were also considered in this study.

Several previous studies have dealt with various mechanical properties of yttria. Monroe and Smyth² studied the grain-size dependence of fracture energy for 96%–98% dense sintered pure Y_2O_3 by the notched-beam test. The maximum fracture energy (5.17 J/m^2) occurred at a grain size of $30 \mu\text{m}$ and then decreased slowly to 3.79 J/m^2 for the $115 \mu\text{m}$ grain-size material. Tani, et al.³ carried out similar studies on HIPed $>98.7\%$ dense pure Y_2O_3 by the indentation method. They demonstrated almost no effect of grain size on fracture toughness over the $0.2\text{--}10.0 \mu\text{m}$ range, with a slight decline (from $\sim 2.0 \text{ MNm}^{-3/2}$ to $1.6 \text{ MNm}^{-3/2}$ at grain sizes of 160 to $214 \mu\text{m}$). Rice, et al.⁴ studied fracture energy/flaw size/grain size relationships in ThO_2 -doped Y_2O_3 by both fractographic and the applied-moment double-cantilever beam (DCB) technique. They showed that fracture energy rose from 1 J/m^2 to about 7 J/m^2 , with an increasing flaw/grain size ratio from 0.15 to 10 . This was interpreted in terms of a transition from single-crystal fracture energy to polycrystalline fracture energy. It was also shown that preferred cleavage occurred in $[111]$ for single crystals. They also performed three-point bend tests and reported strengths of 207 MPa and 161 MPa for $15 \mu\text{m}$ grain-size specimens which were ground parallel and perpendicular to the tensile axis, respectively.

II. EXPERIMENTAL PROCEDURE

Concentrations of 8 to 16 m/o La_2O_3 were added to Y_2O_3 * by dissolving 99.99% pure oxides in HNO_3 and coprecipitating with $\text{H}_2\text{C}_2\text{O}_4$. After washing, drying, and screening, the

*Rhône-Poulenc Industries, Paris, France, and MolyCorp Inc., Lavoisier, Colorado. Coprecipitated oxides were also supplied by both companies.

mixture was calcined at 1000°C for 1 hr. The powder was pressed into either a rod or disk shape at 103 to 345 MPa by double-acting uniaxial or isostatic pressing. After prefiring in air for 1 hr at 1000°C to 1300°C, the specimens were sintered in a W-mesh resistance furnace* in controlled atmospheres, starting with dry H₂ and shifting to 23°C dew-point H₂ to ensure a near-stoichiometric final specimen. The heating and cooling rate was 2200°C/hr. Sintering was accomplished in the two-phase C + H field, most commonly near 2150°C, where 10–60 v/o H phase was in equilibrium with the C solid solution. Samples were converted to single-phase C by annealing between 1300–2020°C in 23°C dew-point H₂ for times ranging from 10 to 300 min. Some single-phase C samples were rapidly heated (at 420°C/min) into the C + H field, held for 1–300 min, and quenched at 210°C/min to ambient temperature. Representative microstructures for the various heat treatments are shown in Figure 1.

The densities were close to theoretical (at least 99.9%) for all specimens tested. Deviations from theoretical were characterized by measuring specular transmittance between 0.3 and 3.0 μm .[†] Residual porosity was the primary source of transmittance loss in single-phase samples, whereas samples heat-treated or quenched from the two-phase field had, in addition, scattering from the H (M) phase.

Microstructures were examined on quenched, slow-cooled, and annealed samples after sectioning, polishing, and etching with boiling 20% HCl. Grain intercept lengths were measured by counting the grain boundaries, intersected by random straight lines of known length. The reported grain sizes are the average intercept length times 1.5.

STEM analyses[‡] were performed on ion-beam thinned specimens coated with carbon. In-situ fracture analysis was performed with a tensile stage employing a dogbone specimen with a hole in the thinned central region. Microchemical analysis was performed by analytical electron microscopy.

*Centorr Associates, Soncock, New Hampshire.

†Perkin-Elmer Lambda 9.

‡Philips EM400T STEM.

Strength was determined by four-point bending on specimens $0.127 \times 0.254 \times 2.54$ cm exposed to air for 23°C tests and Ar for elevated-temperature tests. Samples were ground with a 320-grit diamond wheel parallel to the tensile axis and annealed at 1000°C for 1 hr in air before testing. The cross-head speed was 0.05 cm/min. Most of the fracture toughness measurements were determined by the crack-indentation technique employing the graphical parameter fit of Charles and Evans.⁶ Loads from 1.96 N to 98.0 N gave equivalent results; therefore, a load of 2.94 N was employed to minimize branching and multiple cracks from Vickers indentation corners. Limited fracture-toughness work was conducted by the controlled-strength⁶ and DCB*⁷ methods to confirm the validity of the indentation results.

Young's modulus was determined by an ultrasonic technique^{†8} and corrected with reference to a National Bureau of Standards standard reference bar.⁹ Poisson's ratio, shear modulus, and bulk modulus were determined by a pulse-echo overlap technique.[‡] Young's modulus was confirmed with this instrumentation.

III. RESULTS AND DISCUSSION

Table I shows the relationship between microstructure, strength σ , and the critical stress-intensity factor, K_{IC} , otherwise known as fracture toughness. The controlled flaw and double-cantilever-beam techniques gave good agreement with indentation results, giving confidence to employing this method for most testing. Both large-grain-size polycrystalline material and a few melt-grown single crystals gave a K_{IC} of $0.9 \text{ MNm}^{-3/2}$. The stronger samples, as measured in bending, had higher fracture toughness. Flaw sizes, C , were calculated from the fracture mechanics relationship

$$\sigma = \frac{Y K_{IC}}{C^{1/2}} \quad (1)$$

*Test performed at the Naval Research Laboratory.

†Performed by G.C. Walther at IIT Research Institute, Chicago, Illinois, under Project D8142.

‡Parametrics.

where Y is a geometrical factor taken as 1.25 for the test conditions employed. The calculated flaw size is close to the grain size, particularly on the single-phase specimens. This suggests that grain pullout in machining or microstructure-related flaws controls strength.¹⁰ On the other hand, the two-phase 21- μm grain-size specimen had a similar calculated flaw size. This implies that another common defect controls strength and that the higher fracture toughness is responsible for the higher fracture stresses. Grooves from the diamond machining or pore nests are examples of flaws that could be independent of grain size.

Fracture surfaces were examined on representative samples. Fracture origins were difficult to locate on the large-grain-size samples. No obvious microstructural faults were observed as fracture origins. In several cases, the origin was near a corner, indicating a stress concentration. One such specimen is illustrated in Figure 2. This particular bar had a strength of 277 MPa, which is among the highest measured to date. The material is two-phase and the grain size is small (21 μm), favoring both a high stress-intensity factor and a small flaw size, the prerequisite for high-strength material. A large percentage of transgranular fractures occurred, which indicates strong grain bonding and properties near intrinsic values.

A detailed STEM characterization study will be reported separately.¹¹ In addition, Horvath¹² has recently completed analytical microscopy studies in the La_2O_3 - Y_2O_3 system, and has made a number of important observations. In the present study, two morphologies were observed for structures equilibrated in the two-phase zone. The first was equiaxed C grains containing intragranular, lathlike M precipitates. In many cases, the M phase was twinned as a result of the observed strain field (Figure 3). The other general structure exhibited untwinned intragranular second phases which also indexed as M (Figure 4). The single-phase C structures had clean grain boundaries and showed no compositional variation. The only observation of a H precipitate was made by Horvath on a sample that had

been heat treated for 1 min at 2200°C and quenched. The precipitate was only 0.8 μm in diameter; thus, the matrix probably provided enough constraint to prevent the H-to-M transformation.

The in-situ fracture experiments gave direct evidence for crack deflection (Figure 5) by the M twinned precipitate on a crack branch. The area along the main crack was too thick for TEM, but it revealed evidence of crack deflection on STEM backscattered images. A number of other fracture features were observed, including an apparent crack arrest by the M phase.¹¹

The 62- μm grain-size microstructure was selected for high-temperature strength measurements. The data reported in Figure 6 indicates a remarkably level strength/temperature relationship. This is undoubtedly due to the high melting point (2462°C) and low creep rates, which in turn are related to low self-diffusivities. The large grain size may also account for the low creep rates at the moderately high strain rate employed. The slight dip in strength at 500°C may be real even though the standard deviation overlaps the values obtained for adjacent test temperatures. Similar intermediate temperature dependencies have been seen in optical-quality polycrystalline Al_2O_3 and are ascribed to water-vapor stress corrosion.¹³

Since the fracture toughness was shown to control strength, studies were conducted to increase toughness. With its metastable, high-temperature H phase, the high-temperature, two-phase field of the La_2O_3 - Y_2O_3 system offers a unique opportunity to toughen Y_2O_3 . None of the other Y_2O_3 sintering aids, such as ZrO_2 , HfO_2 , ThO_2 , MgAl_2O_4 , MgO , or Al_2O_3 , have phase diagrams that offer the potential for second-phase toughening.

Figure 7 illustrates the effect of annealing time in the two-phase zone. The samples were quenched at 450°C/min in an attempt to retain the high-temperature H phase. Two types of samples were employed at one composition (9 m/o La_2O_3). In one case, green compacts were sinter-annealed. High density is achieved within a few minutes of sintering,¹

so the 10-min point corresponds to a fine-grained but dense structure. Increased annealing time coarsens the structure, and this is accompanied by a lower fracture toughness. The other structure tested was introduced into the anneal as optically clear 70- μm grain-size single-phase C material. As annealing continued, the grain size decreased due to the precipitation and growth of the H phase. Again, the reduced grain size was accompanied by higher fracture toughness. This phenomenon could be due to the energy absorption of the finer grain structure or due to the more uniform and more closely spaced distribution of the H (M) phase.

Figure 8 illustrates the dependence of fracture toughness on La_2O_3 concentration for both green compacts sinter-annealed and previously sintered/annealed samples. A significant increase in fracture toughness with higher second-phase concentration was realized for both types of samples. These samples were annealed for 3 hr, which means that grain refinement was well advanced on the previously sintered samples. The higher K_{IC} values for the three compositions corresponds to increased second-phase concentration, which is estimated from the phase diagram to be 16 v/o, 38 v/o, and 51 v/o for the three compositions.

Another experiment was conducted to vary La_2O_3 concentration, checking for the interrelationship between optical and mechanical properties. The composition range covered was 8.76 to 15.6 m/o La_2O_3 . At a sintering temperature of 2150°C, these compositions resulted in a H phase content from 14.5 to 58 v/o. Toughness was measured for samples quenched from 2150°C. Companion samples were annealed at 1950°C for 300 min. The results are reported in Figure 9. The fracture toughness of the as-sintered samples increases with volume concentration of second phase. After annealing, the toughness decreases to single-crystal values for all but the 15.6 m/o sample. Microstructural examination revealed that this sample retained the second phase. This sample was subsequently annealed at both 1850°C and 1750°C, and the second phase persisted, indicating a slight

discrepancy in the phase diagram, which is discussed in a separate paper.¹¹ The low transmittance of this sample correlates with the high second-phase content.

A series of 10.5 m/o La_2O_3 samples was sintered in the two-phase field at 2150°C for 90 min. Individual samples were subsequently annealed for 90 min over a range of temperature spanning the phase boundary well into the single-phase cubic field. The samples were polished to 2-mm thickness and the optical transmittance was measured. Then they were annealed at 1000°C to relieve surface polishing stresses, and the fracture toughness was determined. The same samples were subsequently polished to 1-mm thickness and remeasured for transmittance. The results of this experiment are shown in Figure 10.

The toughness rises from the single-crystal value for material annealed at 1975°C to $\cong 20\%$ higher for a two-phase body annealed well above the phase boundary. The peak toughness is slightly lower than expected from Figure 9. This is a result of the increased grain size resulting from the 3-hr total cycle, compared with 1½ hr for the data reported in Figure 9. It is thought to be extremely significant that the toughness rises to near the peak level for samples annealed at 2000°C and 2025°C. These samples have significant transparency, suggesting that it may be possible to achieve both toughening and transparency. Based on the steep transmittance drop at 2050°C, a suggested phase boundary is indicated, which is in good agreement with the phase diagram. It was also noted that the transmittance increased with decreasing annealing temperature. The driving force for the phase transition increases in this direction, leading to increased grain growth of the C phase and increased chemical homogenization.

The observed toughening was evaluated with respect to the possible mechanisms such as crack deflection, crack bowing, crack branching, microcracking, and martensitic transformational toughening. The phase transformation between the H and M phases offers the potential for martensitic toughening. However, the only direct evidence for retention of the hexagonal phase is in a sample annealed at 2200°C for 1 min and quenched.¹² Further, the

degree of toughening is lower than would be expected for martensitic toughening. Thus, it appears that heat-treating schedules have not yet been devised that would make possible the use of this mechanism if, in fact, it exists in this system. Microcracking is ruled out based on the microstructural evaluation, which is aided by the samples' transparency.

Crack bowing produces a nonlinear crack analogous to dislocation pinning. Crack deflection produces a nonplanar crack as the crack front diverts around the second-phase particle due to residual strain resulting from thermal expansion or elastic modulus mismatch between the matrix and second phase. It is difficult to discriminate between crack bowing and crack deflection. Cracks resulting from the STEM analysis showed evidence for crack deflection. Consequently, the toughening was compared to the crack deflection model of Faber and Evans.¹⁵ Crack deflection by spherical, disc, or rod-shaped second phases was considered in this model. Figure 11 shows the toughness data obtained from the several quenched composition series normalized to the single-crystal toughness ($0.9 \cdot \text{MN} \cdot \text{m}^{-3/2}$) and compared with the model for spherical and rod second phases. The volume fractions were calculated based on the phase diagram, knowing the starting composition and equilibrium temperature. The data fall between the model prediction for spheres and rods. This coincides with the model prediction for discs or thin platelets. The metallography and TEM characterization has shown a variety of disc, polyhedron, and plate morphologies in the second phase, depending on the annealing cycle. Figures 1(b), 1(c), 2, and 3 are examples. It appears reasonable to find different levels of toughening, depending on microstructure. The dense two-phase sample [e.g., Figure 1(b)] showed the most plate-like structures and demonstrated the greatest toughening, as shown in Figure 11. The data best fit a model for crack deflection around the M second phase. In a given series plotted in Figure 11, the matrix grain size was within a narrow range ($3\text{--}8 \mu\text{m}$). However, a grain size effect on fracture toughness may contribute in an additive way to the observed relationship with v/o of second phase.

Figure 10 shows that it is possible to achieve some toughening by annealing just below the phase boundary in the single-phase C field. The toughening mechanism in this case is open to speculation. Tests were conducted to determine a possible grain-size dependence. Samples were annealed for periods from 5 to 500 min at 2020°C. The fracture toughness is plotted as a function of grain size in Figure 12. No clear trend is shown within the range tested. The falloff in toughness noted in Figure 10 for samples annealed for 3 hr at 2025, 2000, and 1975°C is accompanied by an increase in grain size from 10 to 70 μm .

Monroe and Smyth² found a weak dependence of fracture energy on grain size falling from ~ 5000 ergs/cm² to ~ 4000 ergs/cm² for the 10 to 70- μm change in grain size for pure Y₂O₃. Statistical analysis of their data demonstrated that this decline was real within a 95% confidence limit. Using the relationship $K_{IC} = (2\gamma E)^{1/2}$, this corresponds to a change of 1.28 MNm^{-3/2} to 1.15 MNm^{-3/2} in fracture toughness. This represents a 9% change in fracture toughness. The study reported in Figure 10 shows a 20% change in toughness for the 10 to 70 μm grain-size shift. This implies that about half of the enhanced toughness observed for the 10 μm grain-size sample annealed at 2025°C may be due to a grain-size effect. However, samples annealed to give different grain sizes in the single-phase region at 2025°C do not show a grain-size dependence on fracture toughness in the 6 to 54 μm range (Figure 12). It appears possible that some, as yet unidentified, mechanism is contributing enhanced toughness to these 2025°C specimens. It is possible that a minor, undetected concentration of second phase exists in these samples, since they have been examined only by x-ray and metallography.

The fracture energy data of Rice et al.⁴ translates to a fracture toughness of 1.56 ± 2 MNm^{-3/2} for polycrystalline ThO₂-doped Y₂O₃. This compares favorably with the DCB data on La₂O₃-doped Y₂O₃ (Table I). The fact that the DCB values are higher than the 0.9 MNm^{-3/2} used for the single-phase fracture toughness in the present indentation study is not surprising, since different fracture toughness measurement techniques seldom agree precisely. The toughening observed in this study relative to the single-phase material is

believed to be valid, and in all likelihood would have been observed if DCB or some other fracture toughness technique was employed.

The elastic properties of $0.09 \text{ La}_2\text{O}_3 \cdot 0.91 \text{ Y}_2\text{O}_3$ are reported in Table II. The agreement between the two methods of determining Young's modulus is good, considering the fact that different samples were employed. Both of the samples had the same composition, and the sintered densities were very close (5.140 g/cm^3 for the bar in method 1 and 5.130 g/cm^3 for the disc in method 2), so the difference cannot be attributed to porosity. The bulk and shear modulus, together with Poisson's ratio, appear reasonable for a material with low Young's modulus.

Young's modulus of pure Y_2O_3 was studied by Marlowe and Wilder using a resonance frequency method.¹⁶ Their data, extrapolated to zero porosity, gave 179.7 GPa. The slightly lower Young's modulus (166.5 GPa) for $0.09 \text{ La}_2\text{O}_3 \cdot 0.91 \text{ Y}_2\text{O}_3$ is reasonable, considering the expanded unit cell (10.675 \AA vs 10.603 \AA) and higher density (5.13 g/cm^3 vs 5.03 g/cm^3). Dickson and Anderson¹⁷ found a Young's modulus of 173.7 GPa for $0.09 \text{ ThO}_2 \cdot 0.91 \text{ Y}_2\text{O}_3$. This solid solution also expanded the Y_2O_3 lattice to 10.646 \AA , which is not as much as the equivalent molarity of La_2O_3 . They report a Poisson's ratio of 0.295 for this material. The observed Young's modulus is indicative of the moderate atomic bonding and complex C structure which contains a large oxygen vacancy.

The strength-to-modulus ratio is $>1 \times 10^{-3}$, with some specimens in the range of 1.66×10^{-3} . The microstructure and surface finish of most polycrystalline oxides are considered excellent when this ratio exceeds 1×10^{-3} . This becomes important when considering materials for thermal shock applications where strength/modulus is contained in the governing relations.¹⁸

IV. CONCLUSIONS

La_2O_3 -doped Y_2O_3 is a versatile system capable of being fabricated into many different microstructures. In two-phase bodies, the fracture toughness and strength are strongly dependent on concentration and morphology of the H (M) second phase. Lathlike second phases are tougher than more equiaxed structures. The fine-grained two-phase structures are tougher than the larger-grained two-phase material. Grain size is less important in the single-phase C microstructures.

The fracture toughness data support crack deflection as a major contributing toughening mechanism. The microscopy evidence supports this conclusion. There was no evidence for martensitic toughening, as heat treatments have not yet been devised to retain the high-temperature H phase.

The specular transmittance at 2-5 μm depends strongly on the concentration of M phase. Annealing just under the C/C + H phase boundary produced a structure with minimal transmittance loss and ~20% improvement in fracture toughness. The fracture toughness did not appear to be a function of grain size for this annealing temperature. The nature of the toughening mechanism for this structure is unclear.

A 62- μm grain-size single-phase microstructure exhibited a level strength versus temperature relationship to 1600°C, indicating low creep rates and low subcritical flaw growth.

The strength-to-modulus ratio, $\geq 1 \times 10^{-3}$, indicates good microstructure control and low surface flaw size, placing this material among the class of strong oxides which have potential to survive in severe thermal shock environments.

V. ACKNOWLEDGMENTS

This work is supported in part by the Office of Naval Research. We are indebted to many colleagues at GTE for their contributions, especially T. Emma, R. Thibodeau, B. MacAllister, and M. Katsoulakos.

VI. REFERENCES

1. W.H. Rhodes, "Controlled Transient Solid Second-Phase Sintering of Yttria," *J. Am. Ceram. Soc.* 64, pp. 144-150, 1981.
2. L.D. Monroe and J.R. Smyth, "Grain Size Dependence of Fracture Energy of Y_2O_3 ," *J. Am. Ceram. Soc.* 61, p. 538, 1978.
3. T. Tani, Y. Miyamoto, M. Koizumi, and M. Shimada, "Grain Size Dependence of Vickers Microhardness and Fracture Toughness in Al_2O_3 and Y_2O_3 Ceramics," *Ceram. Int.* 12, p. 33, 1986.
4. R.W. Rice, S.W. Freiman, and J.J. Mecholsky, "The Dependence of Strength-Controlling Fracture Energy on the Flaw Size to Grain-Size Ratio," *J. Am. Ceram. Soc.* 63, p. 129 (1980).
5. A.G. Evans and E.A. Charles, "Fracture Toughness Determination by Indentation," *J. Am. Ceram. Soc.* 59, p. 371, 1976).
6. P. Chantikul, G.R. Anstis, B.R. Lawn, and D.B. Marshall, "A Critical Evaluation of Indentation Techniques for Measuring Fracture Toughness: II. Strength Method," *J. Am. Ceram. Soc.* 64, p. 539, 1981.
7. S.W. Freiman, D.R. Mulville, and P.W. Mast, "Crack Propagation Studies in Brittle Materials," *J. Mater. Sci.* 8, p. 1527, 1973.
8. S. Spinner and W.E. Tefft, "A Method for Determining Mechanical Resonance Frequencies and for Calculating Elastic Moduli from These Frequencies," *ASTM Proc.* 61, pp. 1221-1238, 1961.
9. R.W. Dickson and J.B. Wachtman, Jr., "An Alumina Standard Reference Material for Resonance Frequency and Dynamic Moduli Measurement I. For Use at 25°C," *J. Res. Natl. Bur. Stand.* 75A (3), pp. 155-162, 1971.
10. R.W. Rice, S.W. Freiman, and P.F. Becher, "Grain Size Dependence of Fracture Energy in Ceramics: I. Experiment," *J. Am. Ceram. Soc.* 64, p. 345, 1981.
11. G.C. Wei, T. Emma, and W.H. Rhodes, "Analytical Microscopy Study of Phases and Fracture in Y_2O_3 - La_2O_3 Alloys," submitted to *J. Am. Ceram. Soc.*

12. S.F. Horvath, "Analytical Electron Microscopy Studies in the Yttrium Oxide-Lanthanum Oxide (Y_2O_3 - La_2O_3) System," M.S. Thesis, Lehigh University, 1985.
13. R.R. Shaw and R.J. Charles, "Delayed Failure of Polycrystalline and Single Crystal Alumina," GE Report 62-RL-3081M.
14. (a) J. Coutures and M. Foex, "High Temperature Equilibria in the System La_2O_3 - Y_2O_3 ," *J. Solid State Chem.* 11 (4), pp. 294-300, 1974.
(b) M. Mizuno, A. Rouanet, T. Yamada, and T. Noguchi, "Phase Diagram of the System La_2O_3 - Y_2O_3 at High Temperatures," *Yogyo Kyokai Shi* 84 (7), pp. 342-348, 1976.
15. K.T. Faber and A.G. Evans, "Crack Deflection Processes — I. Theory," *Acta Metal.* 31, p. 565, 1983.
16. M.O. Marlowe and D.R. Wilder, "Elasticity and Internal Friction of Polycrystalline Yttrium Oxide," *J. Am. Ceram. Soc.* 48, pp. 227-233, 1965.
17. R.W. Dickson and R.C. Anderson, "Temperature Dependence of the Elastic Moduli of $91 Y_2O_3 + 9 ThO_2O_2$ from 25°C to 1100°C," *J. Am. Ceram. Soc.* 51, pp. 233-234, 1968.
18. D.P.H. Hasselman, "Thermal Stress Resistance Parameters for Brittle Refractory Ceramics: A Compendium," *Ceram. Bull.* 49 (12), p. 1033, 1970.

Table I
Dependence of fracture toughness and strength on microstructure

Phases	Grain Size (μm)	Bend Strength (MPa)	Indentation K_{IC} ($\text{MN}\cdot\text{m}^{-3/2}$)	Controlled Flaw K_{IC} ($\text{MN}\cdot\text{m}^{-3/2}$)	Double* Cantilever K_{IC} ($\text{MN}\cdot\text{m}^{-3/2}$)	Calculated Flaw Size (μm)
1	Single	—	0.9	—	—	—
1	40	166 ± 34	1.1	—	—	69
1	62	161 ± 21	0.9 ± 0.1	0.8	1.3	49
2	8	—	1.5	1.3	—	—
2	21	202 ± 44	1.3 ± 0.1	—	1.2	65

*Courtesy of Naval Research Laboratory.

Table II
Elastic properties

Property	Method	Value
Young's modulus	1	163.9 GPa
Youngs' modulus	2	166.5 GPa
Shear modulus	2	63.64 GPa
Bulk modulus	2	144.5 GPa
Poisson's ratio	2	0.3080

1. Method of Reference 8.
2. Parametrics pulse echo.

Figure 1. Typical microstructures for $0.09 \text{ La}_2\text{O}_3 \cdot 0.91 \text{ Y}_2\text{O}_3$.

- (a) Sintered at 2125°C for 20 min and annealed at 1950°C for 120 min.
- (b) Sintered at 2150°C for 180 min and quenched.
- (c) Sintered at 2150°C for 90 min, annealed at 1950°C for 90 min, and reannealed at 2150°C for 10 min.

Figure 2. Fracture origin on two-phase $21\text{-}\mu\text{m}$ grain-size sample.

Figure 3. Bright-field transmission electron micrograph of a two-phase sample showing twinned second-phase particles.

Figure 4. Bright-field transmission electron micrograph of a two-phase sample showing untwinned second-phase particles.

Figure 5. Bright-field transmission electron micrograph of a two-phase sample fractured in situ, showing deflection of crack by second-phase particles.

Figure 6. Four-point bend strength vs temperature for $62\text{-}\mu\text{m}$ grain-size material.

Figure 7. Effect of annealing time in two-phase zone (2150°C) on fracture toughness for two different starting structures.

Figure 8. Effect of La_2O_3 concentration on fracture toughness for samples quenched from the two-phase zone (2150°C).

Figure 9. Transmittance and toughness for La_2O_3 -doped Y_2O_3 of varying La_2O_3 content.

Figure 10. Effect of annealing temperature on transmittance and toughness.

Figure 11. Relative toughness of two-phase material compared with theory of Faber and Evans.

Figure 12. Fracture toughness as a function of grain size for samples annealed at 2020°C .

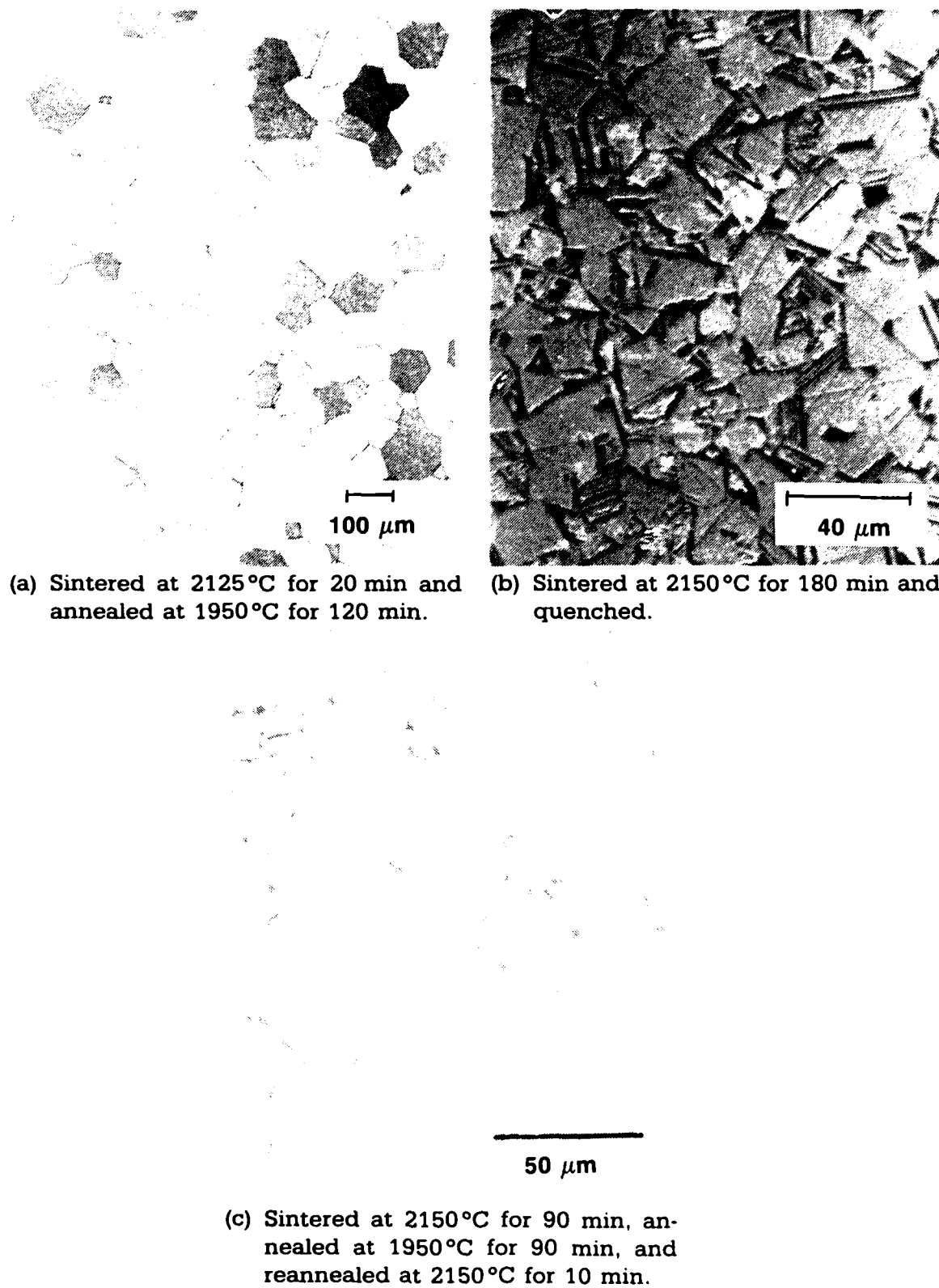


Figure 1. Typical microstructures for 0.09 $\text{La}_2\text{O}_3 \cdot 0.91 \text{Y}_2\text{O}_3$.

FRACTURE ORIGIN

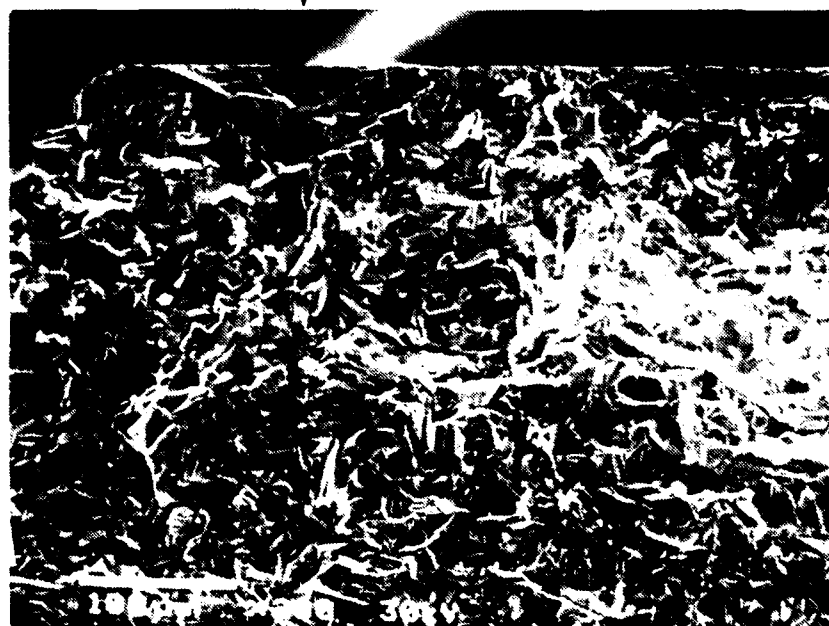


Figure 2. Fracture origin on two-phase 21- μm grain-size sample.



Figure 3. Bright-field transmission electron micrograph of a two-phase sample showing twinned second-phase particles.

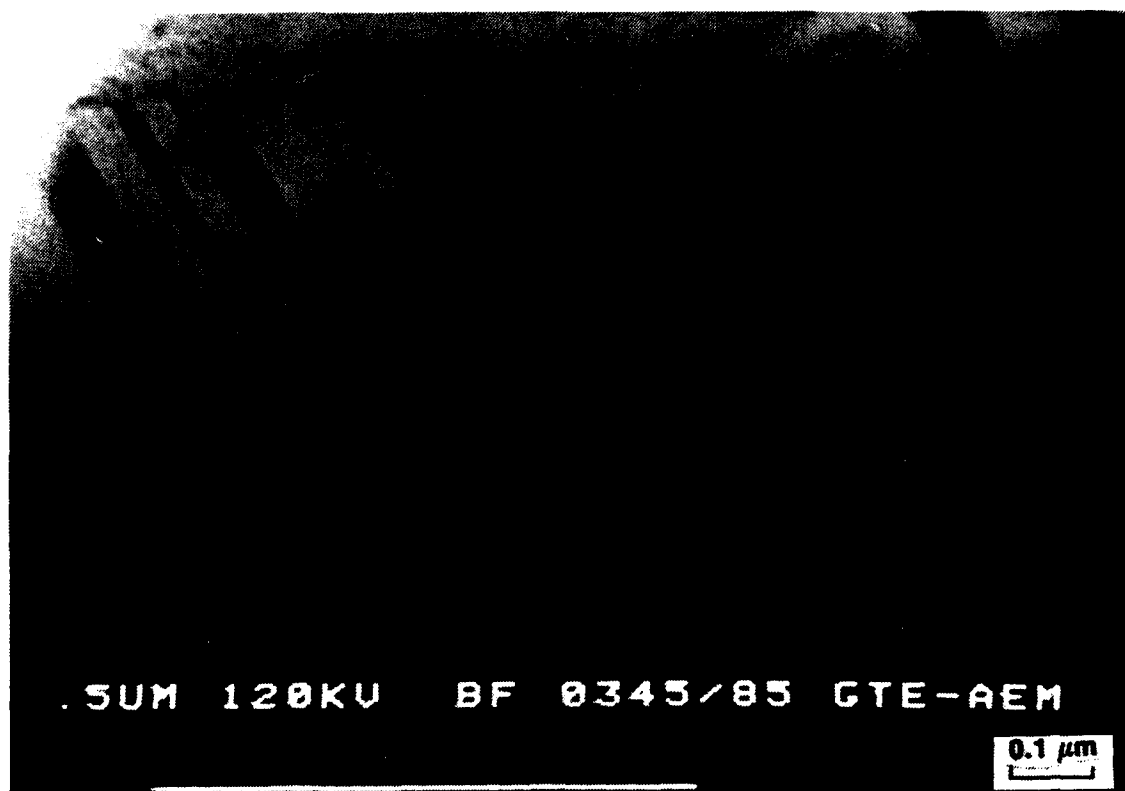


Figure 4. Bright-field transmission electron micrograph of a two-phase sample showing untwinned second-phase particles.



Figure 5. Bright-field transmission electron micrograph of a two-phase sample fractured in situ, showing deflection of crack by second-phase particles.

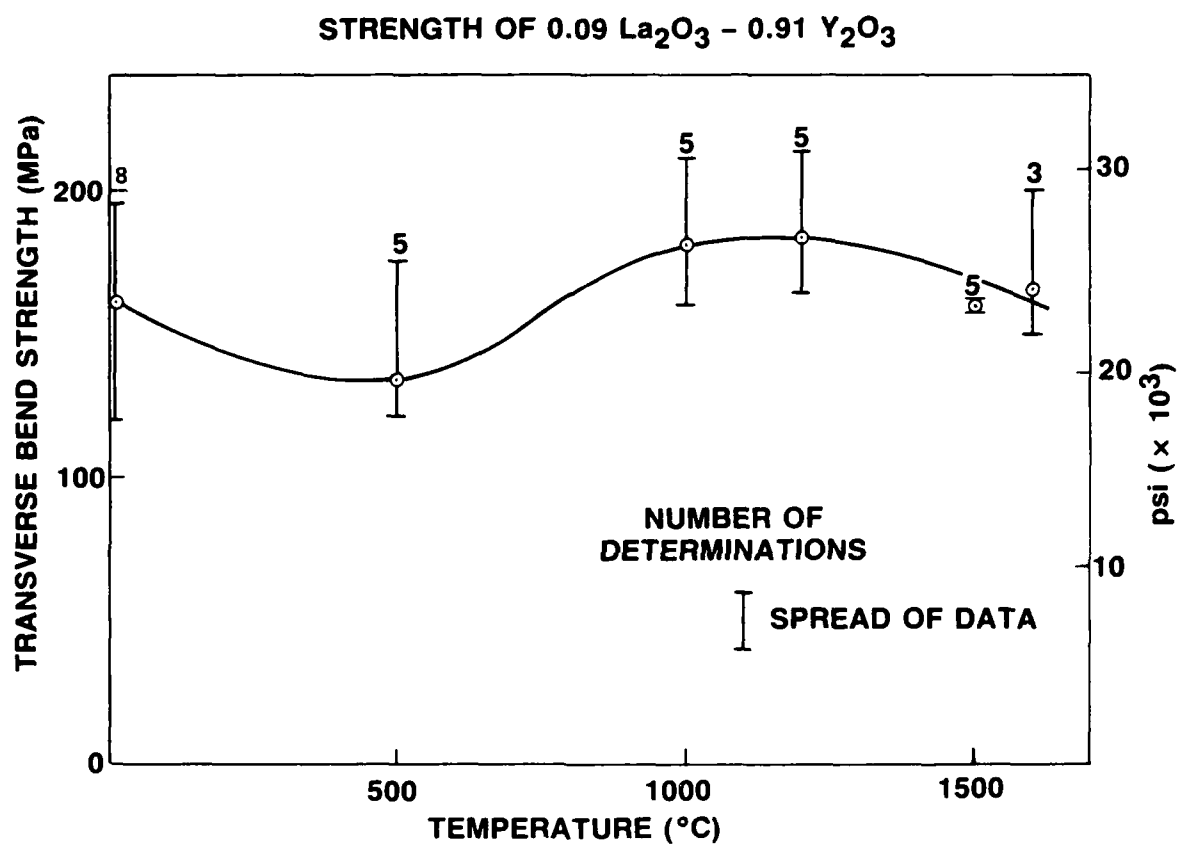


Figure 6. Four-point bend strength vs temperature for 62- μm grain-size material.

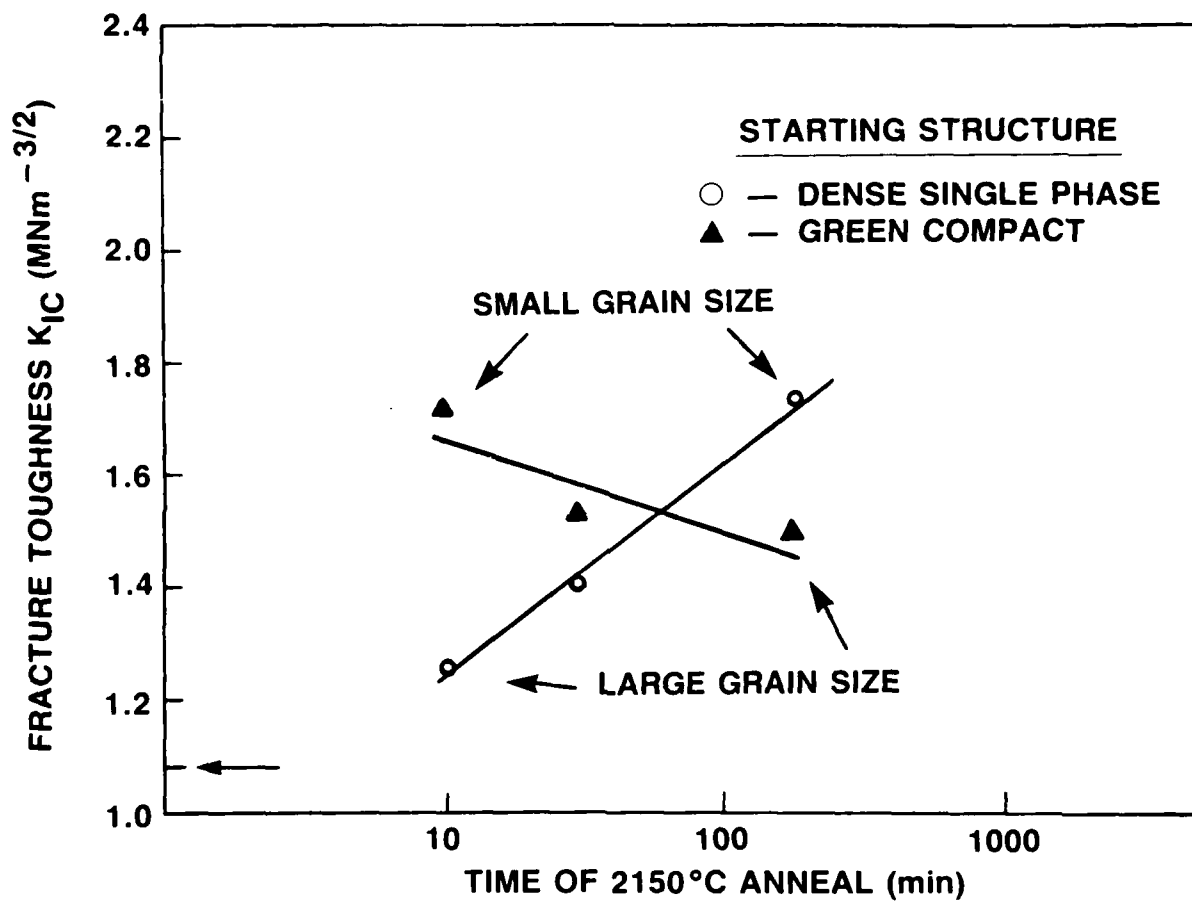


Figure 7. Effect of annealing time in two-phase zone (2150°C) on fracture toughness for two different starting structures.

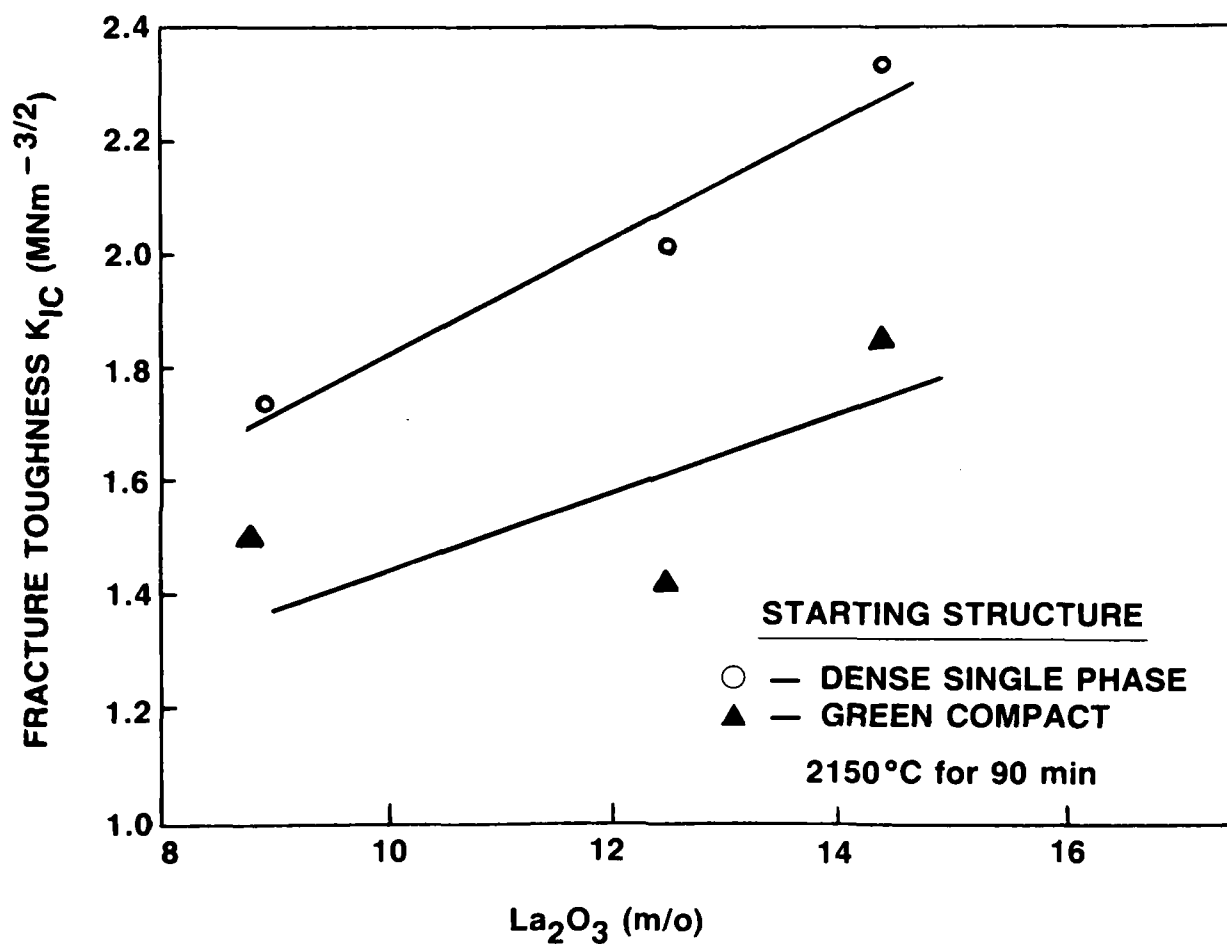


Figure 8. Effect of La_2O_3 concentration on fracture toughness for samples quenched from the two-phase zone (2150°C).

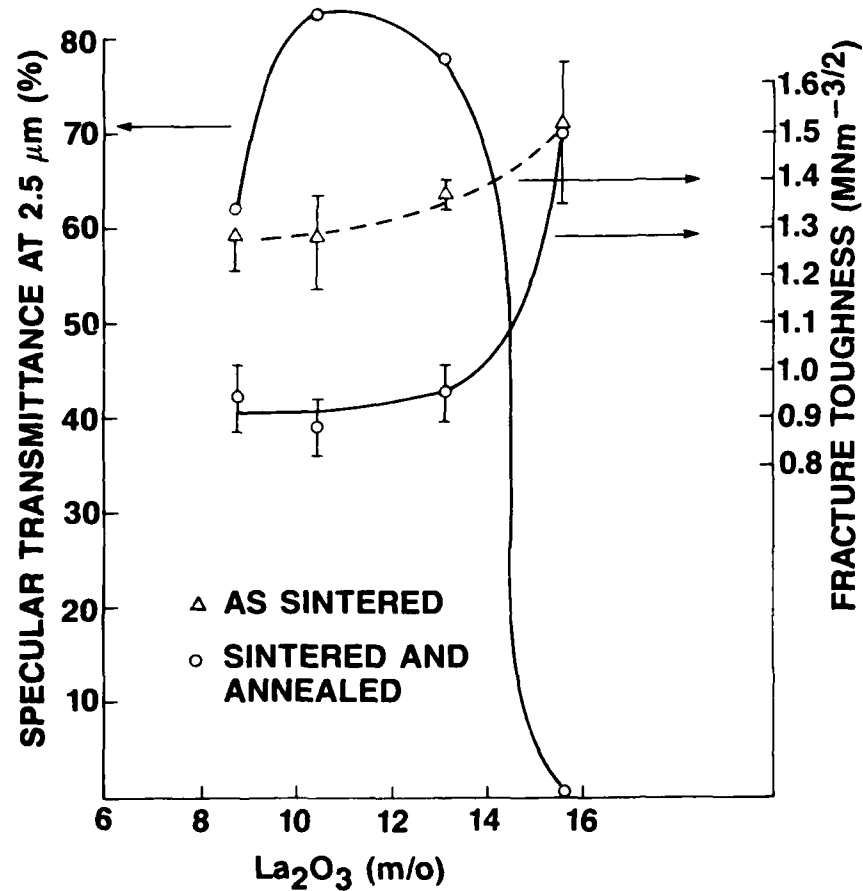


Figure 9. Transmittance and toughness for La_2O_3 -doped Y_2O_3 of varying La_2O_3 content.

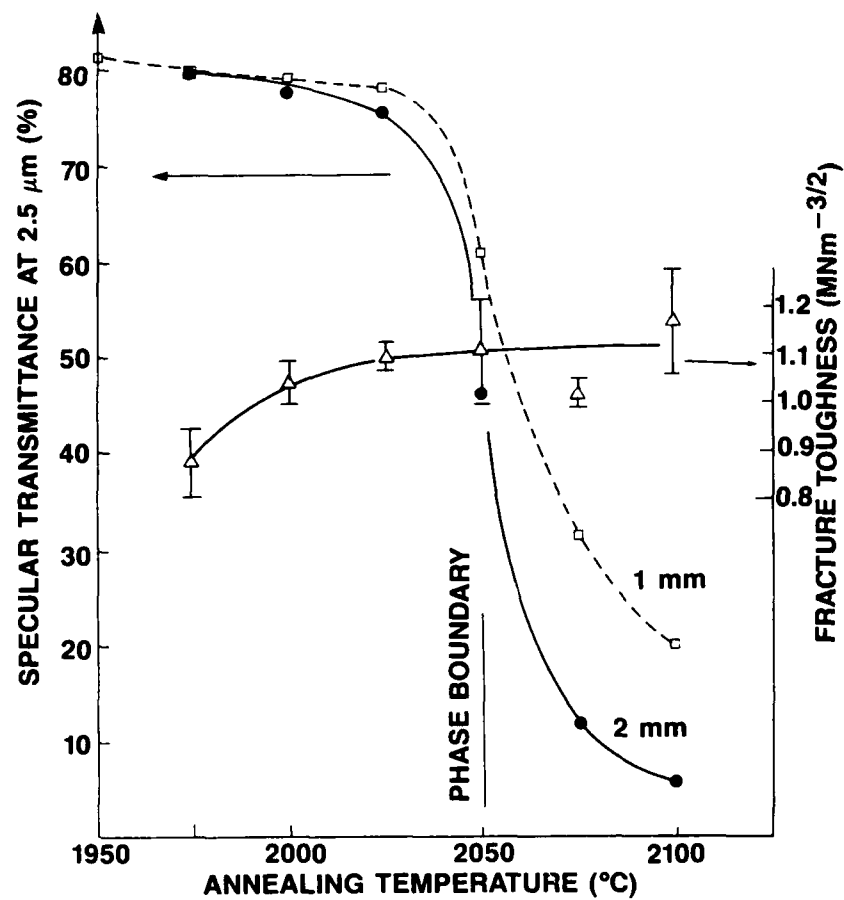


Figure 10. Effect of annealing temperature on transmittance and toughness.

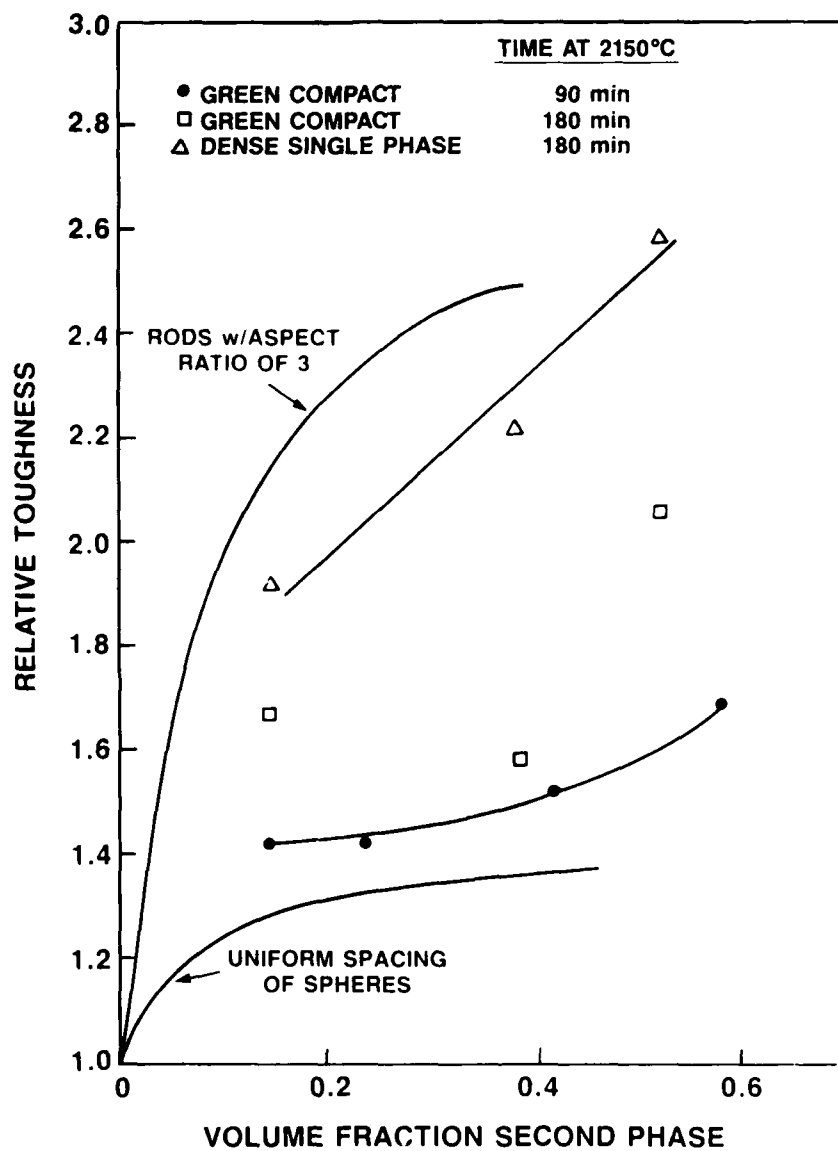


Figure 11. Relative toughness of two-phase material compared with theory of Faber and Evans.

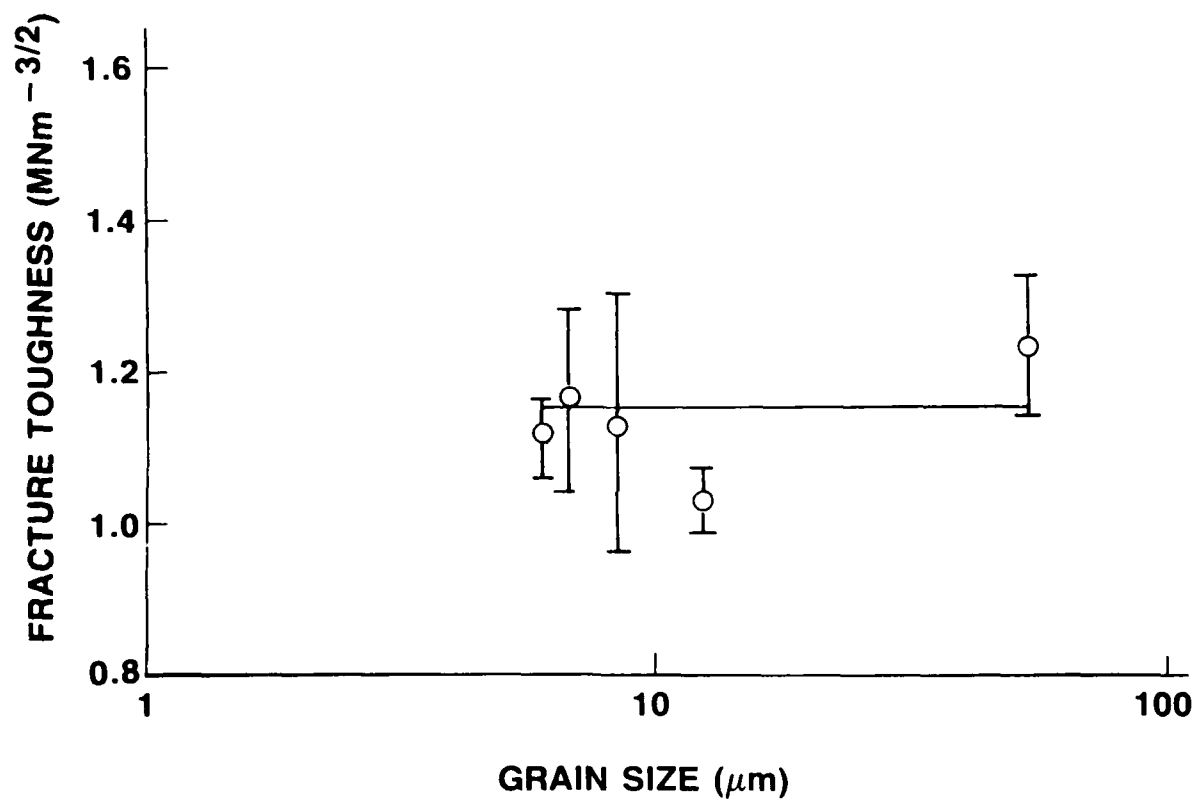


Figure 12. Fracture toughness as a function of grain size for samples annealed at 2020°C.

**ANALYTICAL MICROSCOPY STUDY OF PHASES
AND FRACTURE IN Y_2O_3 -DOPED La_2O_3 ALLOYS**

by

G.C. Wei
T. Emma
W.H. Rhodes

Analytical Microscopy Study of Phases and Fracture in Y_2O_3 - La_2O_3 Alloys*

G.C. Wei, T. Emma, and W.H. Rhodes

GTE Laboratories Incorporated

Waltham, MA 02254

ABSTRACT

Transmission electron microscopic analyses defined the structures and compositions in single-phase and two-phase La_2O_3 -doped Y_2O_3 material fabricated by the transient solid second-phase sintering. The composition in single-phase 10 m/o La_2O_3 -doped, sintered and annealed samples was found to be uniform, indicating diffusivity was sufficiently high for homogenization in the single-phase field. Two-phase 16 m/o La_2O_3 -doped sintered and annealed samples showed two morphologies: (1) intragranular, lathlike, monoclinic second-phase particles (twinned and untwinned) and (2) equiaxed cubic matrix. The second-phase particles were identified as the monoclinic phase derived from the high-temperature hexagonal phase through a rapid phase transition. Microchemical analyses of the phases suggested adjustments to the Y_2O_3 - La_2O_3 phase diagram. Observation of the interactions of the intragranular second-phase particles with crack propagation indicated crack deflection as one of the mechanisms responsible for toughening (1.5 vs. $0.9 \text{ MPa}\cdot\text{m}^{1/2}$).

INTRODUCTION

La_2O_3 -doped Y_2O_3 is an infrared (3.5 to $5.5 \mu\text{m}$) transmitting material that possesses exceptional optical, mechanical, and thermal properties. Pore-free, single-phase, polycrystalline La_2O_3 -doped Y_2O_3 is transparent since the structure is C-type cubic. This material is made by a transient solid second-phase sintering technique.¹ Briefly stated, the process involved coprecipitating an La_2O_3 - Y_2O_3 composition that has a high-temperature two-phase (hexagonal, H, and cubic, C) field and a wide single-phase solid solution (cubic C phase) field below about 2000°C (Figure 1). By sintering in the two-phase field, grain growth is retarded due to the

*Work partially sponsored by the Office of Naval Research.

Paper presented at the American Ceramic Society Annual Meeting, Chicago, IL, 1986.

presence of the second phase. Pores remain at grain boundaries until they are eliminated by the normal diffusional processes operating in sintering. The material is subsequently annealed in the single-phase cubic field to achieve an equiaxed microstructure. The extremely low porosity microstructure is responsible for the excellent optical and infrared transmittance properties. The second phase can be retained by special anneals to impart mechanical toughening.² A family of Y_2O_3 - La_2O_3 alloys can be made with optimal mechanical and optical properties. This paper reports on characterization of the microstructures in the single-phase and two-phase La_2O_3 -doped Y_2O_3 using analytical electron microscopy (AEM). The results of observation on the interactions of crack propagation with second-phase particles are also presented.

EXPERIMENTAL PROCEDURES

Three types of samples (A, B, and C) were examined by AEM. Sample A is a 9.87 m/o La_2O_3 -doped, sintered (2150 °C for 90 min) and annealed (1950 °C for 6 hr) Y_2O_3 material. This sample was used as a standard required for microchemical analysis. Induction coupled plasma (ICP) analysis showed 11.63 w/o La and 68.01 w/o Y corresponding to 9.87 m/o La_2O_3 in the standard. Sample B is a 10 m/o La_2O_3 -doped, sintered (2200 °C for 2 hr) and annealed (1950 °C for 6 hr), single-phase material. Sample C is a two-phase, toughened, 16 m/o La_2O_3 -doped, sintered (2150 °C for 90 min) and annealed (1950 °C for 6 hr) Y_2O_3 material.

All TEM specimens were made by mechanical thinning to <100 μm thick followed by ion beam milling using a Gatan dual ion miller with argon gas and 5-kV operating voltage. A cold trap was used in the ion milling system to prevent contamination of Si from the pump oil. A sufficient number of specimens were prepared to ensure that the fields examined were representative of the material's bulk. A thin layer of carbon (<5 nm) was deposited by vacuum evaporation in order to provide a conductive link with ground for these highly insulating specimens. Specimens were examined using Philips EM400T STEM operating at 120 kV.

The specimen from the standard sample A was used in measuring the appropriate k-or Cliff-Lorimer factor in microchemical analyses. In order to ensure self-consistency, two k-factors were measured: one was based on the ratio of the L lines for yttrium and the L lines of lanthanum; the other was based on the ratio of the K lines of yttrium and L lines of lanthanum. These factors were 0.55 and 1.11, respectively. Although many of the areas examined met the "thin film criterion," corrections were made for XPT, absorption, and fluorescence. The

k factors were based on 90,000 counts in the lanthanum window at approximately 1.5 times the full width at half maximum. Thicknesses were measured by the convergent beam technique. Electron diffraction in the convergent beam (CBED) mode and the conventional selected area (SAED) mode were used to establish the crystal polymorph and the crystallographic relationship of the primary and intragranular phases. In addition, the single-phase, 10 m/o La_2O_3 -doped, sintered and annealed sample B was tested for lattice parameter shifts within single grains using the convergent beam technique. Compositional changes within these grains were also tested by point counting with energy dispersive x-ray analysis (EDXA). These were used for identifying compositional variations within single grains and the degree of homogenization in the single-phase sample.

TEM in-situ fracture studies were performed on sample C using a straining stage to observe crack propagation. The sample was in a dogbone configuration with central perforation. As the stress was applied, cracks were initiated at the edge of the hole and propagated in a direction nearly perpendicular to the tensile axis. Interactions of crack propagation with second-phase particles were observed.

RESULTS AND DISCUSSION

Single-Phase Material

AEM microchemical analyses by EDXA were performed on over ten grains in the single-phase sample B. This type of sample commonly exhibited relic boundaries within grains on etched metallography specimens.¹ The relic boundary was thought to be associated with grain structure during the sintering part of the sintering/annealing cycle and might possibly result from impurities being swept to these boundaries. The relic boundary was also possibly associated with compositional variation. STEM examinations of sample B showed "spots" that appeared to be a result of selective etching during ion milling (Figure 2), but no relic boundaries. The EDXA identified no detectable impurities. The La-to-Y ratio was found to be a constant in the central or near-boundary portions of the grain (Figure 2). Selected area electron diffraction pattern confirmed the cubic lattice of the single-phase material. The microstructure consisted of equiaxed cubic grains ($\cong 60 \mu\text{m}$) and clean grain boundaries. Dislocation networks near grain boundaries were observed only rarely. Observations of the lattice parameter shifts based on CBED analyses of different areas within single grains showed no detectable compositional variations. The detection limit was 0.5 m/o La_2O_3 . The results

showed that the 1950°C/6 hr annealing cycle appeared to be sufficient for a complete homogenization for samples formulated with 10 m/o La_2O_3 . The relic boundaries observed metallographically appeared to be subgrain boundaries that were not associated with compositional variation or impurity segregation.

Two-Phase Material

In the 16 m/o La_2O_3 -doped, sintered (2150°C for 90 min) and annealed (1950°C for 6 hr) Y_2O_3 sample C, two morphologies were observed: a generally equiaxed structure (5 to 10 μm) consisting of the cubic phase and a lathlike ($\cong 0.1$ to 1 μm by 5 to 10 μm) intragranular phase having a monoclinic lattice (Figure 3). This 16 m/o La_2O_3 -doped Y_2O_3 sample was sintered at 2150°C for 90 min, cooled to room temperature, and annealed at 1950°C for 6 hr. The sintering and annealing were all in the two-phase field, unlike most of the 9 or 10 m/o La_2O_3 -doped samples that were typically sintered in the two-phase field and annealed in the single-phase field. Samples with lower La_2O_3 concentrations would have converted to the single-phase cubic structure during the 1950°C anneal. In sample C, the intragranular second phase was mostly found to be strained with what appeared to be twins running nearly perpendicular to the lathlike body [Figure 3(a)]. Other intragranular phases were found to be defect free [Figure 3(b)]. A typical example of a bright field image together with the x-ray spectra is shown in Figure 4. The x-ray spectra indicated that the ratio of La to Y was higher in the second phase than in the matrix. A line scan for Y and La concentration profiles across the second phase and matrix illustrating the high La content in the lathlike second phase is shown in Figure 5. The concentration profiles indicated no significant diffusion gradients inside the second phase or matrix. Dark field images showed the matrix phase surrounding the second phase to be of the same crystallographic orientation. The lathlike second phases were within a single cubic matrix grain and thus the term "intragranular" was used to describe the lathlike second phase. CBED patterns of the matrix and microdiffraction pattern of the second phase are shown in Figure 6, together with the areas forming the patterns. The CBED data showed that the matrix had cubic symmetry. The CBED pattern (Figure 6) and indexing of selected area electron microdiffraction patterns (Figures 7 and 8) showed that the two phases were cubic and monoclinic in sample C. Figure 8 shows the SAED pattern of both the matrix and second phase with the diffraction spots arising from the second phase indexed as reflections of the monoclinic phase. The matrix was indexed as the C-type cubic phase ($a_0 = 1.0607$ nm). The lattice spacings and the angles between the reflection planes of the second phase agreed with these calculated from the x-ray diffraction pattern of the B phase (B- Gd_2O_3 structure, monoclinic symmetry, $a_0 = 1.4061$ nm, $b_0 = 0.3566$ nm, $C_0 = 0.8760$ nm,

$\beta = 100.1^\circ$). The subscript c and m to the indices of reflection planes in Figures 7 and 8 referred to the cubic and monoclinic phases, respectively. No hexagonal phase was found. The absence of the hexagonal polymorph could be a result of a rapid H→B phase transformation due to the relatively large size of the second phase.

The intragranular B phase could be present during the anneal as residual H phase particles. A two-phase assemblage (16 m/o La_2O_3) at 2150°C sintering temperature contained $\cong 60$ v/o H phase. During the subsequent annealing, the amount of the H phase would decrease and that of the cubic matrix would increase; the composition of the H and C phases would change in accordance with the phase rules in the two-phase field of the Y_2O_3 - La_2O_3 phase diagram. As the material cooled after annealing, the H phase might (1) convert to the stable B phase with an attendant increase in the solute content, and (2) transform to the C phase with a reduced solute content. The presence of the intragranular monoclinic phase is thought to be a result of the above two reactions. In other words, the B phase particles inside the cubic grains might be derived from the residues of the H phase that, during the annealing, was partially transformed to the C phase.

Note that the existence of the H phase was reported³ in a 9 m/o La_2O_3 -doped Y_2O_3 sample quenched from 2200°C and the size of the intragranular, ellipsoidal, hexagonal phase was small (0.8 by 0.5 μm). Some extra spots were observed in the SAED pattern (Figure 8). They could originate from several sources. The most likely are structure factor changes due to the scattering factor differences between yttrium and lanthanum, and incomplete convergence of the interference function resulting in elongated reciprocal lattice points. The crystallographic relationship between the matrix and intragranular phase was established. The $(\bar{2}2\bar{2})_c$ and $(402)_m$ planes were approximately parallel in adjacent phases.

As described before, the lathlike, monoclinic second phase in the two-phase material was often found to be strained with a twinned substructure. The structure of the twins was analyzed based on the results of SAED (Figure 9). The twin plane was $(313)_m$, similar to the twins found in other monoclinic rare-earth oxides.⁴ The volume expansion was reported to be 1% for H→B transition and 8% for H→C transition in pure Y_2O_3 .⁵ The presence of the twins in monoclinic second phase in sample C is believed to be a result of the displacive nature and deformation involved in the hexagonal-to-monoclinic transformation. The strain field surrounding the second-phase particles is caused by (1) the volume changes associated with the phase transitions (H→B and H→C) and (2) mismatch between thermal expansions and elastic moduli in the matrix and second phase.

Microchemical analysis of each phase used the thin film method. The results of analyses taken from several matrix grains and several intragranular second-phase particles for two-phase sample C are presented in Table I. The k factors and thicknesses are also shown in the same Table. The use of Y's K line in the microchemical analyses yielded results similar to those using Y's L line. As shown in Table I, The La_2O_3 contents in the matrix phase varied from 6.7 to 9.1 m/o, while those in the intragranular second phase ranged from 34 to 38 m/o La_2O_3 . The variations in composition may well be in the range of analysis uncertainty. The results were different from the indications from the current Y_2O_3 - La_2O_3 phase diagram; the matrix phase had lower La_2O_3 contents than the phase diagram (1950°C) value (15 m/o La_2O_3), while the second phase had much higher La_2O_3 content relative to the prediction (27 m/o La_2O_3 at 1950°C) from the phase diagram. The compositions of the matrix phase (≈ 8 m/o La_2O_3) and the second phase (≈ 36 m/o La_2O_3) and the bulk composition (16 m/o La_2O_3) of sample C indicated a ≈ 29 v/o second-phase content at 1950°C according to the lever rule. This volume percent agreed reasonably with that indicated by the TEM observation.

The present results and the data obtained by Horwath³ are compared to the values indicated by the Y_2O_3 - La_2O_3 phase diagram (Figure 1). The Y_2O_3 - La_2O_3 phase diagram in Figure 1 was from Ref. 1. The high La_2O_3 content of the second phase in sample C was consistent with the results (24 m/o and 38 m/o La_2O_3 contents) of AEM analyses³ on the second-phase particles in 9 m/o La_2O_3 -doped Y_2O_3 samples quenched from 2100°C or 2200°C; the La_2O_3 contents in the second phase were all higher than the values indicated by the C&H/H phase boundary. During cooling, the compositions of the second phase could shift to higher La_2O_3 contents as the second phase passed through the C&B phase field which had a phase boundary at high La_2O_3 contents (≈ 35 m/o). This could explain the high La_2O_3 content of the second phase in sample C. The composition of the matrix phase in sample C was consistent with the extrapolation (10 m/o La_2O_3) to 1950°C from the data³ on 2100°C (8 m/o La_2O_3) and 2200°C (6 m/o La_2O_3). Thus, the present results suggested adjustments to the C/C&H phase boundary of the C&H phase field.

TEM In-Situ Fracture Experiments

TEM in-situ fracture experiments were conducted on sample C. As the stress was applied, two major cracks were initiated at the edge of the hole in the TEM specimen and propagated in a direction almost normal to the tensile axis. In addition, several microcracks developed in the areas around the hole (Figure 10). The areas along the fully developed main cracks were relatively thick and revealed evidence of crack deflection on STEM back-scattered images.

Interactions of cracking with the microstructure were readily observed along the microcracks. Several modes of crack propagation along the microcracks were evident: (1) transgranular cleavage and intergranular fracture in the equiaxed cubic matrix (Figure 11), (2) crack deflection by the lathlike, monoclinic second-phase particles (Figure 12), and crack branching in the cubic matrix (Figure 13), (3) crack arrest at the interface of the second phase and matrix (Figure 14), and (4) zigzag cracks in the lathlike monoclinic second-phase particles having twinned substructure (Figure 15).

The cleavage plane in cubic Y_2O_3 is $\{111\}$.⁶ The same cleavage plane is thought to be operative in the cubic phase of La_2O_3 -doped Y_2O_3 . The second phase in sample C is of monoclinic symmetry and, therefore, does not have an easy cleavage plane. The substantial amount of crack deflection at the cubic matrix/monoclinic second-phase interface appears to be related to (1) the difference in the cleavage behavior of the cubic phase vs. the monoclinic phase and (2) the strain field surrounding the second phase caused by the volume change associated with the H→B phase transition along with mismatch in thermal expansion and elastic modulus between the phases. The indentation fracture toughness ($1.5 \text{ MN}\cdot\text{m}^{-3/2}$) in the 16 m/o La_2O_3 -doped, sintered and annealed, two-phase sample C was appreciably higher than that ($0.9 \text{ MN}\cdot\text{m}^{-3/2}$) of the standard 9 m/o La_2O_3 -doped, sintered and annealed, single-phase material.² The toughening mechanism must be related to the above interactions, including deflection of cracking by the lathlike second-phase particles dispersed inside the cubic matrix grains.

SUMMARY AND CONCLUSIONS

In summary, AEM studies showed the composition in a single-phase, 9 m/o La_2O_3 -doped, sintered ($2200^\circ\text{C}/2 \text{ hr}$) and annealed Y_2O_3 sample to be uniform, indicating that the $1950^\circ\text{C}/6 \text{ hr}$ anneal was sufficient for homogenization. A two-phase, 16 m/o La_2O_3 -doped, sintered (2150°C for 90 min) and annealed (1950°C for 6 hr) sample showed intragranular, lathlike, monoclinic second-phase particles in an equiaxed cubic matrix. Microchemical analyses indicated $\cong 34 \text{ m/o}$ – 38 m/o La_2O_3 in the intragranular second phase and $\cong 6.1 \text{ m/o}$ – 9.1 m/o La_2O_3 in the cubic matrix, suggesting adjustments to the C/C&H phase boundary in the Y_2O_3 - La_2O_3 phase diagram. The symmetry of the intragranular second phase was identified as monoclinic through SAED and CBED. Some of the lathlike, intragranular, monoclinic second-phase particles exhibited twin-like features, while others appeared defect free. The twin plan was $(31\bar{3})_m$. The $(\bar{2}2\bar{2})_c$ and $(402)_m$ planes were approximately parallel in adjacent phases.

Deflection of crack, by the cubic matrix/intragranular, monoclinic second-phase interface, was observed in TEM in-situ fracture experiments and believed to be one of the mechanisms responsible for the toughening in the two-phase material.

REFERENCES

1. W.H. Rhodes, "Controlled Transient Solid Second-Phase Sintering of Yttria," *J. Am. Cer. Soc.* 64 [1], 12-19 (1981).
2. W.H. Rhodes, G.C. Wei, and E.A. Trickett, "Lanthana-doped Yttria: A New Infrared Window Material," Society of Photo-Optical Instrumentation Engineers (SPIE) Proc. Conf. of Infrared and Optical Transmitting Materials, San Diego, California (August 1986), in press.
3. S. Horwath, "Analytical Electron Microscopy Studies in the Y_2O_3 - La_2O_3 System," M.S. Thesis, Lehigh University, Bethlehem, Pennsylvania (1985).
4. P.E. Caro, et al., "Defects and Impurities Influences on Phase Transformation in Rare Earth Oxides," *Defects and Transport in Oxides*, ed. S. Seltzer and R. I. Jaffee, Plenum Press, New York, 519-535 (1974).
5. H.R. Hoekstra, "Phase Relationships in the Rare Earth Sesquioxides at High Pressure," *Inorganic Chemistry* 5, 754 (1966).
6. W.S. Brown and E.N. Farabaugh, "Dislocation Etchant for Single Crystal Y_2O_3 ," *J. Am. Cer. Soc.* 53, [4] 225 (1970).

Table I
TEM microchemical analysis results on two-phase sample C

SIGNAL	k-FACTOR	PHASE	THICKNESS (nm)	La ₂ O ₃ (m/o)
Y L Line	0.55	Matrix	150	9.1
La L Line		Matrix	25	8.8
		Matrix	200	7.7
		Matrix	175	6.7
Y K Line	1.11	Intragranular Second Phase	80	35.9
La L Line		Intragranular Second Phase	150	38.0
		Intragranular Second Phase	25	34.0

FIGURE CAPTIONS

- Figure 1. Y_2O_3 -rich portion of the La_2O_3 - Y_2O_3 phase diagram.
- Figure 2. STEM micrographs of single-phase sample B (a) and (b) and line scan (Y and La) across one grain boundary (c). The "spots" in (a) and (b) probably resulted from selective etching during ion milling.
- Figure 3. Bright field TEM micrograph showing twinlike features in second phase particles, (a), and defect-free second phase particles, (b).
- Figure 4. EDXA spectra of matrix phase (C) and second phase (B) in two-phase sample C.
- Figure 5. STEM micrograph of two-phase sample C showing second phase particles (a), and line scans for Y (b), and La (c).
- Figure 6. TEM micrograph (a) showing the second phase, (B) and matrix (C), and CBED patterns of the matrix (b) and (c), and microdiffraction pattern of the second phase (d).
- Figure 7. SAED pattern of the phases (B) and (C) shown in Figure 6(a).
- Figure 8. Indexing of SAED pattern formed the phases (B) and (C) shown in Figure 6(a). Zone axis is $[110]_c$ and the foil plane is parallel to $(132)_m$.
- Figure 9. Electron diffraction diagram of the monoclinic second phase in two-phase sample C, (a). The zone axis is $[10\bar{1}]_m$. The SAED pattern in twinned second phase, (b), has a symmetry with respect to $[313]_m$, indicating $(313)_m$ as a twin plane.
- Figure 10. Schematic sketch showing TEM in-situ fracture experiment to identify interactions of crack propagation with second phase.
- Figure 11. Cleavage and intergranular cracking in two-phase sample C.
- Figure 12. Crack deflection by lathlike, second-phase particle in two-phase, toughened sample C.

Figure 13. Crack branching in two-phase, toughened sample C.

Figure 14. Crack arrest at the interface of the second phase and matrix in two-phase sample C.

Figure 15. Zigzag cracking path through twinned second phase in two-phase sample C.

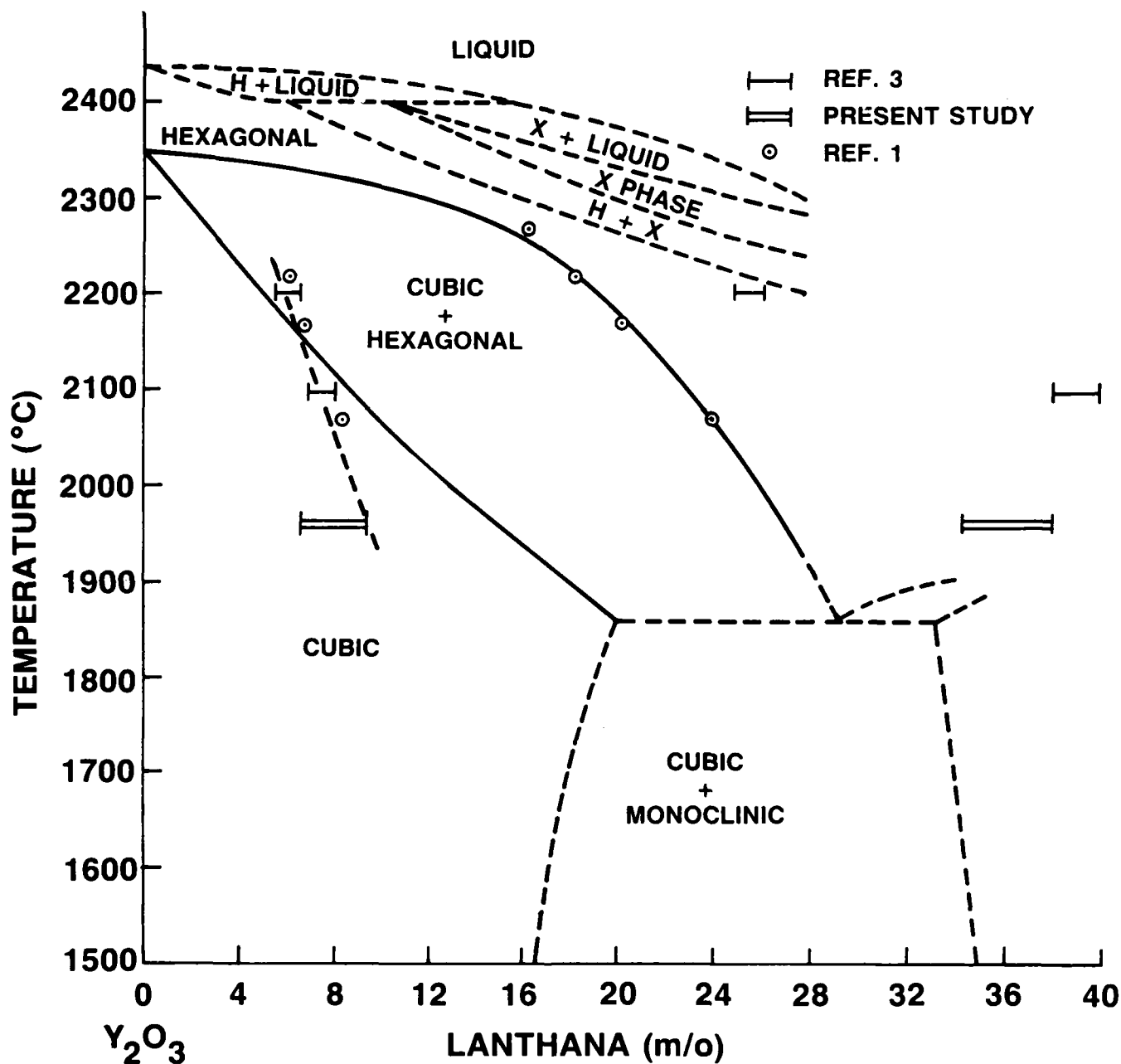
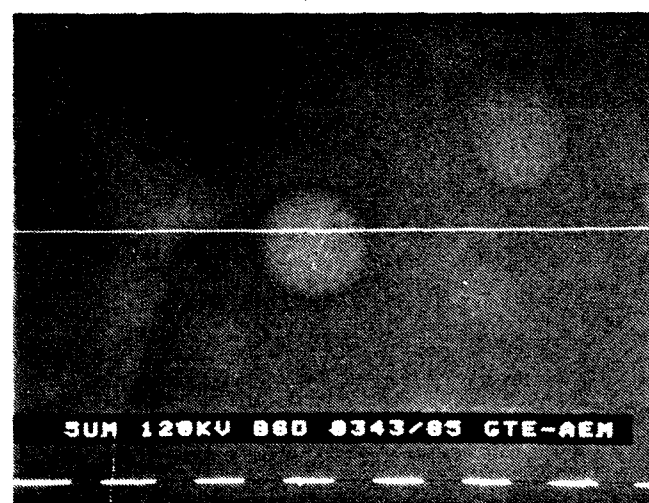


Figure 1. Y_2O_3 -rich portion of the La_2O_3 - Y_2O_3 phase diagram.

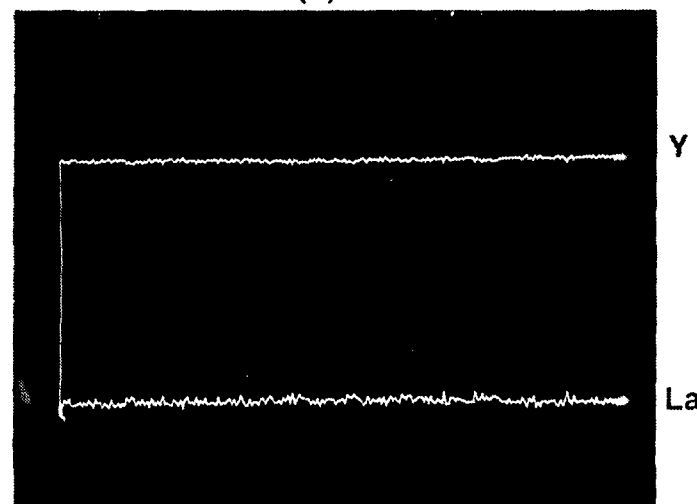


50 μm

(a)



(b)



(c)

Figure 2. STEM micrographs of single-phase sample B (a) and (b) and line scan (Y and La) across one grain boundary (c). The "spots" in (a) and (b) probably resulted from selective etching during ion milling.

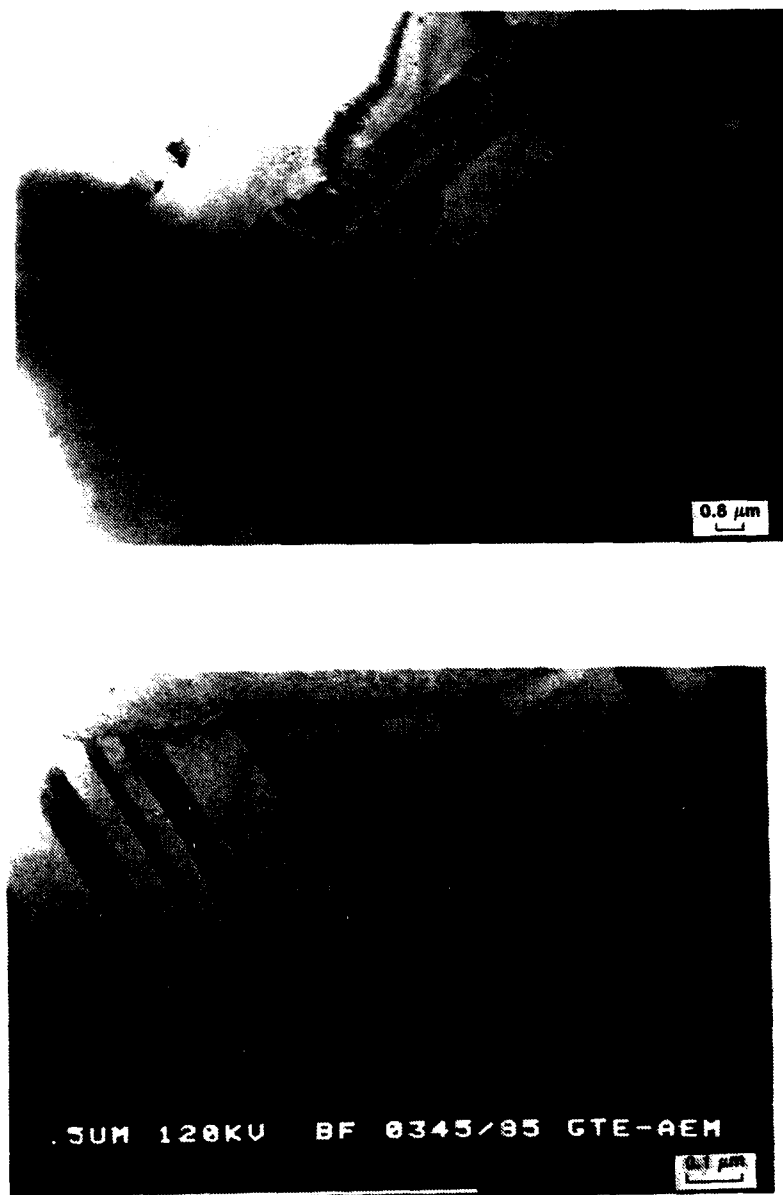


Figure 3. Bright field TEM micrograph showing twinlike features in second phase particles, (a), and defect-free second phase particles, (b).

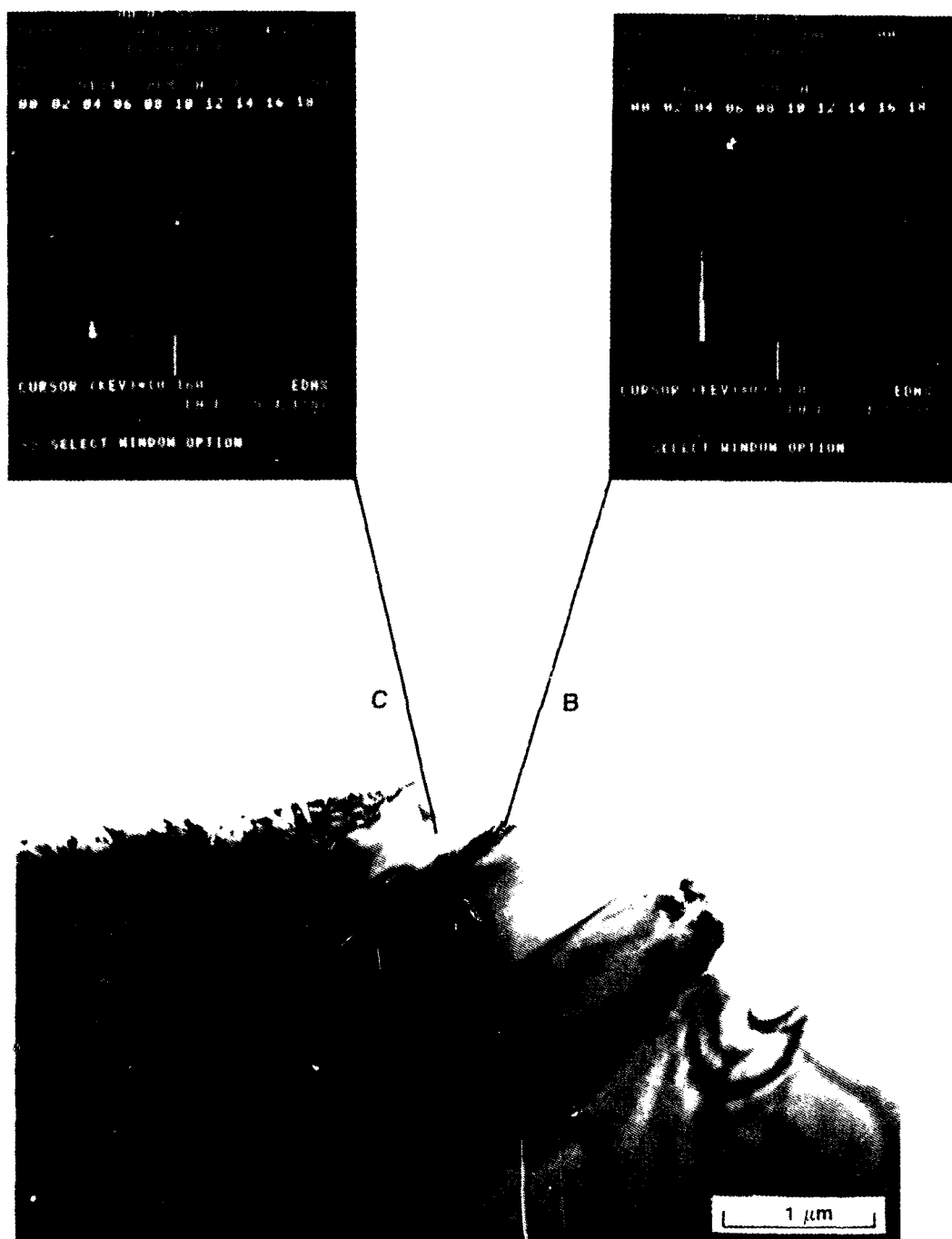
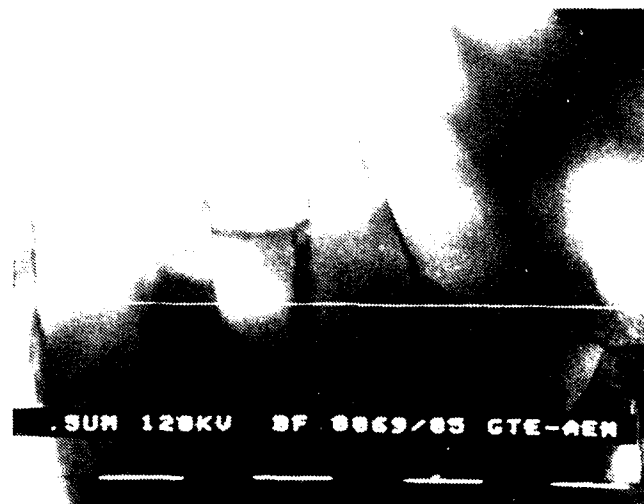


Figure 4. EDXA spectra of matrix phase (C) and second phase (B) in two-phase sample C.



(a)



Y

(b)



La

(c)

Figure 5. STEM micrograph of two-phase sample C showing second phase particles (a), and line scans for Y (b), and La (c).

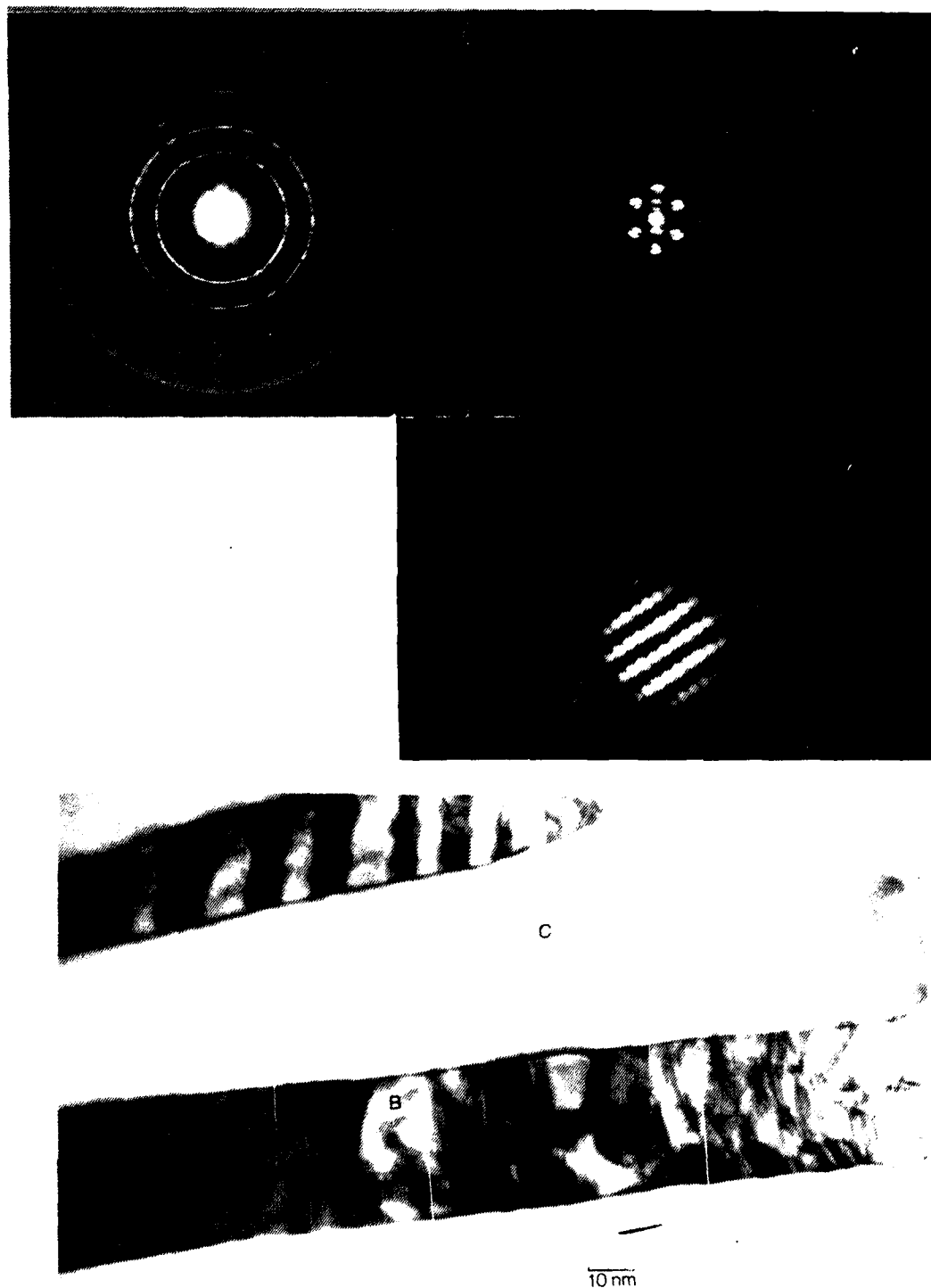


Figure 6. TEM micrograph (a) showing the second phase, (B) and matrix (C), and CBED patterns of the matrix (b) and (c), and microdiffraction pattern of the second phase (d).

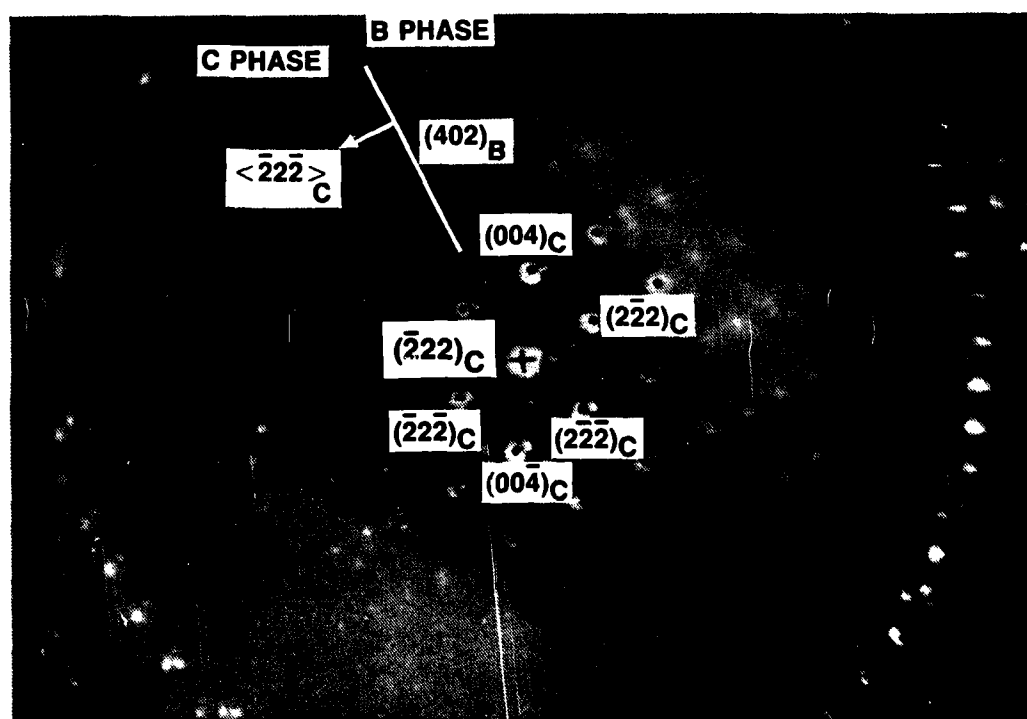


Figure 7. SAED pattern of the phases (B) and (C) shown in Figure 6(a).

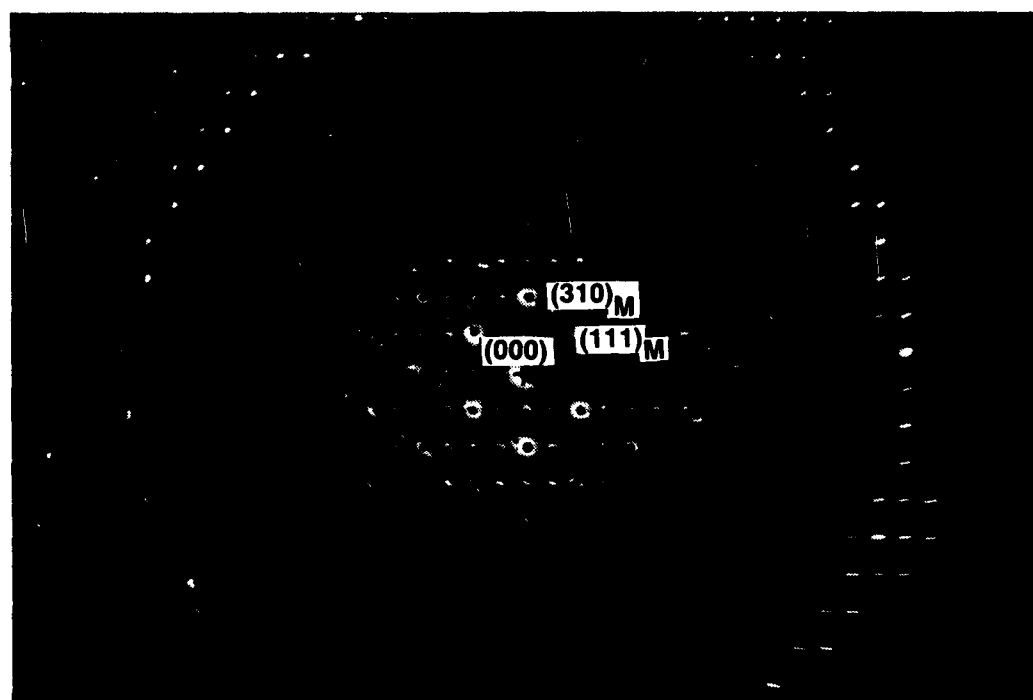


Figure 8. Indexing of SAED pattern formed the phases (B) and (C) shown in Figure 6(a).
 Zone axis is $[110]_c$ and the foil plane is parallel to $(132)_m$.

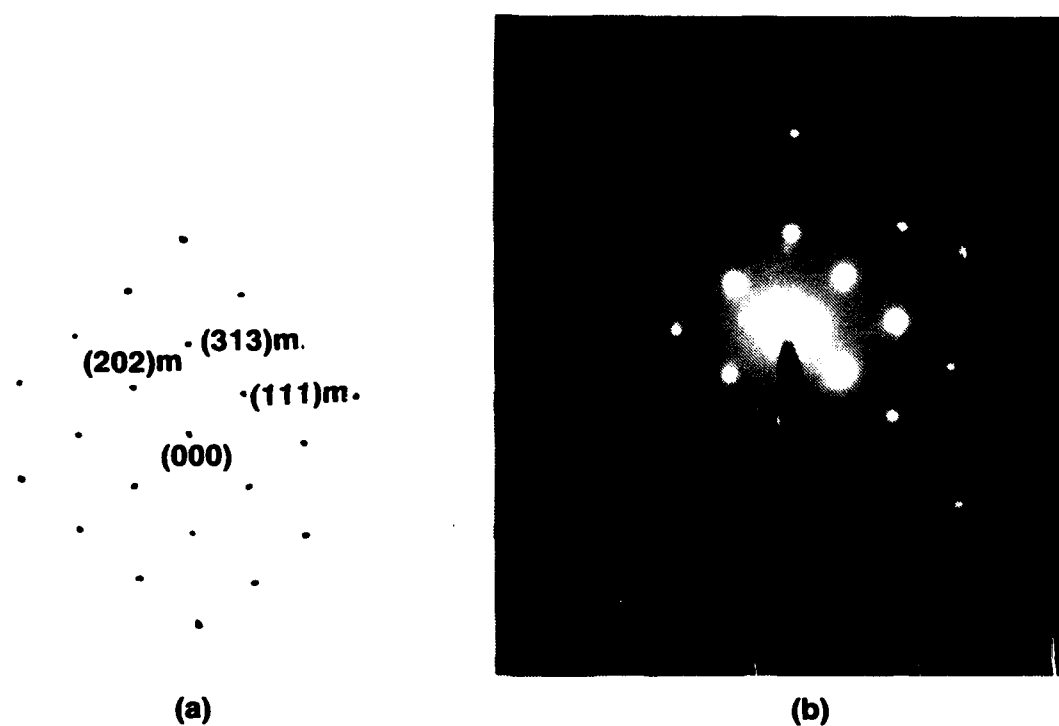


Figure 9. Electron diffraction diagram of the monoclinic second phase in two-phase sample C, (a). The zone axis is $[10\bar{1}]_m$. The SAED pattern in twinned second phase, (b), has a symmetry with respect to $[313]_m$, indicating $(313)_m$ as a twin plane.

- TEM in-situ fracture experiment to identify interaction of crack propagation with second phase.

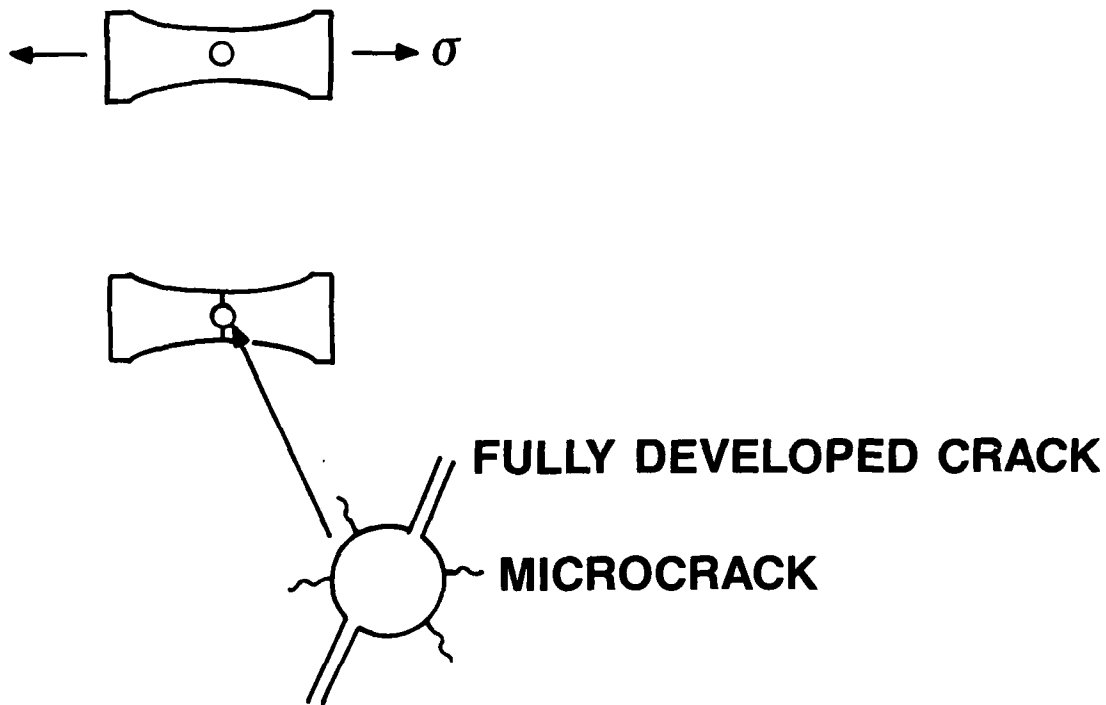


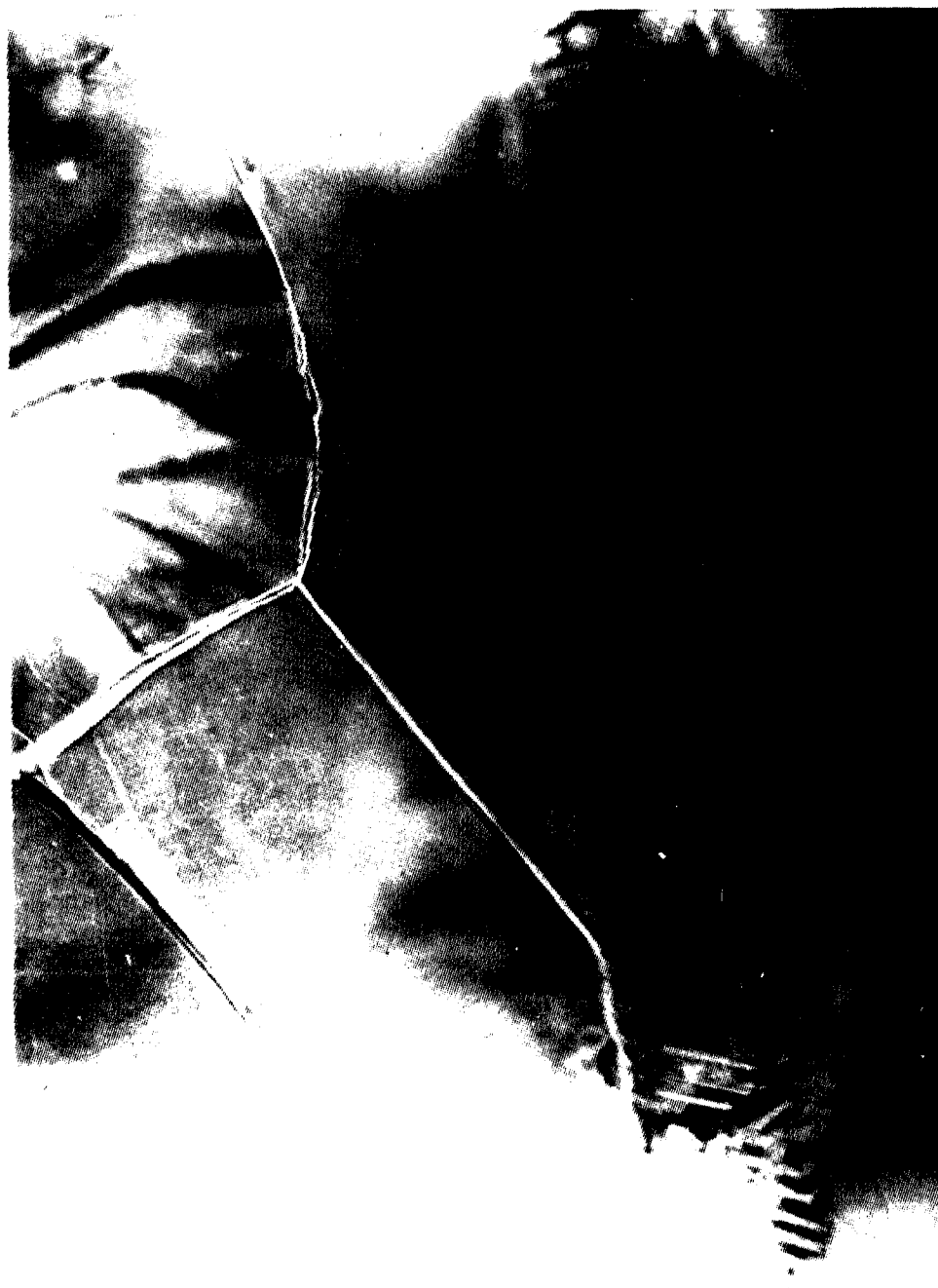
Figure 10. Schematic sketch showing TEM in-situ fracture experiment to identify interactions of crack propagation with second phase.



Figure 11. Cleavage and intergranular cracking in two-phase sample C.



Figure 12. Crack deflection by lathlike, second-phase particle in two-phase, toughened sample C.



0.1 μm



Figure 13. Crack branching in two-phase, toughened sample C.

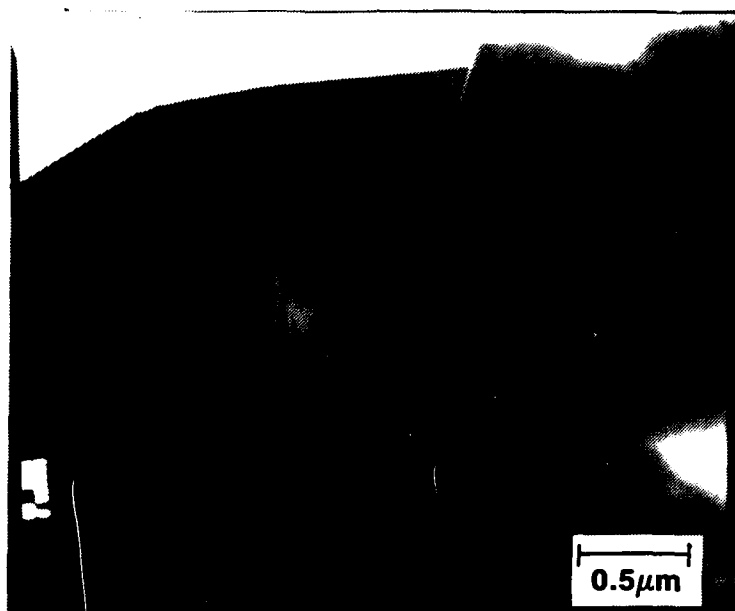


Figure 14. Crack arrest at the interface of the second phase and matrix in two-phase sample C.

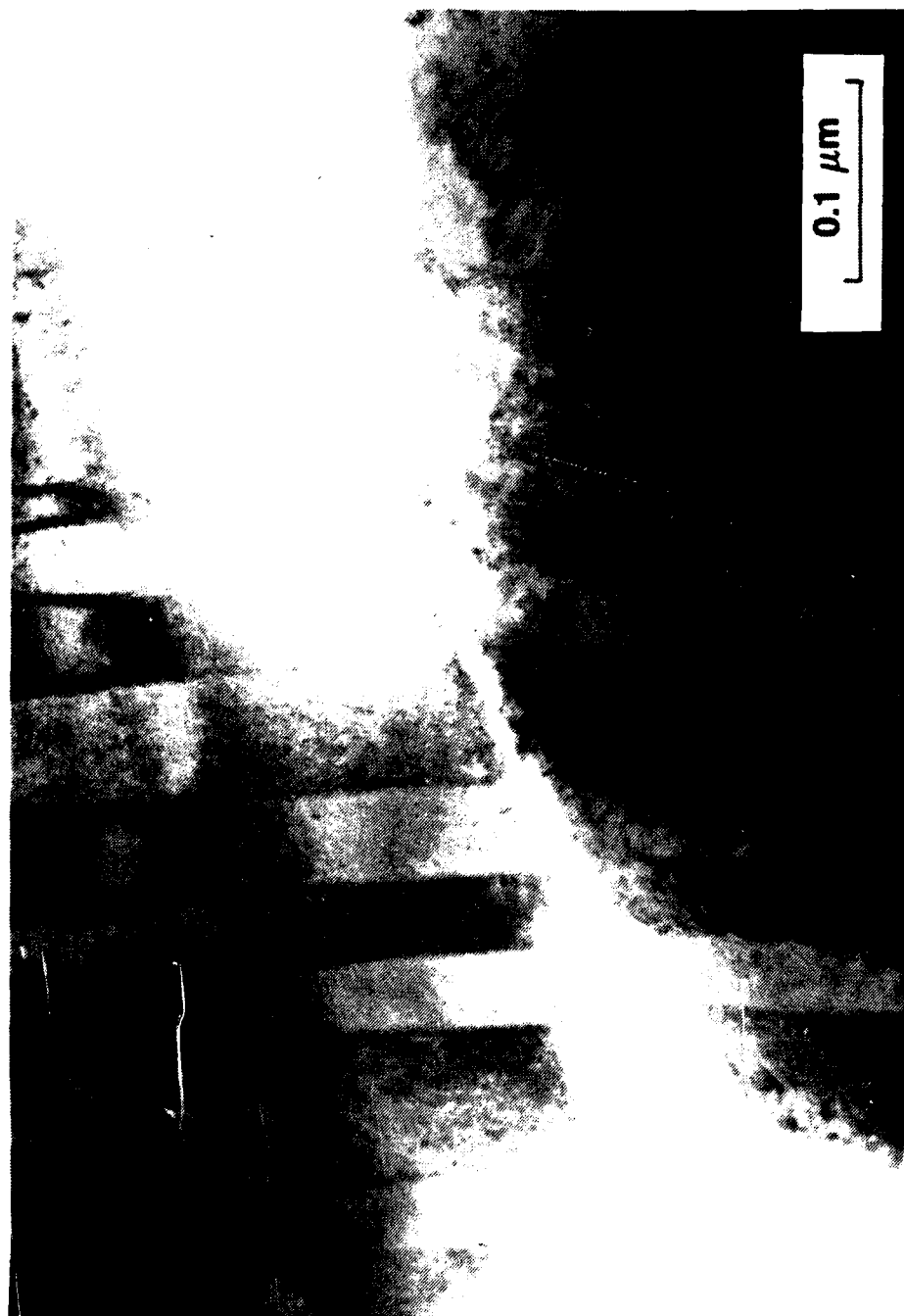


Figure 15. Zigzag cracking path through twinned second phase in two-phase sample C.

**EXTRINSIC OH⁻ ABSORPTION IN TRANSPARENT
POLYCRYSTALLINE LANTHANA-DOPED YTTRIA**

by

G.C. Wei

Extrinsic OH⁻ absorption in transparent polycrystalline lanthana-doped yttria*

G.C. Wei
GTE Laboratories Inc., 40 Sylvan Road, Waltham, MA 02254

ABSTRACT

Transparent lanthana-doped yttria fabricated by transient solid second-phase sintering under wet hydrogen typically has a broad absorption band with a peak at 3.08 μm . The absorption band shift observed in samples treated in wet deuterium indicated that the 3.08 μm absorption was due to OH⁻ ions. The diffusion rates of hydrogen defects in lanthana-doped yttria were determined in the temperature range from 1000 to 1400°C. The changes in the concentrations of OH⁻ ions upon anneals were determined by measuring infrared absorbance at 3.08 μm . The diffusion coefficient is 1.3×10^{-7} , 9.9×10^{-7} , and 4.1×10^{-6} cm²/s at 1000, 1200, and 1400°C, respectively, with an activation energy of 140 kJ/mol. Annealing in a controlled oxygen partial-pressure environment can remove the OH⁻ absorption band and bring the total absorption in the 3 to 5 μm range closer to the intrinsic values.

I. INTRODUCTION

Lanthana-doped yttria is a transparent ceramic material made by a transient solid second-phase sintering technique.¹ It has the cubic-type rare-earth-oxide crystal structure. The structure can be described as a modified fluorite-type cubic structure with one-fourth of the anion sites vacant. This material has low intrinsic absorption in the infrared (3 to 5 μm) and transmits over the wavelength range of 300 nm to 9 μm .

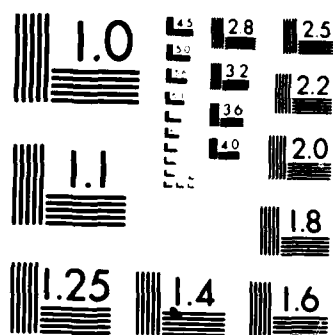
*Work partially supported by the Office of Naval Research. Paper presented at the American Ceramic Society Annual Meeting, Cincinnati, OH, 1985.

AD-A170 821 PROCESSING STUDIES FOR OPTICALLY TRANSPARENT
LA(2)O(3)-DOPED Y(2)O(3)(U) GTE LABS INC WALTHAM MA
W H RHODES ET AL. 31 JUL 86. TR-86-810.1
UNCLASSIFIED N00014-82-C-0452 F/G 20/

UNCLASSIFIED N00014-82-C-0452

F/G 20/6

NL



MICROCOPY RESOLUTION TEST CHART
NATIONAL BUREAU OF STANDARDS-1963-A

The absorption in La_2O_3 -doped Y_2O_3 in the 3 to 5 μm range can be described as either intrinsic or extrinsic. The relationship between absorption coefficient and wavelength for 9 m/o La_2O_3 -doped Y_2O_3 is shown in Figure 1, which illustrates the effect of extrinsic absorption. The absorption coefficients were measured using a two-thickness technique. Theoretically, $\log [\text{absorption coefficient}]$ is proportional to wavelength for wavelengths several times greater than the cutoff wavelength. The straight line in Figure 1 is the experimental data confirming the theoretical linear dependence, and the extrapolation is extended to the 3–5 μm range to obtain the intrinsic absorption coefficient. The extrapolated multiphonon edge shows that the intrinsic absorption coefficient is on the order of 10^{-3} to 10^{-4} cm^{-1} . The actual absorption coefficient in the current materials is typically on the order of 10^{-1} to 10^{-2} cm^{-1} , which is about one to two orders of magnitude higher than the intrinsic absorption. This is caused by extrinsic absorption in the samples. The extrinsic absorption can be due to stoichiometry-related point defects, impurities such as OH^- and possibly rare-earth and transition metals, and surface defects and impurities. All of these are believed to make significant contributions to the total absorption. One major source of the extrinsic absorption is a strong absorption band near 2.7 to 3.5 μm , with a peak at 3.08 μm (3246 cm^{-1}). This is indicated by the fact that the absorption coefficient increases significantly as λ approaches 3 μm (Figure 1).

This paper presents the results of a study on understanding the cause and removing this absorption band. Also reported in this paper are high-temperature diffusion rates of the defects responsible for the 3.08- μm absorption band.

II. EXPERIMENTAL PROCEDURES

Several 9 m/o La_2O_3 -doped Y_2O_3 disks were used in annealing experiments on deuteration, determination of hydrogen defect diffusivity, and OH^- removal. Typical chemical analyses have shown the following impurities: Si (14 ppm), Cl (7 ppm), Ca (7 ppm), S

(6 ppm), Ce (5 ppm), Na (4 ppm), Fe (3 ppm), Al (3 ppm), Mg (2 ppm), and K (1 ppm). The sizes of the samples used in the experiments ranged from 10 mm dia \times 1 mm thick to 19 mm dia \times 6 mm thick. The annealing experiments were conducted in an alumina tube furnace. The ID of the alumina muffle was 38 mm. Various gases, including Ar - 5 ppm O₂, Ar - 1 ppm O₂, wet (H₂O)-D₂, wet (D₂O)-D₂, O₂, and CO-CO₂ mixtures, were used. The flow rate of the gases was 1250 °C mm³/s. Samples were placed on an alumina boat which was centered in the furnace. The furnace was first purged with the appropriate gas for 30 min, and then the gas flow rate was adjusted to 1250 mm³/s. The temperature was increased from room temperature to a predetermined temperature in 1 hr, held for a predetermined time, and cooled to room temperature in 1 hr. The treated samples were polished lightly to remove the surface effect of thermal etching and then cleaned with acetone and CCl₄. The infrared absorption spectra in the samples before and after the anneals were compared on an FTIR spectrophotometer.* Anneals for determination of diffusivity of hydrogen defects were conducted in Ar - 1 ppm O₂ atmosphere. The concentrations of hydrogen defects in the samples were monitored with infrared absorbance of OH⁻ ions at 3.08 μ m (3246 cm⁻¹). The diffusion coefficients for hydrogen defects at elevated temperatures were obtained from the following equation.²

$$\frac{A_0 - A_t}{A_0 - A_\infty} = \frac{2}{d} \cdot \frac{1}{\sqrt{\pi}} \cdot \sqrt{Dt} \quad (1)$$

where

A_0 = Initial OH⁻ absorbance at 3246 cm⁻¹

A_t = OH⁻ absorbance after anneal for time (t)

A_∞ = Baseline absorbance in the 3 to 5 μ m range

d = Half-thickness of sample

*Nicolet 20DX FTIR spectrophotometer.

The use of Equation (1) required $\sqrt{4Dt} \ll 2d$. Diffusion experiments were designed so that $\sqrt{4Dt}$ was smaller than the sample thickness.

III. RESULTS AND DISCUSSION

A typical FTIR spectrum of La_2O_3 -doped Y_2O_3 samples illustrating the 3246 cm^{-1} ($3.08\text{ }\mu\text{m}$) absorption band is shown in Figure 2. The shape of the transmittance curve and the phonon edge are well defined. Samples were 10 mm dia \times 2 mm thick. The strong and broad absorption band is clearly discernible. A similar absorption band at $3\text{ }\mu\text{m}$ has been reported in single-crystal Y_2O_3 ,^{3,4} although the sources of the absorption peak were not specifically identified. The as-processed La_2O_3 -doped Y_2O_3 samples were treated at 1400°C in Ar - 5 ppm O_2 for 4 hr, and the samples were cooled to room temperature in about 1 hr. The FTIR spectrum of the treated samples (Figure 3) showed that the $3.08\text{-}\mu\text{m}$ absorption band apparent in the as-processed samples disappeared as a result of the controlled-atmosphere anneal. Figure 1 also shows that the 3246 cm^{-1} ($3.08\text{ }\mu\text{m}$) absorption band appeared to have three additional peaks at 3437 cm^{-1} ($2.91\text{ }\mu\text{m}$), 2920 cm^{-1} ($3.43\text{ }\mu\text{m}$), and 2846 cm^{-1} ($3.51\text{ }\mu\text{m}$). In the Ar - 5 ppm O_2 -treated samples, the absorption peaks were eliminated.

Similar treatment in pure oxygen also removed the absorption band. However, anneals under mixtures of CO and CO_2 did not significantly affect the absorption bands. This might be because of the reaction $3\text{H}_2 + \text{CO} \rightarrow \text{H}_2\text{O} + \text{CH}_4$ in the boundary layer adjacent to the samples; hydrogen diffused out of the samples reacted with CO to form H_2O which, in turn, provided a source of hydrogen to diffuse back into the samples. In samples treated with wet (D_2O) hydrogen, the FTIR spectra again showed the $3.08\text{ }\mu\text{m}$ band. This was because the reactions among D_2O , H_2 , O_2 , H_2O , and D_2 under flowing 1-atm P_{H_2} would produce only

a small amount of D_2 and D_2O available for $OD^- - OH^-$ exchange in the samples at $1400^\circ C$. Therefore, deuteration experiments were conducted using wet (D_2O) deuterium. Samples were treated at $1400^\circ C$ under wet (D_2O) D_2 with a dew point of $23^\circ C$.

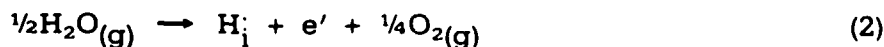
The FTIR spectrum of the deuterized samples clearly showed a new absorption band at 2420 cm^{-1} ($4.13\text{ }\mu m$), Figure 4. Several side peaks at 2515 cm^{-1} ($3.98\text{ }\mu m$), 2396 cm^{-1} ($4.20\text{ }\mu m$), and 2660 cm^{-1} ($3.76\text{ }\mu m$) were also observed. The shifts in the absorption bands are listed in Table I. The shift of the major absorption peak from 3246 cm^{-1} to 2420 cm^{-1} (a factor of 1.34) upon deuteration agrees very well with the theoretical shift. For perfect bond stretching, the frequency of the OH^- vibration should be, in theory, larger than that of OD^- by a factor of 1.37. The results clearly showed that the $3.08\text{-}\mu m$ (3246 cm^{-1}) absorption band was due to OH^- rather than oxygen vacancies. The shifts in the side bands (Table I), in the range of 1.16 to 1.29, were in reasonable agreement with the theoretical shift (1.37). The entire infrared spectrum, including the side peaks in the as-processed and wet deuterium-treated samples, were complex and only the major peaks were interpreted. The side peaks have not been unambiguously assigned. They might be related to the many possible distributions and orientations of OH^- ions in the lattice and interactions with point defects and impurities. One possibility is the associated defect of interstitial OH^- ions, OH_i' , and $V_{\ddot{O}}$, since the negatively charged OH_i' would attract $V_{\ddot{O}}$. Positive holes trapped to OH_i' could also shift the infrared line. Interactions of OH_i' with tetravalent impurity cations such as Si^{+4} or monovalent anions such as Cl^- are unlikely because they are associated with V_Y''' or O_i'' , which repel OH_i' . Divalent and monovalent cations could introduce $V_{\ddot{O}}$ which, in turn, attracts OH_i' to form $OH_i' - V_{\ddot{O}}$ - metal impurity complexes that could cause the side bands at longer wavelengths. In as-processed and deuterized samples, there were no observable absorption peaks for the molecular stretching frequencies (4164 cm^{-1} and 2935 cm^{-1}) of gaseous H_2 and D_2 in voids.⁵ The absorption peaks ($\cong 3600\text{ cm}^{-1}$) for $Y(OH)_3$, $YOOH$, and $La(OH)_3$ (see Reference 6) were not observed.

Examples of the infrared absorption spectra in as-sintered and diffusion-annealed samples are shown in Figure 5. The OH^- absorbance at 3246 cm^{-1} showed a decrease in the 2-mm-thick sample annealed at 1400°C for 20 min in flowing Ar - 1 ppm O_2 atmosphere. The reduction in the OH^- absorption is clearly due to diffusion of hydrogen defects out of the sample during the anneal. Diffusion rates calculated from Equation (1) are 1.3×10^{-6} , 9.9×10^{-7} , and $4.1 \times 10^{-6}\text{ cm}^2/\text{s}$ at 1000, 1200, and 1400°C , respectively (Figure 6). The Arrhenius relation obtained for the temperature range from 1000 to 1400°C is $D = 0.13 \exp(-140\text{ kJ/mol}/RT)$, where RT has the usual meaning. The diffusion coefficients of hydrogen defects in La_2O_3 -doped Y_2O_3 are about one to three orders of magnitude higher than those, $D = 7.24 \exp(-245\text{ kJ/mol}/RT)$, of oxygen defects in pure Y_2O_3 .⁷ The activation energy (140 kJ/mol) is lower than that (245 kJ/mol) for oxygen defect diffusion in Y_2O_3 . The hydrogen diffusivity in La_2O_3 -doped Y_2O_3 is higher than that ($1 \times 10^{-6}\text{ cm}^2/\text{s}$ at 1600°C)⁸ in single-crystal MgO , and on the same order as that of tritium ($\cong 10^{-6}\text{ cm}^2/\text{s}$ at 1400°C)⁹ in single-crystal Al_2O_3 . The hydrogen diffusivity in La_2O_3 -doped Y_2O_3 is also in good agreement with the extrapolated diffusion of tritium in pure Y_2O_3 at 1400°C ($3 \times 10^{-6}\text{ cm}^2/\text{s}$).¹⁰

An alternate method of eliminating the OH^- absorption involved sintering and annealing in dry H_2 , followed with a final stoichiometry adjustment in Ar - 5 ppm O_2 at 1400°C . The samples prepared under dry H_2 were black. The IR transmittance was too low to ascertain whether there was any OH^- absorption. Samples became transparent and free of the OH^- absorption after the Ar - 5 ppm O_2 stoichiometry adjustment. The time required for the $5 \times 10^{-6}\text{ atm } P_{\text{O}_2}$ stoichiometry adjustment was 88 hr for 5-mm-thick samples. A color boundary diffusion front was observed to migrate about 1.3 mm during the first 4-hr anneal. This indicated an oxygen defect diffusivity of $3 \times 10^{-7}\text{ cm}^2/\text{s}$, about a factor of 10 smaller than the hydrogen defect diffusivity. The stoichiometry adjustment in this procedure could be conducted in mixtures of CO and CO_2 with optimum P_{O_2} (10^{-10} to 10^{-13}) atm for maximum transmittance, as indicated by the results on stoichiometry studies.¹¹

In another experiment, transparent samples were made by sintering in dry H_2 at 2150°C and annealing in Ar – 5 ppm O_2 at 1950°C for 3 hr. Additional time (6 hr) in the Ar – 5 ppm O_2 , 1950°C anneal actually converted the transparent samples (3 hr in Ar – 5 ppm O_2 at 1950°C) to slightly grayish, indicating that the local P_{O_2} at 1950°C inside the W-element, Mo-heat-shield furnace was much lower than the intended 5×10^{-6} atm. During the first 3 hr (1950°C/Ar – 5 ppm O_2) run, the residual water which was adsorbed on the furnace cooling tubings, elements, and shields probably was released, resulting in an oxidizing atmosphere ($> 10^{-13}$ atm P_{O_2}). In the subsequent 6 hr/1950°C/Ar – 5 ppm O_2 run, the reactions of the furnace element and shields with oxygen in the furnace atmosphere could effectively decrease the P_{O_2} to less than 10^{-13} atm. Nevertheless, the samples so prepared exhibited the OH^- absorption band. The OH^- absorption band in this particular sample could also be explained by the high temperature (1950°C) used in the experiment, since the equilibrium hydrogen defect concentration increases exponentially with temperature at a constant P_{H_2O} (< 1 ppm) in the Ar – 5 ppm O_2 environment. It was found that the OH^- absorption band could be restored by annealing in wet hydrogen for the samples in which the OH^- absorption was first removed by heat treatment in Ar – 5 ppm O_2 . Attempts to outgas powders prior to sintering did not eliminate the OH^- absorption. These findings suggest that the sources of the OH^- impurities are (1) wet H_2 used in the sintering and annealing cycle, and (2) residual water content in the starting powder.

Norby and Kofstad¹² recently studied hydrogen defects in pure Y_2O_3 in the range of P_{H_2O} from 30 ppm to 1.6×10^{-2} atm in air and oxygen. They argued that, since literature studies¹³⁻¹⁵ showed disorders on oxygen sublattice as dominating point defects, only O_i'' and V_O^\bullet should be considered when discussing the hydrogen defects. Two types of hydrogen defects, interstitial H_i^\bullet and interstitial OH_i' , were proposed as the dominating hydrogen defects. The formation of proton (H_i^\bullet) was described by¹²



with an equilibrium constant $\propto P_{H_2O}^{-1/2} P_{O_2}^{1/4}$. The OH_i' can be viewed as a proton bonded to an O_i'' . The possibility of OH_i' , i.e., OH^- ions substituting directly for O_O , is considered unlikely because it would involve the formation of $YOOH$ or $Y(OH)_3$, which was not detected in the IR spectra. Hydrogen in the form of H^- ions was also considered unlikely because the H^- ion vibration frequency should be much lower than the 3246 cm^{-1} wavenumber of the OH^- extrinsic band. The formation of OH_i' was described by¹²



with an equilibrium constant proportional to $P_{H_2O}^{-1/2} P_{O_2}^{-1/4}$. Both Equations (2) and (3) predict that the equilibrium concentrations of hydrogen defects in Y_2O_3 - La_2O_3 would vary directly as the square root of P_{H_2O} . At constant P_{H_2O} , the equilibrium concentrations of hydrogen defects increase exponentially with temperature. Norby and Kofstad¹² constructed defect concentration diagrams consistent with their results of electrical conductivity vs P_{H_2O} for both lower-valent doped and undoped Y_2O_3 . In our materials, the higher and lower valent impurities are on the same order within the accuracy of spark-source mass spectrometry. The case of "undoped Y_2O_3 " should be considered. Norby and Kofstad¹² showed that as P_{H_2O} increased in a constant P_{O_2} oxidizing atmosphere, the hole concentration remained constant for a range of P_{H_2O} , and then decreased with increasing P_{H_2O} due to the increase in $[H_i']$. At high P_{H_2O} , the hole concentration again stayed constant, since $[H_i'] = [OH_i']$.

This relationship is useful for considering the changes in the concentrations of absorption-related defects: p , $[V_O^{\bullet}]$, $[O_i'']$, and $[OH_i']$ in the samples brought about by the Ar - 5 ppm O_2 treatment. According to our stoichiometry studies,¹¹ the 5×10^{-6} atm P_{O_2} treatment is an oxidizing atmosphere for Y_2O_3 - La_2O_3 . Therefore, the analysis by Norby and Kofstad is applicable to the defect equilibrium in 5×10^{-6} atm P_{O_2} . Note that the Kroger-Vink diagram for pure Y_2O_3 constructed by Tsuiki et al¹³ also indicates the Ar - 5 ppm O_2

atmosphere as an oxidizing environment. During the Ar - 5 ppm O₂ treatment, the as-processed Y₂O₃-La₂O₃ changes from an n-type conductor to a p-type conductor and the holes become the dominant carriers. The change in P_{H₂O} from 10⁻² atm (wet H₂ with a 23 °C dew point) to < 1 ppm in the Ar - 5 ppm O₂ atmosphere imparts additional increase in the hole concentration. Thus, during the Ar - 5 ppm O₂ treatment, the OH⁻ impurities are removed but the hole concentration and the concentration of holes trapped to O_i' would increase, which would somewhat offset the benefit of reduced OH⁻ concentration on the total infrared absorption.

Table II shows the transmittance of a typical as-sintered sample of 1-mm thickness. The relatively low transmittance at 3 μm was due to OH⁻ absorption. The sample was annealed in Ar - 5 ppm O₂ at 1400 °C for 2 hr. The data of the annealed samples showed relatively constant transmittance in the 3- to 5-μm range, indicating removal of the OH⁻ absorption. The absolute transmittance increased upon the Ar - 5 ppm O₂ anneal. This indicates that the infrared absorption of La₂O₃-doped Y₂O₃ can be improved by annealing in Ar - 5 ppm O₂.

IV. SUMMARY AND CONCLUSIONS

In summary, the OH⁻ related absorption in La₂O₃-doped Y₂O₃ was studied. The IR absorption in typical as-processed samples was orders of magnitude higher than the projected intrinsic absorption. The extrinsic absorption included a strong absorption band at 3.08 μm. Deuteration experiments and the absorption band shift unequivocally identified this band to be due to the stretching-mode vibration of OH⁻ impurities. The diffusion coefficients for hydrogen defects in La₂O₃-doped Y₂O₃ at 1000 to 1400 °C can be described by $D = 0.13 \exp(-140 \text{ kJ/mol} / RT) \text{ cm}^2/\text{s}$. A high-temperature (1400 °C) anneal in Ar - 5 ppm O₂ proved to be successful in eliminating the OH⁻ absorption band. During the treatment, hydrogen species diffuses out of the lattice and the stoichiometry readjusts with the net result of an appreciable reduction in the IR absorption coefficient.

V. REFERENCES

1. W.H. Rhodes, "Controlled Transient Solid Second-Phase Sintering of Yttria," *J. Am. Ceram. Soc.* 64, pp. 12-19 (1981).
2. Y. Nigara, "Measurement of the Optical Constants of Yttrium Oxide," *Jpn. J. Appl. Phys.* 7, pp. 404-408 (1968).
3. K.A. Wickersheim and R.A. Leferer, "Infrared Transmittance of Crystalline Yttrium Oxide and Related Compounds," *J. Opt. Soc. Am.* 51, p. 1147 (1961).
4. B. Henderson and W.A. Sibley, "Studies of OH⁻ and OD⁻ Ions in Magnesium Oxide. I. Distribution and Annealing of Hydroxyl and Deuteriohydroxyl Ions," *J. Chem. Phys.* 55 (3), pp. 1276-1285 (1971).
5. B.I. Swanson, C. Machell, G.W. Beall, and W.O. Milligan, "Vibrational Spectra and Assignments for the Lanthanide Trihydroxides," *J. Inorg. Nucl. Chem.* 40, pp. 694-696 (1978).
6. J. Crank, *The Mathematics of Diffusion*, Clarendon Press, Oxford (1956).
7. C.D. Wirkus, M.F. Berard, and D.R. Wilder, "Self-Diffusion of Oxygen in Y₂O₃ and Er₂O₃," *J. Am. Ceram. Soc.* 50 (2), p. 113 (1967).
8. R. Gonzales, Y. Chen, and K.L. Tsang, "Diffusion of Deuterium and Hydrogen in Doped and Undoped MgO Crystals," *Phy. Rev. B* 26 (3), pp. 4637-4645 (1982).
9. J.D. Fowler, D. Chandra, T.S. Ellman, A.W. Payne, and K. Verghese, "Tritium Diffusion in Al₂O₃ and BeO," *J. Am. Ceram. Soc.* 60 (3-4), pp. 155-161 (1977).
10. T.S. Elleman, L.R. Zumwalt, and K. Verghese, "Hydrogen Transport and Solubility in Non-Metallic Solids," *Proc. Topical Meet. Tech. Controlled Nucl. Fusion* 3 (2), pp. 763-770 (1978).
11. G.C. Wei, C. Brecher, and W.H. Rhodes, "Effects of Point Defects on High-Temperature Optical Properties in Transparent Polycrystalline Lanthana-Doped Yttria," *Soc. of Photo-Opt. Instrum. Eng. (SPIE) Proc., Conf. on Infrared and Opt. Transm. Mater.*, San Diego, CA, August 1986, in press.

12. T. Norby and P. Kofstad, "Electrical Conductivity and Defect Structure of Y_2O_3 as a Function of Water Vapor Pressure," *J. Am. Ceram. Soc.* 67 (12), pp. 786-792 (1984).
13. T. Tsuiki, T. Masumoto, K. Kitazawa, and K. Fueki, "Effect of Point Defects on Laser Oscillation Properties of Nd-Doped Y_2O_3 ," *Jpn. J. Appl. Phys.* 21 (7), pp. 1017-1021 (1982).
14. R.J. Bratton, "Defect Structure of Y_2O_3 - ZrO_2 Solid Solutions," *J. Am. Ceram. Soc.* 52 (4), p. 213 (1969).
15. P. Odier and J. Loup, "An Unusual Technique for the Study of Nonstoichiometry: The Thermal Emission of Electrons. Results for Y_2O_3 and TiO_2 ," *J. Solid State Chem.* 34, pp. 107-119 (1980).

Table I

OH⁻ and OD⁻ stretching frequencies in La₂O₃-doped Y₂O₃

ν (OH ⁻) (cm ⁻¹)	ν (OD ⁻) (cm ⁻¹)	ν (OH ⁻) / ν (OD ⁻)
2846	2396	1.19
2920	2515	1.16
3246	2420	1.34
3437	2660	1.29

Table II

Transmittance before and after Ar - 5 ppm O₂ treatment

Wavelength λ (μ m)	Room-Temperature Transmittance	
	As-Processed	After Ar - 5 ppm O ₂ Treatment
2	80.4	82.6
3	79.3	82.4
4	81.3	82.0
5	82.1	82.7
6	82.5	83.0

Figure 1. Absorption coefficient of as-processed La_2O_3 -doped Y_2O_3 vs wavelength.

Figure 2. Infrared absorption spectrum of as-processed La_2O_3 -doped Y_2O_3 .

Figure 3. Infrared absorption spectrum of an La_2O_3 -doped Y_2O_3 sample (2-mm thick) annealed at 1400°C for 3 hr in Ar - 5 ppm O_2 .

Figure 4. Infrared absorption spectrum of an La_2O_3 -doped Y_2O_3 sample (2-mm thick) treated in wet (D_2O) deuterium at 1400°C for 3 hr.

Figure 5. Infrared absorption spectrum of as-processed vs diffusion-annealed (1400°C for 20 min in Ar - 1 ppm O_2) La_2O_3 -doped Y_2O_3 sample (2-mm thick).

Figure 6. Diffusivity of hydrogen defects in La_2O_3 -doped Y_2O_3 vs reciprocal temperature.

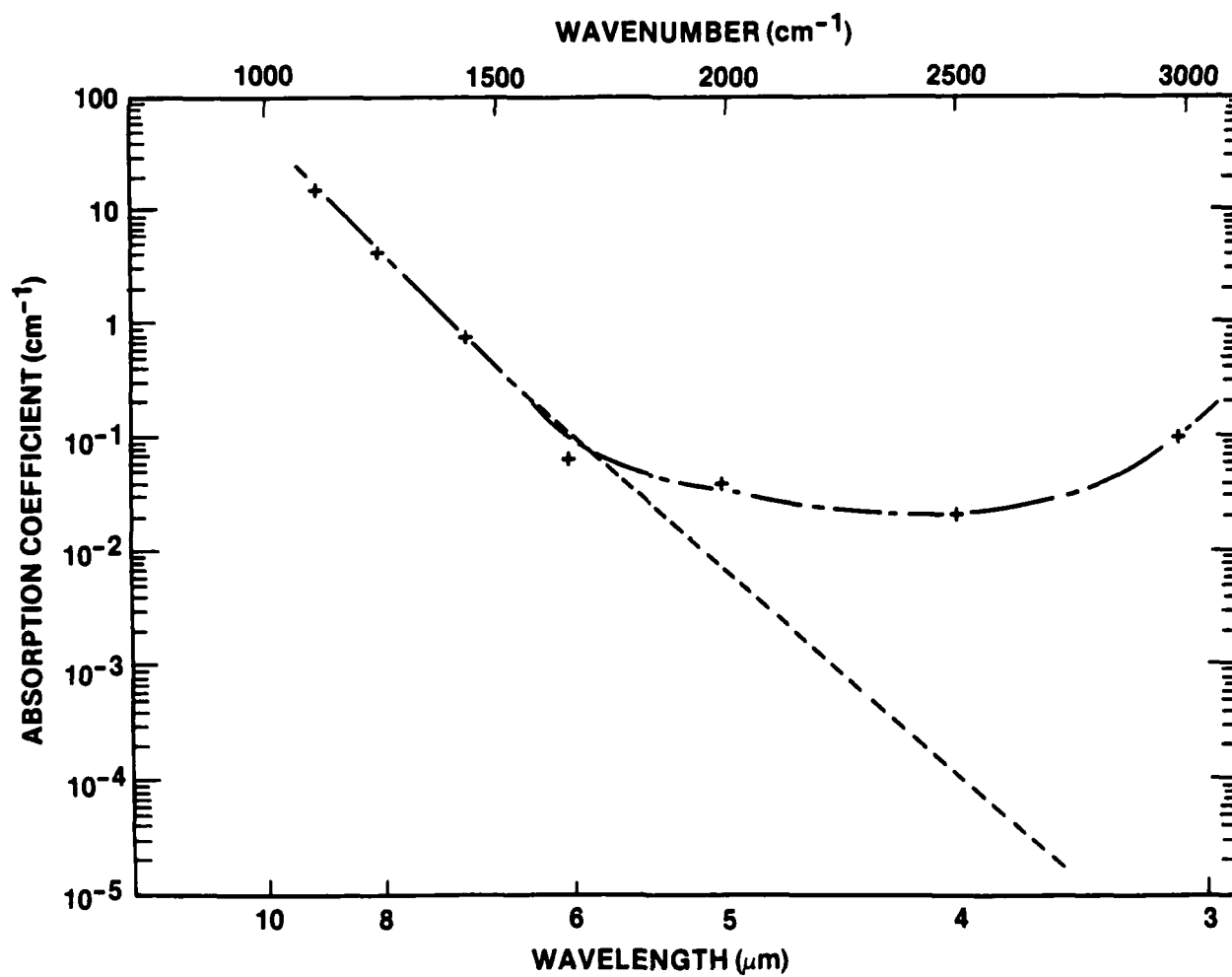


Figure 1. Absorption coefficient of as-processes La₂O₃-doped Y₂O₃ vs wavelength.

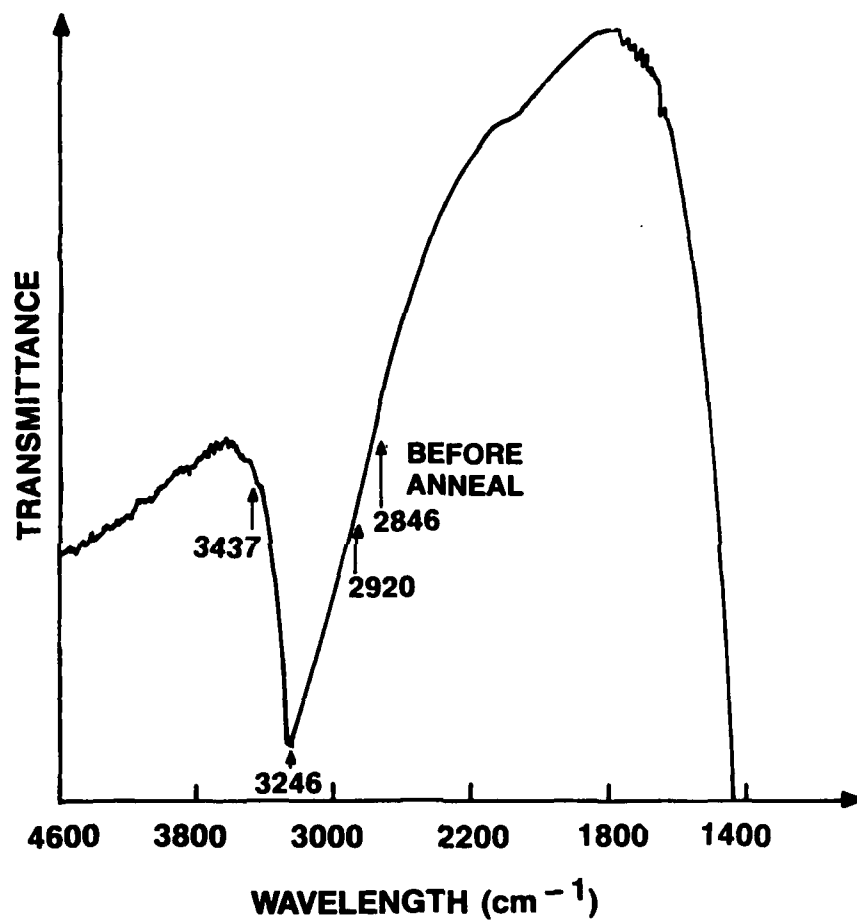


Figure 2. Infrared absorption spectrum of as-processed La_2O_3 -doped Y_2O_3 .

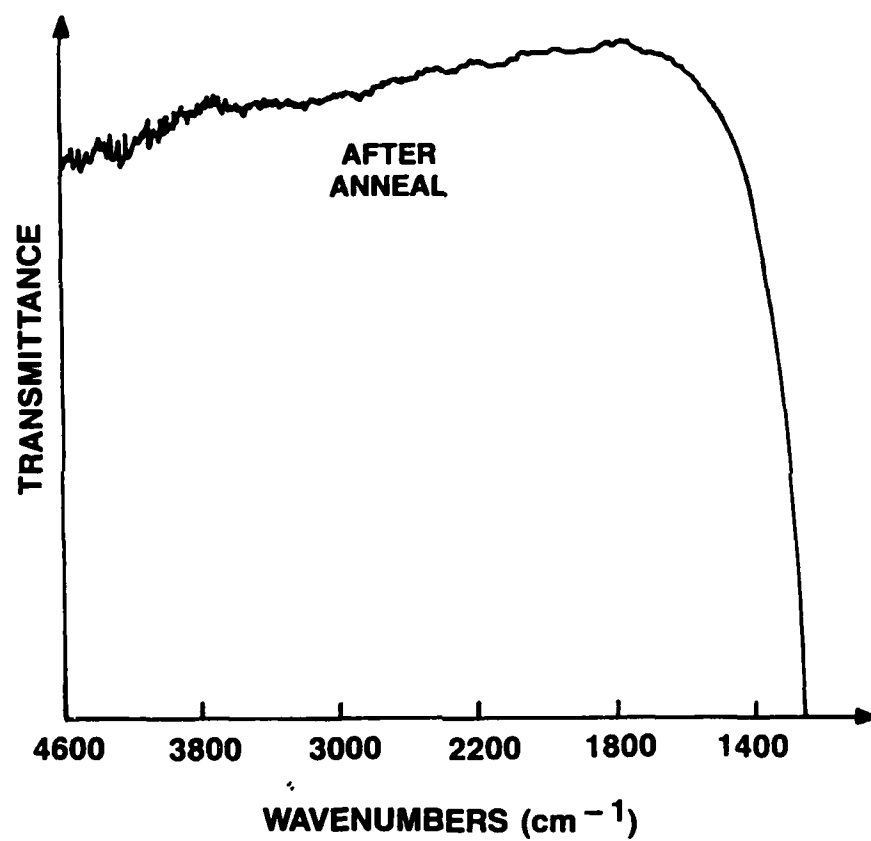


Figure 3. Infrared absorption spectrum of an La_2O_3 -doped Y_2O_3 sample (2-mm thick) annealed at 1400°C for 3 hr in Ar - 5 ppm O_2 .

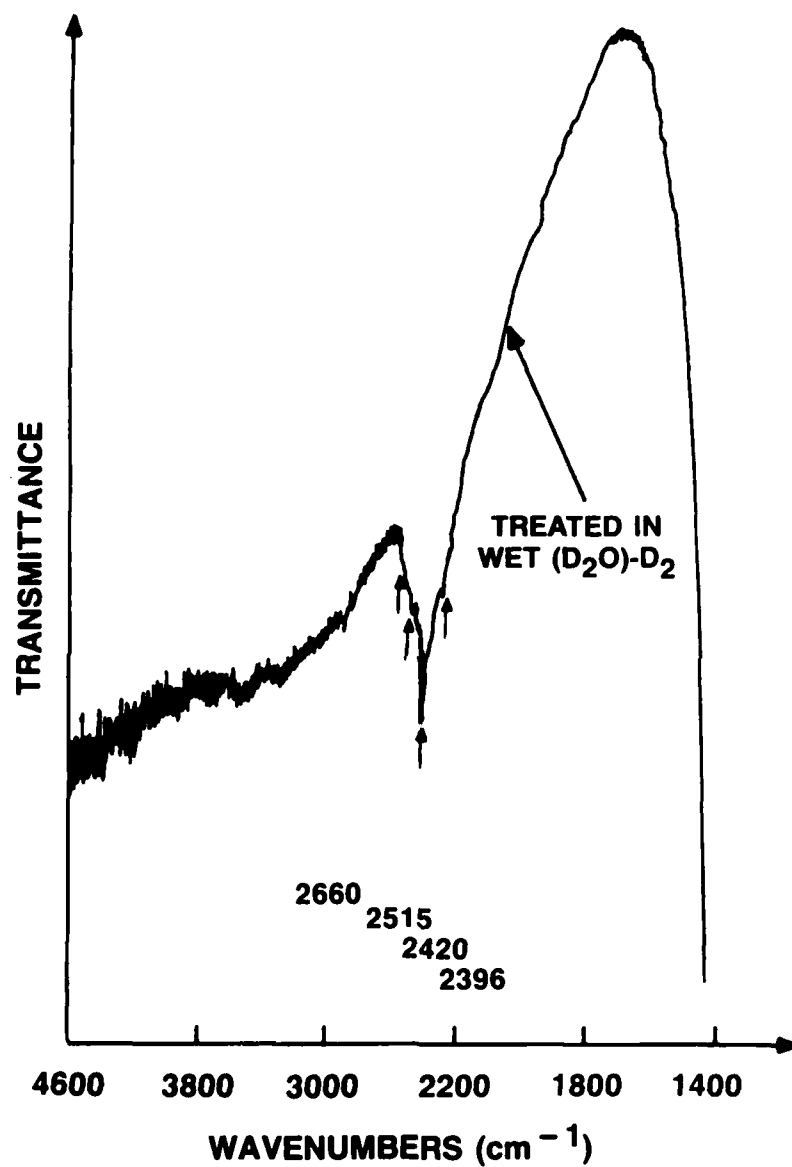
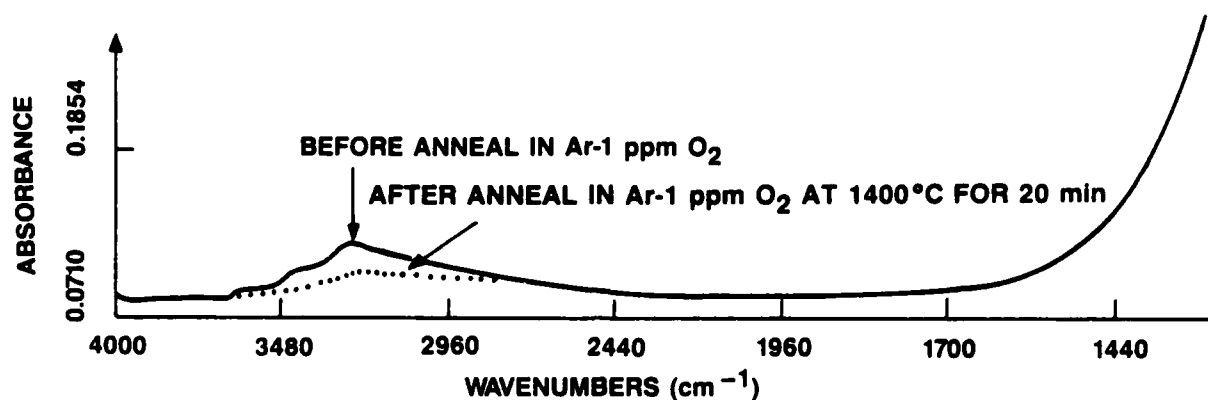


Figure 4. Infrared absorption spectrum of an La_2O_3 -doped Y_2O_3 sample (2-mm thick) treated in wet (D_2O) deuterium at 1400°C for 3 hr.



Diffusivity of Hydrogen Defect is Determined by

- $\frac{A_t - A_0}{A_\infty - A_0} = \frac{2}{L} \cdot \frac{1}{\sqrt{\pi}} \cdot \sqrt{Dt}$
- A = absorbance at 3246 cm^{-1}
(OH^- absorption peak)

Figure 5. Infrared absorption spectrum of as-processed vs diffusion-annealed (1400°C for 20 min in Ar - 1 ppm O_2) La_2O_3 -doped Y_2O_3 sample (2-mm thick).

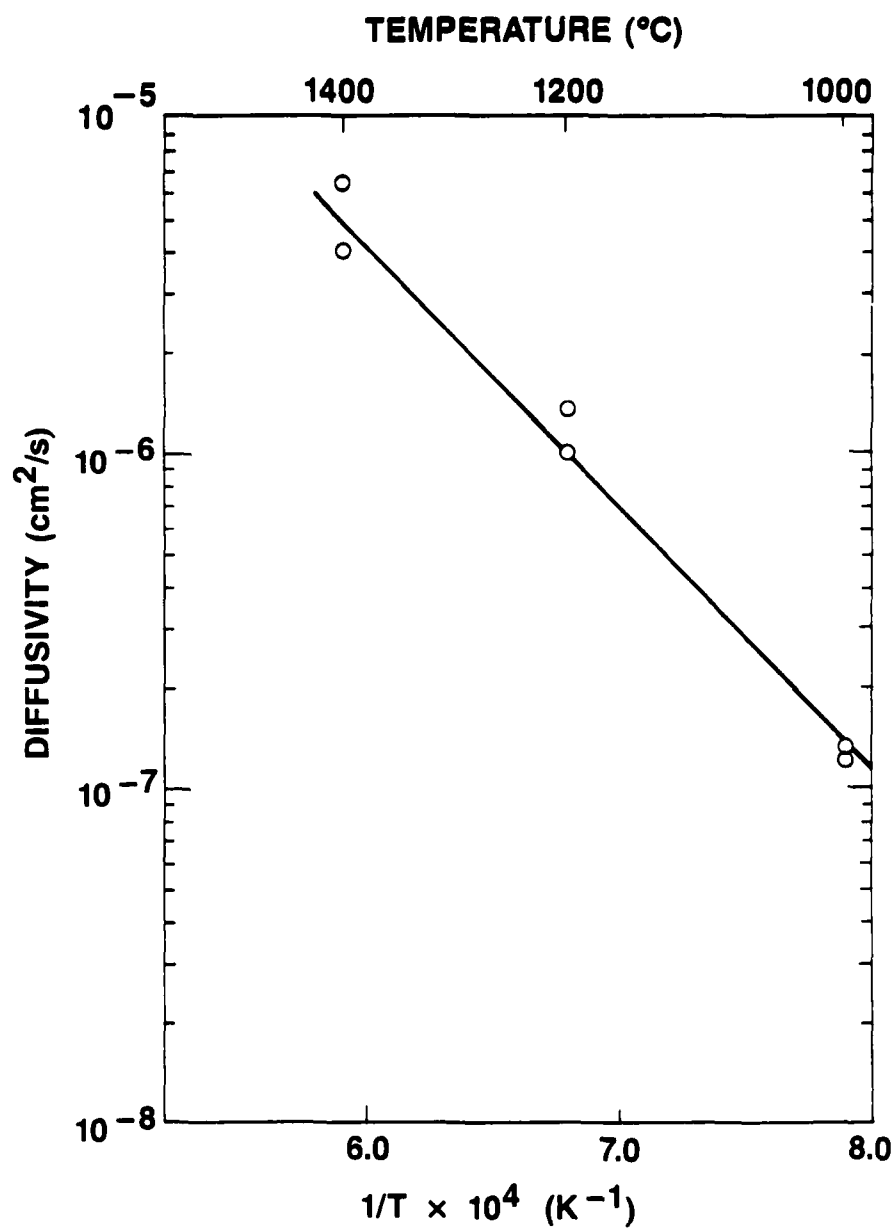


Figure 6. Diffusivity of hydrogen defects in La_2O_3 -doped Y_2O_3 vs reciprocal temperature.

**ADSORBED GASES AS A SOURCE OF RESIDUAL POROSITY
IN SINTERED TRANSPARENT YTTRIA**

by

D. Sordélet
W.H. Rhodes
E.A. Trickett

Adsorbed Gases As a Source of Residual Porosity in Sintered Transparent Yttria

by

D. Sordélet,* W.H. Rhodes, and E.A. Trickett

ABSTRACT

Gas evolution from La_2O_3 -doped Y_2O_3 samples was characterized. Results show that gases remain after calcining powders to 1000°C and presintering green compacts to 1500°C . Carbon dioxide is the major gaseous species present. This suggests that heating cycles should take into account gas evolution prior to pore closure in the final stage of sintering.

INTRODUCTION

The $\text{La}_2\text{O}_3\text{:Y}_2\text{O}_3$ system can be sintered to optical transparency through a controlled, transient, second-phase sintering technique.¹ One of the barriers to achieving theoretical transmittance throughout the total wavelength region of transmittance into the infrared, however, is very fine residual porosity. One possible explanation for the retained porosity is the desorption and entrapment of gases that are not completely removed during calcining or prefiring. Such gases could continue to evolve during the final stages of sintering and become entrapped. It is well known that some gases are insoluble in Al_2O_3 , for example, and can inhibit the attainment of full density.² In the case cited, the insoluble gases are those provided as the sintering atmosphere. It seems logical that certain adsorbed gases might also be insoluble and become entrapped due to their low lattice or grain boundary diffusivity if they desorb after closed porosity is reached in the sintering cycle. The origin of these gases could be incomplete calcination, hydration and conversion to a carbonate prior to pressing, and organic media pickup from milling or binders. The present communication deals with the gaseous evolution behavior of La_2O_3 -doped Y_2O_3 compacts during powder calcination and the initial stage of sintering.

EXPERIMENTAL PROCEDURE

The control powder (A) used in this investigation was prepared by a standard oxalate coprecipitation procedure. It was calcined at 600°C and has a corresponding BET surface area of $43.2 \text{ m}^2/\text{g}$ (see Table I). In order to compare the effect that ball milling and surface area have on gas evolution, one batch of the control powder was wet ball milled in organic media (B). Another batch (C) was calcined at 1000°C for 3 hr and then ball milled as above. Although ball milling has no significant influence on BET surface area, calcination at 1000°C reduces the BET surface area from $43.2 \text{ m}^2/\text{g}$ to $11.6 \text{ m}^2/\text{g}$ (see Table I).

* Present address: Iowa State University, Materials Science and Engineering Department, Ames, IA 50011.

Mass spectroscopy was used to characterize the three powders. Each of the three powders was tested as a green compact, and as a disc prefired to 1200°C for 2 hr. In addition one prefired disc was partially sintered to 70% density by heating to 1500°C. All specimens were stored in a drying oven at 200°C until analyzed. Analysis included the following steps: The furnace section of the spectrometer was heated to 1000°C and allowed to cool back to 400°C, where a blank of the system was taken. Next, either a section of a green compact or a prefired disc was entered into the spectrometer's furnace. The gases given off at 400°C were allowed to equilibrate, and the outgassing pressure was recorded. The gases were then run through the spectrometer. When the analysis at 400°C was completed, the gases were evacuated and the furnace temperature increased to 600°C. Gases were collected during the heatup and were allowed to stabilize at 600°C, at which time the outgassing pressure was recorded and the gases were analyzed in the spectrometer. This procedure was repeated at 800 and 1000°C.

The three powders were further analyzed by thermal gravimetric analysis using an air atmosphere and a heating rate of 10°C/min up to 1000°C.

RESULTS AND DISCUSSION

Figure 1 shows the outgassing pressures of the six samples. Prefiring effectively removes most of the total gas. Sample B has the highest gas level. This is expected because it was ball milled and has a high surface area. Sample C, although ball milled, produces the lowest amount of gas. This indicates that considerable gas volume is removed above 600°C during the calcination of sample C prior to ball milling.

The release of CO₂ from the three green compacts is displayed in Figure 2. Possible sources of CO₂ are the decomposition of any oxalate remaining after calcination and/or formation of carbonates during exposure to air. The similarity of Figures 1 and 2 illustrates that most of the total gas is CO₂, constituting between 70% and 98% of the gases produced.

The amounts of each gas present in the green control sample are displayed in Figure 3. Again, CO₂ is the major species. H₂O desorption peaks appear between 600°C and 800°C for each sample. These are somewhat higher temperatures than are normally expected for the loss of chemical water. This may be an indication of the complex gaseous thermodynamic and kinetic relationships not yet understood in the system. The green samples B and C produce similar results with respect to the relative quantities of each gas.

Methane was observed in the organic solvent wet milled powders, B and C, but not in the unmilled control A; therefore, organic milling aids appear to be the source for CH₄. A comparison of samples C and B in Figure 4 indicates that the higher surface area powder, B, attracts more organic during milling than does C. Figure 4 also shows that not all of the solvent medium is removed at 200°C and that some is retained at temperatures above those characteristic for the loss of physically adsorbed species. The maximum desorption of CH₄ around 600°C suggests that the organic is chemically bonding to the powders during ball milling. Since CH₄ still remains after the prefiring of samples B and C to 1200°C, it is believed that the presence of the other gases is the result of incomplete burnout during prefiring and not due to readsorption during cooling or storage. The gas evolution from a prefired sample C which was partially sintered by heating to

1500°C is shown in Figure 5. The gases are considerably reduced after this treatment, and CO₂ is once more the major component. The presence of water may be further evidence of the aforementioned thermodynamic complexities. One may argue that a partially sintered body presents sufficient open porosity for gas readsorption during transfer from storage oven to spectrometer. However the remaining CH₄ again indicates a strong argument that the gases are indeed a result of incomplete burnout even after pretreatment at 1500°C.

The total weight loss determined by mass spectrometry is compared to TGA results in Table II. The TGA weight loss from 25 to 200°C is added to the total weight loss calculated from the mass spectrometry results because the samples had been kept at 200°C prior to their mass spectrometry analysis. The good agreement of data obtained from the two methods reinforces the validity of the results from the individual analyses.

The control powder is very hygroscopic. A sample was recalcined to 600°C for 3 hr and then exposed to air for 144 hr under ambient laboratory conditions. The powder was then analyzed for H₂O and CO₂ content at 250 and 1200°C, respectively. During this exposure to air, the powder took on 3.22 wt. % H₂O and 2.17 wt. % CO₂. In a similar experiment, the powder was recalcined at 800°C for 3 hr and then exposed to air for 72 hr. The BET surface area was reduced from 43.2 to 24.5 m²/g and accordingly it attracted 2.56 wt. % H₂O and 1.53 wt. % CO₂. The theoretical dehydration and decomposition for Y(CO₃):H₂O doped with 10 mole % La(CO₃):8H₂O is 6.3 wt. % and 36 wt. %, respectively.³ These two experiments indicate that the powder has a stronger tendency to hydrate than to carbonate. Although the powder calcined at 800°C was exposed to air for only 72 hr, the results suggest that the lower surface area powder attracts less H₂O and CO₂.

CONCLUSIONS

It has been shown that not all the volatiles are removed from oxalate-derived powders during calcining or prefiring to 1500°C. CO₂ is the major species present and probably originates from nonoxidized oxalates and from carbonates which form during exposure to air. The powders used are very reactive, rapidly absorbing moisture and partially converting to the carbonate. The higher surface area powders attract more gases and media when milled in the latter. Chemical bonding may be occurring between the organic and powder during ball milling.

Instruments with higher temperature capabilities are needed to determine if and when all gases are evolved. This is an important phenomenon because gases that are entrapped can have a negative effect on the final sintered properties, i.e., transmittance and mechanical strength.

Sintering cycles may need to be adjusted to allow for desorption and permeation of insoluble gases from powder compacts when the highest degree of pore removal is sought. This should not be suprising when contrasted to the extensive firing required in producing optical glass.⁴

REFERENCES

1. W.H. Rhodes, "Controlled Transient Solid Second-Phase Sintering of Yttria," *J. Am. Ceram. Soc.* 64 [1] pp. 13-19 (1981).
2. R.L. Coble, "Sintering Alumina: Effect of Atmospheres," *J. Am. Ceram. Soc.* 45 [3] (March 1962).
3. W.W. Wendlandt and T.D. Green, *Tex. J. Sci.* 13, pp. 316-32 (1961).
4. M.C. Weinberg, P.I.K. Onorato, and D.R. Uhlmann, "Behavior of Bubbles in Glass Melts: II, Dissolution of a Stationary Bubble Containing a Diffusing and Nondiffusing Gas, *J. Am. Ceram. Soc.* 63 [7] (1980).

ACKNOWLEDGMENT

This study was performed with the support of the Office of Naval Research under Contract N0014-82-C-0452. We thank the many contributors from GTE, especially R. Thibodeau, M. Ames, S. Hankin, R. Hammond, and C. Beck.

Figure 1. Gas pressure/g vs temperature.

Figure 2. CO_2 evolution from green disks.

Figure 3. CH_4 evolution from green disks.

Figure 4. Control-green individual gas content.

Figure 5. Gas evolution from prefired Sample C after partial sinter to 1500°C .

Table I
Description of Powders

Powder	Calcine History	Milling History	BET Surface Area
A	600°C	No	43.2 m ² /g
B	600°C	Yes	43.2 m ² /g
C	1000°C	Yes	11.6 m ² /g

Table II
Percent Weight Loss

Powder	TGA 25-200°C	Mass Spectrometry 200-1000°C	Total*	TGA 25-1000°C
A	1.2	3.61	4.81	5.39
B	1.4	5.10	6.50	6.54
C	0.25	1.60	1.85	2.27

* TGA weight loss of 25-200°C added to compensate for 200°C storage prior to mass spectrometry analysis.

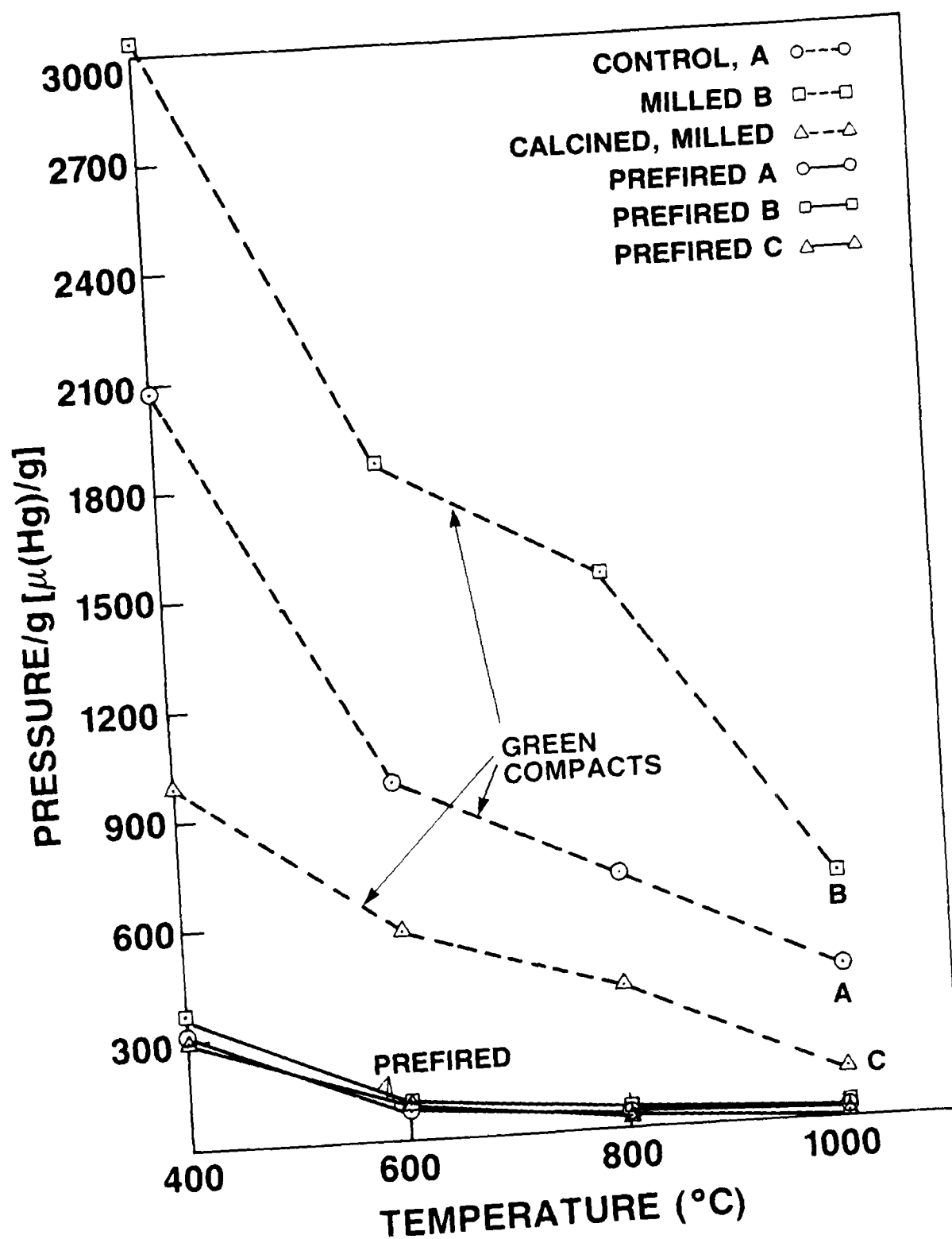


Figure 1. Gas pressure/g vs temperature.

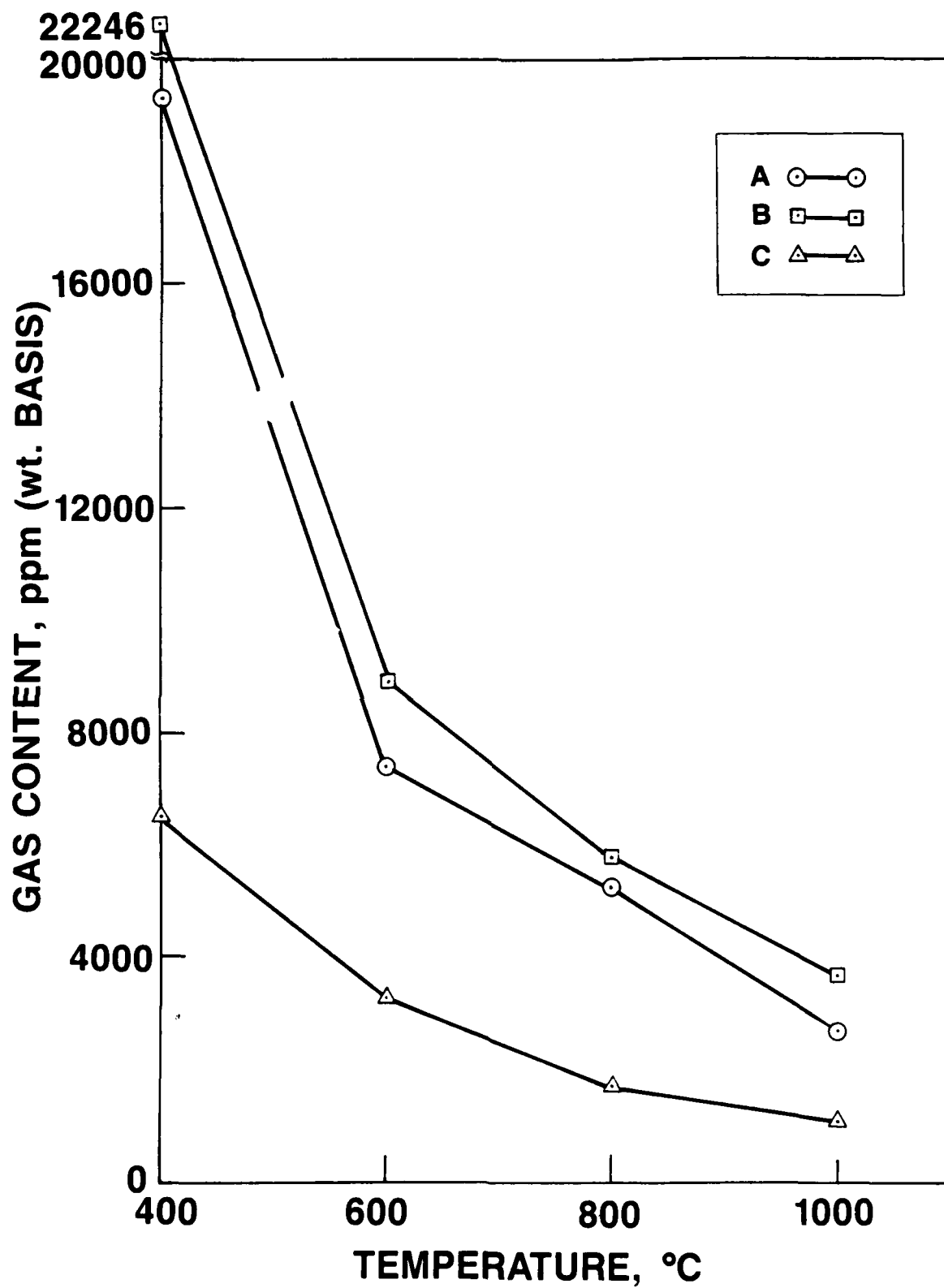


Figure 2. CO₂ evolution from green disks.

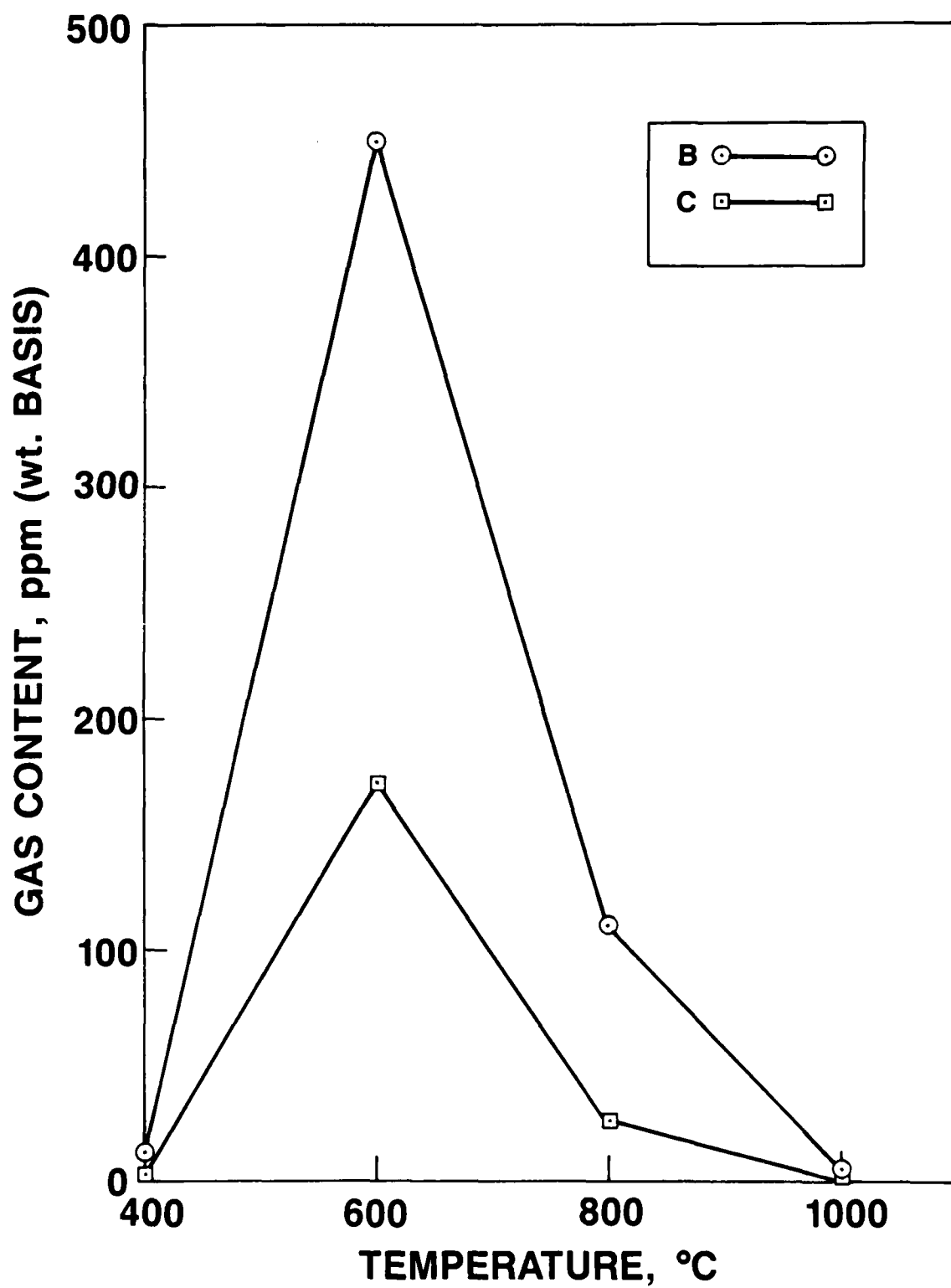


Figure 3. CH_4 evolution from green disks.

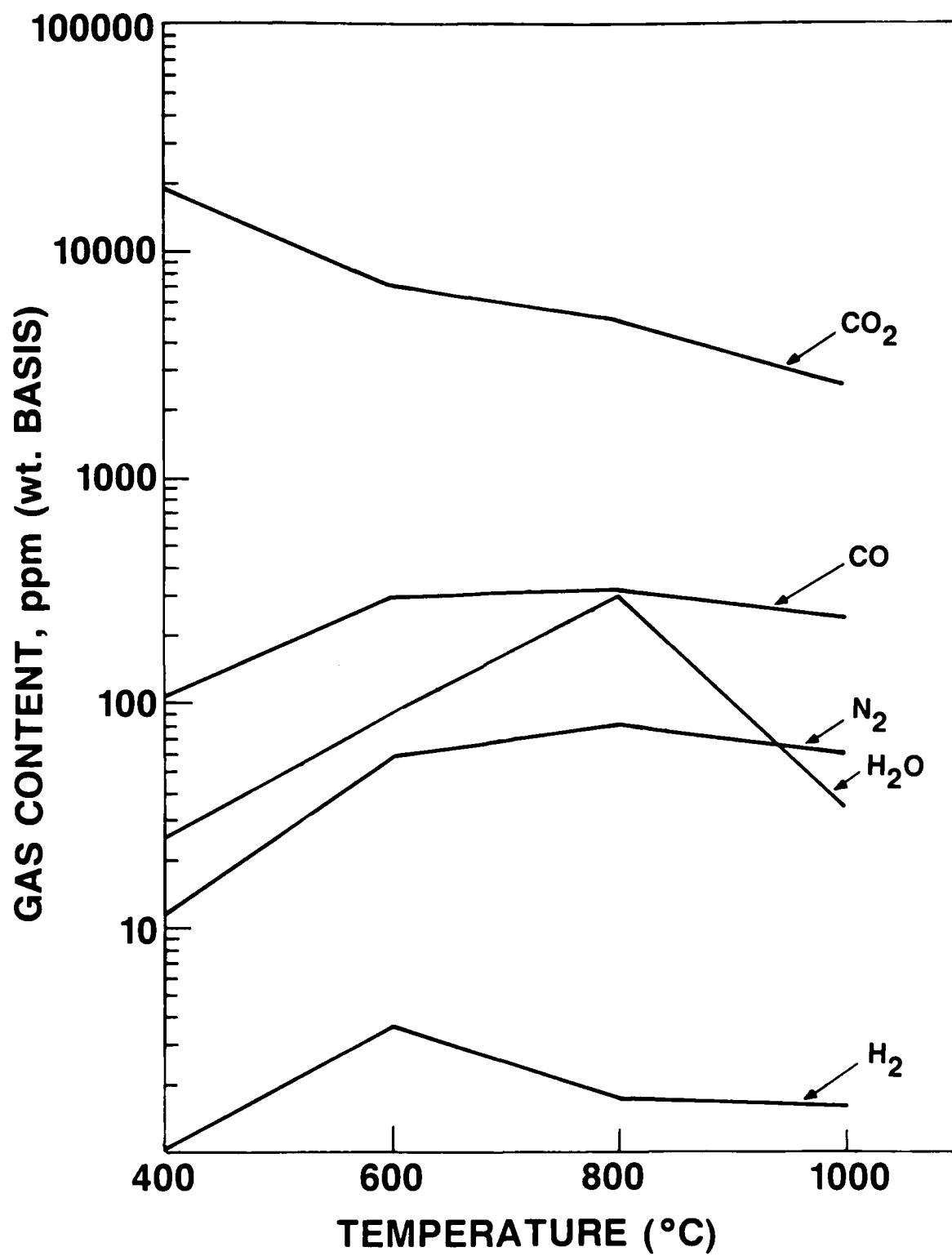


Figure 4. Control-green individual gas content.

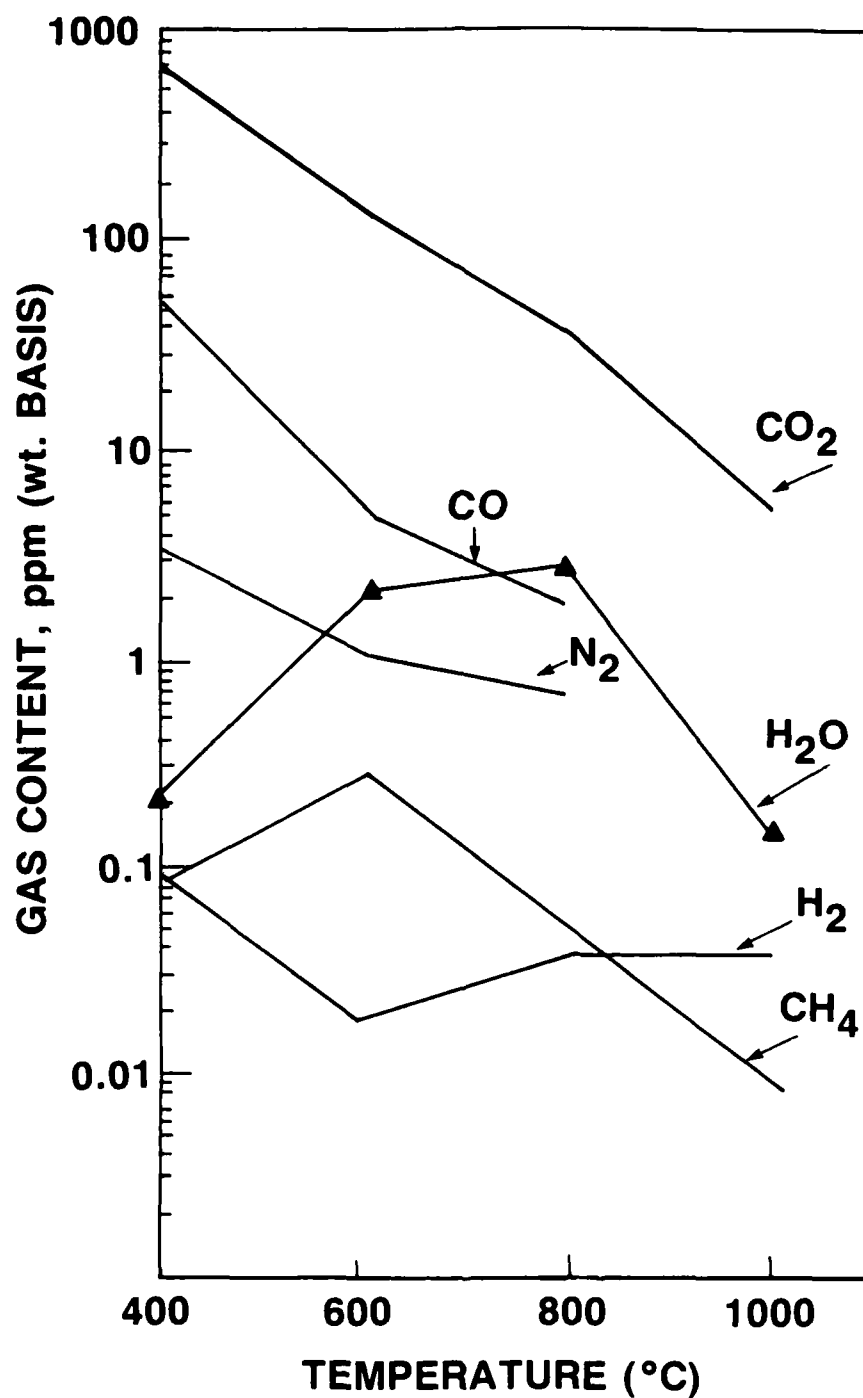


Figure 5. Gas evolution from prefired Sample C after partial sinter to 1500°C.

POLYCRYSTALLINE OXIDES FOR OPTICAL APPLICATIONS

by

W.H. Rhodes

CERAMICS: TODAY AND TOMORROW

Edited by

Shigeharu Naka

Nagoya University

Naohiro Soga

Kyoto University

Shoichi Kume

Osaka University

**The Basic Science Division
The Ceramic Society of Japan**

CONTENTS

Recent Trends in Design, Processing and Application of High Performance Ceramics	1
R. N. Katz	
Gas-Solid Interactions and Microstructure Development in Ceramics	33
D. W. Readey	
Wet Chemical Synthesis of Glasses and Ceramics :Opportunities and Critical Needs	51
D. R. Uhlmann	
Fundamentals of Powder Consolidation in Colloidal Systems	71
I. A. Aksay	
Sintering Additives and the Fabrication of High Density Ceramics	87
R. J. Brook	
Automotive Gas Turbine Ceramic Component Development	101
P. Heitman	
Consistency — A Critical Problem for Ceramics — Can Hot Isostatic Pressing Give an Answer?	119
H. T. Larker	
Role of Microstructure in the Improvement of the Fracture Behavior of Glass-Ceramics	129
D. P. H. Hasselman	
Polycrystalline Oxides for Optical Applications	149
W. H. Rhodes	
Superconducting Ceramics Prepared by CVD	165
G. Wahl and F. Schmaderer	

POLYCRYSTALLINE OXIDES FOR

OPTICAL APPLICATIONS

By

William H. Rhodes

GTE Laboratories

Waltham, Massachusetts, U.S.A.

ABSTRACT .

Polycrystalline oxides have been sintered or pressure sintered to optical transparency for demanding applications where glass has inadequate properties. The four major densification mechanisms are reviewed as well as the variations of sintering and pressure sintering. Many oxides have been fabricated, but the candidates Al_2O_3 , AlON , MgAl_2O_4 , MgO , Y_2O_3 , and $\text{Y}_3\text{Al}_5\text{O}_{12}$ are highlighted. Property trends are given particularly for infrared cut-off and thermal shock resistance. Future needs and processing trends are discussed.

1. Introduction

Most ceramics fabricated for optical use are melted and formed into shapes by glass making techniques. They are used in the glassy form since the amorphous structure and lack of grain boundaries permit the passage of light over a wide spectrum with only refraction from the surface, minimal scattering from retained bubbles, and minimal absorption depending on purity. There are a growing number of optical applications that cannot be sat-

Presented at Basic Science Division of Japan Ceramic Society, "Ceramics: Today and Tomorrow" November 28, 1985, Kobe, Japan

isfied by the available glasses. Glass research is progressing to satisfy many of these needs. However, it is clear that a number of applications can best be satisfied by crystalline materials because of superior inherent chemical and physical properties.

Crystalline materials can also be fabricated by melt techniques but, in this case, one must seed and grow single crystals to result in materials useful for optical applications. This results in a host of useful materials which are cut and polished into optical components. These components tend to be small and expensive. In addition, a number of potential ceramic compounds cannot be grown into useful size single crystals.

The field of optical polycrystalline ceramics has developed to fulfill the applications not satisfied by glass or single crystal materials. In several cases, altogether new devices were developed based on the properties of the polystalline oxide. For example, the development by Coble⁽¹⁾ of directly sintered translucent Al_2O_3 tubes made possible the high pressure sodium lamp with an estimated annual world production of 10^8 units. Haertling and Land⁽²⁾ fabricated transparent lanthanum-modified lead zirconate titanate (PLZT) and made possible high speed, visual protection glasses and three dimensional television based on electro-optic switching. In the case of alumina, single crystals by the edge defined growth technique came along later, and could possibly have supplanted the polycrystalline material except that price and several properties favored the polycrystalline product. The PLZT material on the other hand depends on the rapid switching of small domains and would not have been possible in the single crystal form. Thus, we have examples of polycrystalline oxides made viable based on low cost near-net-shape fabrication processes and unique physical properties.

A large number of polycrystalline oxides have been fabricated into translucent or transparent samples based on the literature. A number of these have been fabricated in one or two studies and, apparently, have not been

the subject of further development or application. Oxides in this category include Gd_2O_3 ,⁽³⁾ Sc_2O_3 ,⁽⁴⁾ $\text{Li Al}_5\text{O}_8$,⁽⁵⁾ BeO ,⁽⁶⁾ CaO ,⁽⁷⁾ $3\text{Al}_2\text{O}_3\text{-2SiO}_2$,⁽⁸⁾ $3\text{Al}_2\text{O}_3\text{-2GeO}_2$,⁽⁹⁾ and ThO_2 .⁽¹⁰⁾ The dominant, useful optical polycrystalline ceramic is Al_2O_3 and this is chiefly because of its thermodynamic stability and good physical properties. The other well developed oxides include Y_2O_3 ,⁽¹¹⁻¹⁹⁾ $\text{Y}_3\text{Al}_5\text{O}_{12}$,⁽²⁰⁻²²⁾ MgO ,⁽²³⁻³¹⁾ MgAl_2O_4 ,⁽³²⁻³⁹⁾ and AlON .⁽³⁹⁻⁴⁰⁾ It is interesting to note that this list is really based on three compounds, i.e., Al_2O_3 , MgO , and Y_2O_3 . This paper will review and compare the six dominate oxides, and discuss the important processing techniques for achieving optical transparency. Finally, an attempt will be made to predict the course of future developments in this field. The optically active materials such as PLZT will not be reviewed specifically, but much of the discussion concerning processing also applies to this class of material.

II. Fabrication Methods

All of the major process routes are based on the consolidation of powders below their melting point by sintering or pressure sintering. The driving force is the lowering of free energy by the elimination of the solid-vapor interfaces associated with the 25 to 60% porosity of the starting powder compact. Each major consolidation category has subsets; such as uniaxial hot-pressing, hot isostatic pressing, and press forging as variants of pressure sintering. Table 1 lists these processes along with their major advantages and disadvantages. Sintering is usually favored over pressure sintering because high volume production is possible. However, the sintering process is less tolerant of variations in powder properties and temperature than pressure sintering. Densification inhomogenities due to agglomerates and powder bridging can often be eliminated by particle rearrangement during the initial stages of pressure sintering. Unlike sintering, pressure sintering is usually a unit operation resulting in a few pieces of product per day, resulting in high cost. Some products such as infrared windows can tolerate the high costs.

Al_2O_3 was the first oxide sintered to translucency by Coble in about 1957.⁽¹⁾ The discovery that MgO acted as a solid state sintering aid for Al_2O_3 was largely responsible for a revolution in sintering research. The exact mechanism by which MgO affects the competing processes of pore elimination and pore entrapment through grain growth has been the subject of numerous papers and lively discussion in ensuing years. Bennison and Harmer⁽⁴²⁾ have shown that MgO decreased grain boundary mobility by a factor of 50. They speculated that even though MgO cannot be found at the grain boundaries, it interacts with the CaO impurity normally found in Al_2O_3 , on special and general grain boundaries, respectively, to retard grain growth. Alternatively, the Mg substitution may create defects in the Al_2O_3 lattice depressing the transport rate of the controlling diffusion species in grain growth. MgO lowers the density where impurity drag becomes effective and promotes a finer grain size at a given level of density. Pore-boundary attachment is favored which results in pore elimination before the onset of exaggerated grain growth. Other examples of solid state sintering to theoretical density are for ThO_2 doped Y_2O_3 ,⁽¹¹⁾ and SiO_2 and MgO doped $\text{Y}_3\text{Al}_5\text{O}_{12}$.⁽²⁰⁾

La_2O_3 -doped Y_2O_3 is a well documented example of transient solid-state sintering to transparency.⁽¹⁸⁻¹⁹⁾ The phase diagram for this system is unique in that a high temperature two-phase field exists above a single phase solid solution field. At the proper level of La_2O_3 doping, a sample is taken into the two-phase field where ≈ 25 v/o second phase markedly retards grain growth. This is thought to occur due to the fact that the long diffusion paths associated with Oswald ripening slow grain growth. Again pore boundary attachment is favored allowing the necessary time for pore removal by solid state diffusion. Once pores are removed, the temperature is lowered into the single phase zone and the sample converts to a pore free microstructure. Prochazka and Klug⁽⁸⁾ indicated that Al_2O_3 rich mullite formed precipitates that could be removed by subsequent annealing. This may be another example of transient solid-state sintering.

Al₂O₃ was the first oxide sintered to translucency by Coble in about 1957.⁽¹⁾ The discovery that MgO acted as a solid state sintering aid for Al₂O₃ was largely responsible for a revolution in sintering research. The exact mechanism by which MgO affects the competing processes of pore elimination and pore entrapment ~~through grain growth~~ has been the subject of numerous papers and lively discussion in ensuing years. Bennison and Harmer⁽⁴²⁾ have shown that MgO decreased grain boundary mobility by a factor of 50. They speculated that even though MgO cannot be found at the grain boundaries, it interacts with the CaO impurity normally found in Al₂O₃, on special and general grain boundaries, respectively, to retard grain growth. Alternatively, the Mg substitution may create defects in the Al₂O₃ lattice depressing the transport rate of the controlling diffusion species in grain growth. MgO lowers the density where impurity drag becomes effective and promotes a finer grain size at a given level of density. Pore-boundary attachment is favored which results in pore elimination before the onset of exaggerated grain growth. Other examples of solid state sintering to theoretical density are for ThO₂ doped Y₂O₃,⁽¹¹⁾ and SiO₂ and MgO doped Y₃Al₅O₁₂.⁽²⁰⁾

La₂O₃-doped Y₂O₃ is a well documented example of transient solid-state sintering to transparency.⁽¹⁸⁻¹⁹⁾ The phase diagram for this system is unique in that a high temperature two-phase field exists above a single phase solid solution field. At the proper level of La₂O₃ doping, a sample is taken into the two-phase field where ≈25 v/o second phase markedly retards grain growth. This is thought to occur due to the fact that the long diffusion paths associated with Oswald ripening slow grain growth. Again pore boundary attachment is favored allowing the necessary time for pore removal by solid state diffusion. Once pores are removed, the temperature is lowered into the single phase zone and the sample converts to a pore free microstructure. Prochazka and Klug⁽⁸⁾ indicated that Al₂O₃ rich mullite formed precipitates that could be removed by subsequent annealing. This may be another example of transient solid-state sintering.

Liquid phase sintering is the most universally applied approach to sintering translucent ceramics. The small concentration of liquid phase remaining at the grain boundaries refracts light leading to a translucent product rather than a transparent material where the in-line or specular transmittance is equivalent to the total transmittance. Judging by the wide number of oxides sintered to translucency by liquid phase sintering, it would appear that successful sintering systems could be found for most oxides. Examples include Y_2O_3 ,^(16, 17) $MgAl_2O_4$,⁽³⁵⁻³⁶⁾ Al_2O_3 ,^(42a) $3Al_2O_3 \cdot 2SiO_2$.⁽⁸⁾ Essentially one needs to experiment near the solid end of a solid plus liquid phase field. Only a few volume percent of a wetting liquid phase are required to provide a high diffusivity path at the grain boundaries. The driving force for densification remains the same reduction in free energy operative in solid state sintering. The major difference is the increased transport rates due to the presence of the liquid phase. Exaggerated grain growth usually occurs, so it is more difficult to keep the pores on the grain boundaries long enough for their complete elimination. Large grain sizes are typical for liquid phase sintered materials due to the high transport rates operative.

Transient liquid phase sintering is a variation of liquid phase sintering where the second phase is removed during processing. One method for second phase removal is to operate in a liquid plus solid field for sintering and, subsequently, anneal back to a single phase body. This approach is completely analogous to the transient solid-state sintering previously described. This mechanism may operate for SiO_2 rich compositions in sintering $3Al_2O_3 \cdot 2SiO_2$,⁽⁸⁾ but it is not widely employed due to the difficulty in finding an appropriate system. A more common variation of this mechanism is to employ a volatile halide as the liquid phase additive. After the additive has performed its function to enhance transport rates, it diffuses down grain boundaries to the surface and, subsequently, is volatilized from the surface. Ideally, no second phase remains, but SEM and stress corrosion behavior indicated that 0.1% LiF remained in MgO after a 60 h post hot-pressing anneal at 1000°C.⁽⁴³⁾ The starting composition was 0.3% LiF. In addition to

MgO,⁽²³⁻³¹⁾ the oxides MgAl_2O_4 ,^(33, 34) Gd_2O_3 ,⁽³⁾ and CaO ,⁽⁷⁾ have been sintered or hot-pressed employing volatile halide sintering aids.

Pressure sintering is often employed since the added driving force enhances the densification process. The reduction in free energy associated with surfaces remains the main driving force, but the application of pressure can act in several beneficial ways. Initially, the powder can be rearranged to a more favorable packing geometry through partial sliding. This sliding action also breaks down agglomerates which might otherwise lead to pore nests in the final microstructure. At elevated temperatures, Nabarro-Herring type diffusional creep assists the transport process. Finally, in certain systems, and under forging conditions, it may be possible to initiate plastic deformation. In most cases, sintering aids are required which implies that one of the sintering mechanisms already discussed is essential. Thus, the application of pressure is really an assist to sintering requiring lower process temperatures and resulting in smaller final grain sizes. The major problem encountered is chemical interaction with the die body and inability to control the gaseous environment. Separating barriers such as boron nitride or tungsten sheet are often employed. Many oxides pressed in graphite dies end up grey and are subjected to a subsequent anneal to improve the body color. Peelen^(44, 45) employed continuous uniaxial hot-pressing to fabricate transparent undoped Al_2O_3 with high transparency due to the $1\mu\text{m}$ grain size and, more importantly, the very fine ($0.1\mu\text{m}$ - $0.2\mu\text{m}$) pore size. This work is one of the most complete studies on the factors affecting transparency.

Hot isostatic pressing (HIP) has been employed for BeO and PZT.⁽⁴⁶⁾ In this work, cold pressed discs were encapsulated in evacuated borosilicate glass tubes and HIPPED at 1000 - 1400°C and 195MPa . It is possible to HIP without a pressure transmitting container by first sintering to closed porosity ($\approx 93\%$ dense). This approach eliminates possible interaction with the container and makes it possible to choose the composition of the gas trapped in the remaining porosity. This composition may be critical as Coble⁽⁴⁷⁾ and

others⁽⁴⁸⁾ have shown the importance of having a soluble or rapid diffusing gas species on sintering to theoretical density. HIP processes have been utilized to achieve high transparency in ZnS,⁽⁴⁹⁾ and CaLa₂S₄.⁽⁵⁰⁾ Extensive use of containerless HIP technology in fabricating transparent polycrystalline oxides has not been demonstrated.

The advantage of press forging over uniaxial hot pressing was first demonstrated on Y₂O₃.⁽⁵¹⁾ Translucent Y₂O₃ was achieved compared to a 99% dense opaque ceramic body by hot-pressing. Press forging is accomplished by compressing a dense or partially sintered compact in a flat or shaped die such that no lateral constraints are present. The specimen is forged at moderate pressures (40 MPa), and strain rates (10⁻⁴) sec.⁻¹ such that the mechanisms operative in uniaxial hot pressing contribute to densification in addition to high temperature deformation. It is possible that several deformation mechanisms operate. Preferred crystallographic orientation in both Y₂O₃⁽⁵¹⁾ and Al₂O₃⁽⁵²⁾ demonstrated that slip along preferred planes occurred. This is believed to have aided densification and reduced birefringence in the case of Al₂O₃. The texture was confirmed by x-ray techniques. Absorption coefficients as low as 0.015 cm⁻¹ at 4.5μm. were achieved for Al₂O₃. It was possible to fabricate a translucent 7.5 cm diameter hemisphere by forging a 98.5% dense 5 cm diameter by 3.5 cm high solid right cylinder at 1900°C. Graphite dies were employed, so it was necessary to prevent a reaction with a boron nitride diffusion barrier. Tearing occurred at the outer circumference, but it was possible to machine away the cracked region.

III. Properties

A compilation of intrinsic and extrinsic properties for the six polycrystalline oxides is shown in Table 2. Many of the properties are strongly temperature dependent, so the data must be used with caution. For example, the thermal conductivity for the oxide appears quite distinct and different at 300°K, but a comparison at 800°K would indicate a much closer spread. A

second factor to consider is that data such as bend strength and fracture toughness are microstructure dependent. Different manufacturers will produce material with different properties. This can make a large difference in performance in demanding applications. The values reported are from several reviews on optical materials^(53, 54) and the specific articles on individual oxides.^(20, 22, 31, 34, 39, 55)

Several properties are interrelated based on the structure and bonding. The ionic vibrational modes govern the long wave cut-off. Large amplitude vibrations will occur when there is a coincidence between the frequency of the incoming radiation and the resonant frequency of the ions. A simple harmonic oscillator model has been effective in predicting the fundamental absorption frequency, ν of many polar diatomic structures,⁽⁵³⁾ and is given by:

$$\nu = (1/2\pi) (f/\mu)^{1/2} \quad (1)$$

where the reduced mass $\mu = m_1 m_2 / (m_1 + m_2)$ and f is the force constant related to the elastic modulus and lattice parameter. By simple inspection, it can be seen that the bonding which results in high elastic modulus, high melting point, and low expansion coefficient give rise to higher frequency (shorter wavelength) infrared cut-offs. A comparison of the six candidate oxides cut-off with hardness shows the clear trend between these properties (FIG.1). Similar plots of thermal expansion melting point, or Young's modulus do not show direct correlations. The varying atomic masses and lattice parameter must be accounted for in the oscillator model to make the direct correlation.

A long infrared cut-off window makes possible application in a device requiring transmission at 3-5 μ m. If such a device is to be heated, the phonon edge will move to shorter wavelengths again favoring the longer wavelength transmitting oxides, Y_2O_3 and MgO. Long wavelength transmittance oxides

have lower emissivity. This is illustrated in Figure 2 where the theoretical single crystal transmittance curves for Al_2O_3 and Y_2O_3 are shown together with the black body radiosity curve for 1500°K . The principal contribution to Y_2O_3 's emittance is the overlap of the radiosity curve and the absorption curve (crosshatched area). The overlap is significantly less for Y_2O_3 than for Al_2O_3 (slashed area under the curve). This effect has been demonstrated in a study^(14, 56) of Y_2O_3 envelope high pressure sodium lamps where an emittance of 0.12 at 1500°K was measured for Y_2O_3 compared with 0.19 for Al_2O_3 . This lowered the radiation loss in the Y_2O_3 lamps and resulted in a higher wall temperature keeping the power level and tube geometry equivalent to the Al_2O_3 envelope lamps.

Thermal shock resistance is important for most applications. As noted in the compendium by Hasselman,⁽⁵⁷⁾ each thermal stress environment has a different set of controlling physical properties. In extremely severe conditions, the parameter is:

$$R_1 = \frac{\sigma (1-u)}{\alpha E} \quad (2)$$

where σ is the strength u is Poisson's Ratio, α is the thermal expansion coefficient, and E is the elastic modulus. A less severe environment where there is time for the thermal gradient to disperse by conduction, the controlling equation becomes

$$R_2 = R_1 k \quad (3)$$

where k is the thermal conductivity. These parameters have been calculated employing the data in Table 2 and neglecting u since Poisson's Ratio is nearly equal for the candidate oxides. These data are reported in Table 3 where the oxides are listed in order of relative thermal shock resistance. $\text{Y}_3\text{Al}_5\text{O}_{12}$ appears to be excellent under R_1 conditions and second under R_2 environ-

ment. The main reason for this is that the σ/E ratio is larger than the other oxides due to excellent process and microstructure control.⁽²²⁾ Al_2O_3 has a high thermal conductivity which explains its' good predicted behavior under R_2 conditions. These same calculations would show quite different rating if high temperature properties were employed. Thus, calculations and ratings such as shown in Table 3 should be used with caution. The thermal environment should be specified and a model should be generated which accurately reflects the temperature and stress state where thermal stress failure is expected. Tests that simulate this environment can be employed on prototype parts or test bars, but these too are complex and can lead to erroneous conclusions.

The other properties of interest depend on the application. For example, hardness is not important for lamp envelopes, but it becomes a factor for erosion resistance. High speed missiles need resistance to rain and dust erosion which can occur while the missile is being carried under the wing of an airplane. The fracture toughness is also important in determining the erosion threshold and rate.

Chemical properties became important in the lamp envelope application. Reactions with the fill components and atmosphere can dictate whether or not a particular envelope will survive and assuming the reaction rates are slow, how long the envelope will last. The Al_2O_3 envelope high pressure sodium lamp can last in excess of 20,000 h even though it reacts with sodium to form beta alumina at an intermediate temperature near the electrodes.⁽⁵⁸⁾ The Y_2O_3 envelope high pressure sodium lamp must be kept to $<1250^\circ\text{C}$ to prevent a reaction with the atmosphere causing darkening due to nonstoichiometry.⁽¹⁵⁾ Other materials such as MgAl_2O_4 have undergone limited testing for the high pressure sodium lamp application.⁽³⁷⁾

IV. Future Trends

Of the six polycrystalline oxides highlighted in this paper, Al_2O_3 is the only one which has reached a manufacturing status. It is highly likely that development will continue on one or more of the other oxides. There is considerable U.S. interest in advanced infrared materials. There is also interest World-wide on advanced lamp envelope materials. It is not clear whether or not the economics could justify a material such as $\text{Y}_3\text{Al}_5\text{O}_{12}$ or Y_2O_3 for high pressure sodium lamp envelopes. Increased lamp efficacies have been demonstrated, but Y_2O_3 powder costs 4 times the current price for Al_2O_3 powder, so there are trade-offs. Lighting scientists continue their search for better color and more efficient lamp chemistries. Chemical reactions dictate the choice of container materials, so it is quite likely that new envelopes will be required. The increased free energy of formation for Y_2O_3 or $\text{Y}_3\text{Al}_5\text{O}_{12}$ over Al_2O_3 may make these or some other candidate material stable and, therefore, useful.

Processing may change from the methods outlined. For example, Debsikdar⁽⁶⁰⁾ has prepared sol-gel monoliths of MgAl_2O_4 . This method and other colloidal synthesis routes may make possible lower temperature processing. Sintering aids may become obsolete due to the close packing of the particles which makes possible complete densification with little grain growth and, hence, no pore entrapment. Chemical routes to powder synthesis also allow close control over composition which is often critical for compounds with narrow solubility limits.

References

1. R. L. Coble, "Transparent Alumina and Method of Preparation," U.S. Patent 3,026,210.
2. G. H. Haertling and C. E. Land, "Hot-Pressed (PL,La) (Pb,Ti) O₃ Ferroelectric Ceramics for Electro-optic Applications," J. Am. Ceram. Soc. 54, 1, (1971).
3. Edward Carnall and Donald Pearlman, "Transparent Gd₂O₃ Ceramics and Phosphors," Mat. Res. Bull. 7, 647 (1972).
4. G. E. Gazza, D. Roderick, B. Levine, "Transparent Sc₂O₃ by Hot Pressing," J. of Matl, Sci. 6 (1971).
5. G. E. Gazza "Hot Pressing of Li Al₅O₈," J. Amer. Ceram Soc. 55, 172, (1972).
6. John Rickter, "Translucent Beryllium Oxide as Envelope Material for High Intensity Arc Lamps," Office of Naval Research Contract No. N00014-71-C-0384.
7. T. K. Gupta, B. R. Rossing, and W. D. Straub, "Fabrication of Transparent Polycrystalline CaO," J. Amer. Ceram. Soc. 56, 339 (1973).
8. S. Prochazka and F. J. Klug, "Infrared-Transparent Mullite Ceramic," J. Amer. Ceram. Soc. 66, 874 (1983).
9. S. Prochazka and G. A. Slack, "Preparation and Optical Properties of Polycrystalline Aluminum Germanate," Mat. Res. Soc. Proceedings 32,

p.245, C. J. Brinker, D. E. Clark, D. R. Ulrich Eds., North-Holland, N.Y., (1984).

10. P. J. Jorgensen and W. G. Schmidt, "Final Stage Sintering of ThO_2 ," J. Am. Ceram. Soc. 53, 24 (1970).
11. P. J. Jorgensen and R. C. Anderson, "Grain-Boundary Segregation and Final Stage Sintering of Y_2O_3 ," J. Am. Ceram. Soc. 50, 553 (1967).
12. C. Greskovich and K. N. Woods, "Fabrication of Transparent ThO_2 -doped Y_2O_3 ," Amer. Ceram. Soc. Bull. 52 473 (1973).
13. G. Toda, I. Matsuyama, and Y. Tsukuda, "Method for Producing Highly Pure Sintered Polycrystalline Yttrium Oxide Body Having High Transparency," U. S. Patent 3,873,657 (March 1975).
14. J. Waymouth and E. Wyner, "Analysis of Factors Affecting Efficacy of High Pressure Sodium Lamps, J. of I.E.S. 10, p.237 (1981).
15. Y. Tsukuda, "Change of Y_2O_3 Sintered Body in Na Vapor," Yogyo-Kyokai-Shi 85 (2), 149 (1977).
16. W. H. Rhodes and F. J. Reid, "Transparent Yttria Ceramics and Method for Producing Same," U. S. Patent 4,098,612 (July 1978).
17. W. H. Rhodes, "Transparent Yttria Ceramics Containing Magnesia or Magnesium Aluminate," U. S. Patent 4,174,973 (November 1979).
18. W. H. Rhodes, "Transparent Yttria Ceramics and Method for Producing Same," U. S. Patent 4,115,134 (September 1978).

19. W. H. Rhodes, "Controlled Transient Solid Second-Phase Sintering of Yttria," J. Am. Ceram. Soc. 64, 13 (1981).
20. G. DeWith and J. E. D. Parren, "Translucent $Y_3Al_5O_{12}$ Ceramics," Mat. Res. Bull. 19, 1669 (1984).
21. C. A. M. Mulder and G. DeWith, "Translucent $Y_3Al_5O_{12}$ Ceramics: Electron Microscopy Characterization," to be published in Solid State Ionics.
22. G. DeWith and J. E. D. Parren, "Translucent $Y_3Al_5O_{12}$ Ceramics: Mechanical Properties," to be published in Solid State Ionics.
23. Leon M. Atlas, "Effect of Some Lithium Compound on Sintering of MgO," J. Am. Ceram. Soc. 40 196 (1957).
24. Roy W. Rice, "Hot Pressing of MgO with NaF," J. Am. Ceram. Soc. 54, 205 (1971).
25. E. Carnall and S. E. Match, "Magnesium Oxide Infrared Transmitting Optical Elements," U. S. Patent 3,326,595.
26. E. Carnall, "The Densification of MgO in the Presence of a Liquid Phase," Mat. Res. Bull. 2, 1075 (1967).
27. W. H. Rhodes, D. J. Sellers and T. Vasilos, "Development and Evaluation of Transparent Magnesium Oxide," Final Report AMRA-CR-67-01(F), on Contract DA-19-066-AMC-291(x), February 1967.
28. G. D. Miles, R. A. J. Sambell, J. Rutherford, and G. W. Stephenson, "Fabrication of Fully Dense Transparent Polycrystalline Magnesia," Trans. Brit. Ceram. Soc. 77, 319 (1967).

29. M. W. Benecke, N. E. Olson, and J. A. Pask, "Effect of LiF on Hot Pressing of MgO," J. Amer. Ceram. Soc., 50, 365 (1967).
30. P. E. Hart, R. B. Atkin, and J. A. Pask, "Densification Mechanisms in Hot-Pressing of Magnesia with A Fugitive Liquid," J. Am. Ceram. Soc. 53, 83 (1970).
31. J. E. Niese, "Technical Aspects of Transparent Ceramic Armor Fabrication," SAMPE Quarterly 1, (4) 17 (1970).
32. A. Gatti and M. J. Noone, "Feasibility Study for Producing Transparent Spinel," Final Report Contract DAAG46-69-C-0096.
33. W. H. Rhodes, P. L. Berneburg, and J. E. Niese, "Development of Transparent Spinel," Final Report Contract DAAG-46-69-C-0113, AD876908.
34. D. W. Roy, "Hot-Pressed MgAl_2O_4 for Ultraviolet, Visible, and Infrared Optical Requirements," SPIE 297 13 (1981).
35. R. J. Bratton, "Translucent Sintered MgAl_2O_4 ," J. Am. Ceram. Soc. 57, 283 (1974).
36. R. J. Bratton, "Magnesium Aluminate Spinel Member Having Calcium Oxide Addition," U. S. Patent 3,567,472.
37. P. Hing, "Fabrication of Translucent Magnesium Aluminate Spinel and its Compatibility in Sodium Vapor," J. Matl Sci. 11, 1919 (1976).
38. Isao Oda, Masayuki Kaneno, Issei Hayakawa, "Polycrystalline Transparent Spinel Sintered Body and a Method for Producing the Same," U. S. Patent 4,273,587.

39. T. M. Hartnett and R. L. Gentilman, "Optical and Mechanical Properties of Highly Transparent Spinel and AION Domes," Proc. 28th Ann. Symp. SPIE 505, S. Musikant Ed p.15 (1984).
40. T. M. Hartnett, E. A. Maguire, R. L. Gentilman, N. D. Corbin and J. W. McCauley, "Aluminum Oxynitride Spinel (ALON) - A New Optical and Multimode Window Material," Ceramic Engineering and Science Proceedings 3, 67 (1982).
41. J. W. McCauley and N. D. Corbin, "Phase Relations and Reaction Sintering of Transparent Cubic Aluminum Oxynitride Spinel (AION), J. Am. Ceram. Soc. 62, 476 (1979).
42. a) Stephen J. Bennison and Martin P. Harmer, "Effect of MgO Solute on the Kinetics of Grain Growth in Al_2O_3 ," J. Am. Ceram. Soc. 66, C90, (1983).

b) Stephen J. Bennison and Martin P. Harmer, "Grain-Growth Kinetics for Alumina in the Absence of a Liquid Phase," J. Am. Ceram. Soc. 68, C22, (1985).
43. W. H. Rhodes, R. M. Cannon, Jr., and T. Visolos, "Stress-Corrosion Cracking in Polycrystalline MgO" in Fracture Mechanics of Ceramics, Vol. 2 edited by R. C. Bradt, D. P. H. Hasselman, and F. F. Lange, Plenum Publishing Corp., New York, P.709.
44. J. G. I. Peelen, "Transparent Hot-Pressed Alumina" Ceramurgia International 5, 70 (1979).
45. J. G. I. Peelen and R. Melselaar, "Light Scattering by Pores in Polycrystalline Materials: Transmission Properties of Alumina", J. App. Phy. 45, 216 (1974).

46. M. Koizumi, K. Kodaira, Y. Ishitobi, M. Shimada, and F. Kanamaru, "Fabrication of Translucent Ceramics by Isostatic Hot-Pressing" *Ceramurgia International* 2, 67 (1976).
47. R. L. Coble, "Sintering Alumina: Effect of Atmospheres" *J. Am. Ceram. Soc.* 45 123 (1962).
48. M. O. Warman and D. W. Budworth, "Effects of Residual Gas on the Sintering of Alumina to Theoretical Density in Vacuum," *Trans. Brit Ceram. Soc.* 66, 265 (1967).
49. C. B. Willingham and J. Papas, "New High-Transparency Infrared Optical Materials" *Bull. Am. Ceram. Soc.* 63, 487, (1984).
50. K. J. Saunders, T. Y. Wong, T. L. Gentilman, "CaLa₂S₄ Long Wavelength IR material of the Future" *Bull. Am. Ceram. Soc* 63, 487 (1984).
51. L. A. Brissette, P. L. Burnett, R. M. Spriggs and T. Vasilos, "Thermomechanically Deformed Y₂O₃" *J. Am. Ceram. Soc.* 49, 165 (1966).
52. W. H. Rhodes, D. J. Sellers, and T. Vasilos "Hot-Working of Aluminum Oxide: II, Optical Properties," *J. Am. Ceram. Soc.* 58, 31 (1975).
53. I. W. Donald and P. W. McMillan, "Review-Infra-red Transmitting Materials," *J. Matl Sci.* 13, 1151 (1978).
54. R. M. Cannon, T. D. Ketchum, T. W. Coyle, "Toughened Optical Materials," *SPIE* 297, 173 (1981).

55. W. H. Rhodes, "Transparent Polycrystalline Yttria for IR Applications," Proceedings of the Sixteenth Symposium on Electromagnetic Windows, Atlanta, GA 1982, p.103.
56. W. H. Rhodes, "Sintered Y_2O_3 for Lamp Envelopes," 2nd International Symposium on Incoherent Light Sources, Enschede, Netherlands 1979, p.103.
57. D. P. H. Hasselman, "Thermal Stress Resistance Parameters for Brittle Refractory Ceramics: A Compendium," Bull. Am. Ceram. Soc. 49, 1033 (1970).
58. P. Hing, "Interaction of Alkali Metal and Halide Vapors with Ceramic Material," J. of IES July 1981, p.194.
59. J. C. Debsikdar, "Preparation of Transparent Noncrystalline Stoichiometric Magnesium Aluminate Gel-Monolith by the Sol-Gel Process," to be published in J. Matl. Sci.

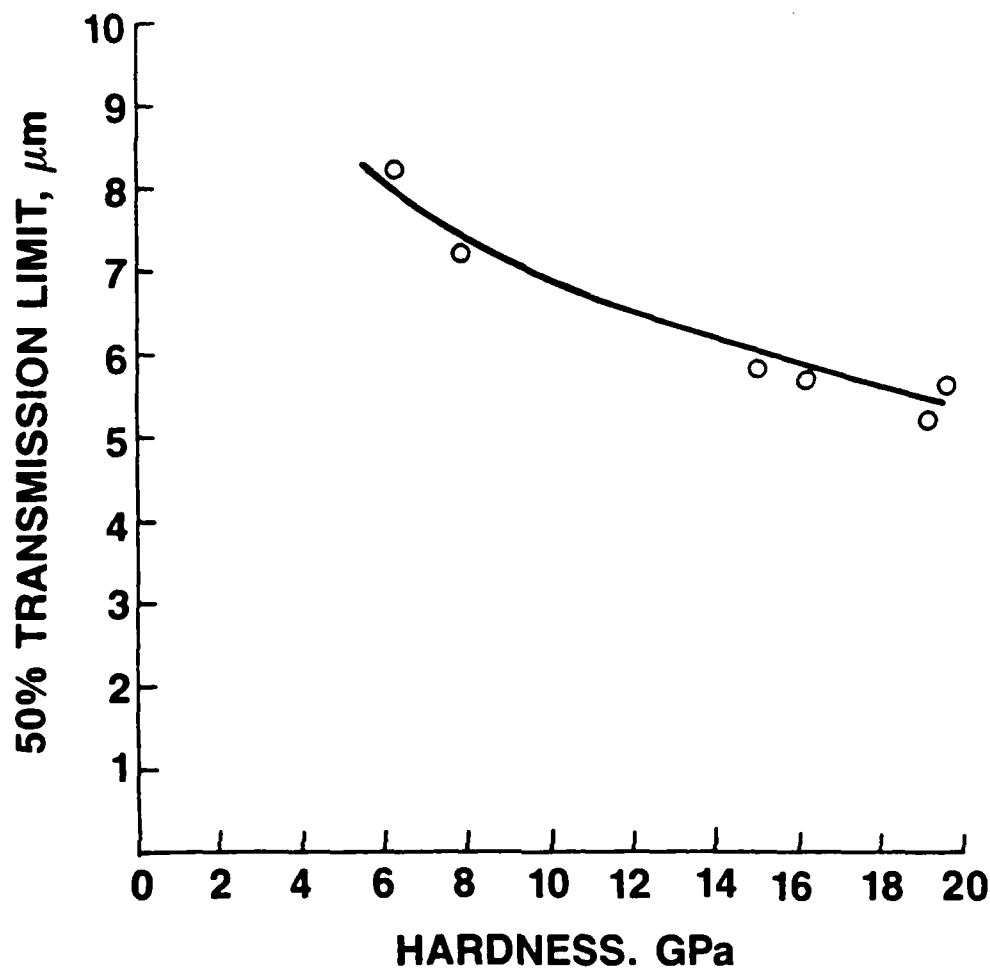


FIGURE 1 - Dependence of Hardness on Infrared Cut-off

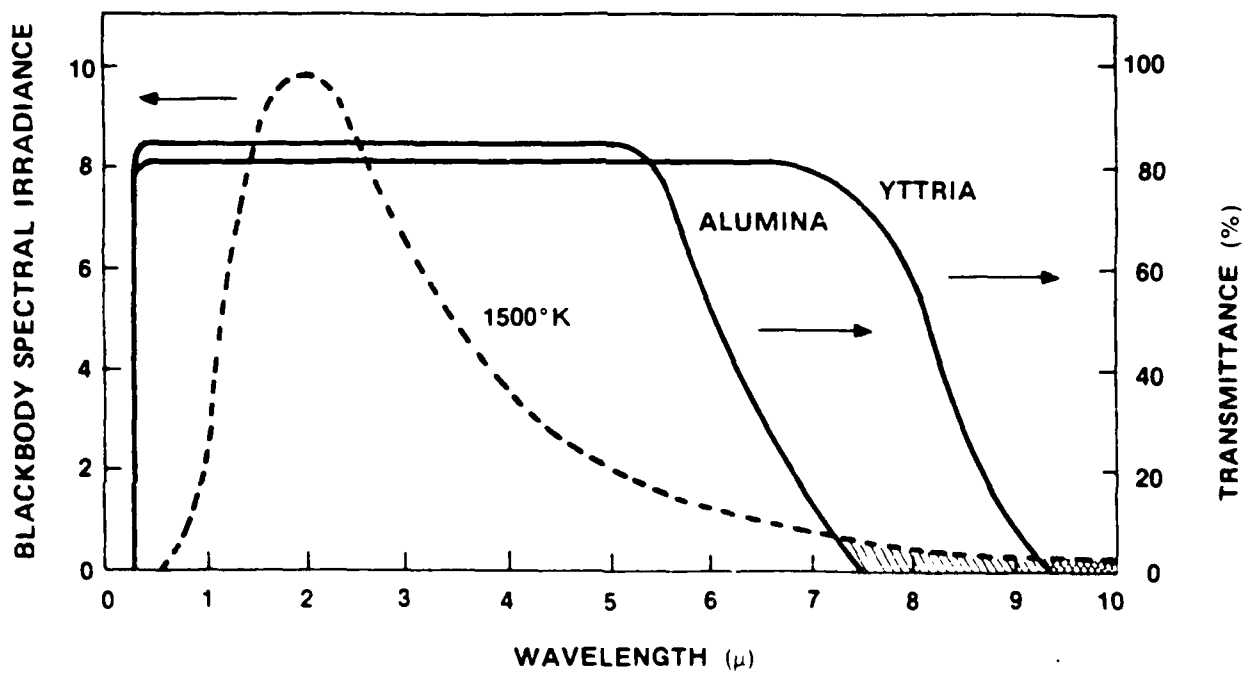


FIGURE 2 - Theoretical Transmittance Curves for Alumina and Yttria Showing Effect of Thermal Radiation on Emittance

Table 1
Major Consolidation Processes for
Polycrystalline Oxides

Consolidation Techniques	Advantages	Disadvantages
1. Sintering		
a. Solid state	Single phase, model microstructure	Difficult to identify sintering aid
b. Transient solid state	Single phase, grain size control	Few suitable systems
c. Liquid phase	Many systems possible, rapid densification	Light diffraction from second phase, large grain size
d. Transient liquid phase	Rapid densification, near single phase	Few suitable systems, difficult to eliminate second phase
2. Pressure Sintering		
a. Uniaxial	Pressure enhances densification, small	Interaction with die components grain size
b. Hot isostatic pressing	Added driving force for final stage	Requires sintering to closed porosity
c. Press forging	Addition of plastic deformation, crystallographic texturing	Cavitation and tearing possible

Table 2
Properties of Polycrystalline Oxides

Property	Al ₂ O ₃	AlON	MgAl ₂ O ₄	MgO	Y ₂ O ₃	Y ₂ Al ₅ O ₁₂
Crystal Structure	Hexagonal	Cubic	Cubic	Cubic	Cubic	Cubic
Density, gm/cc	3.99	3.71	3.59	3.58	5.13	4.56
Melting Point, °C	2050	2140	2135	2800	2464	1970
Thermal Expansion Coefficient 25 - 1000°C, × 10 ⁶ °C ⁻¹	8.2	7.8	9	13.5	7.9	8.6
Thermal Conductivity, W m ⁻¹ °K ⁻¹ @ 300°K	29	12.6	14.6	25	13	13
Young's Elastic Modulus, GPa	405	323	277	307	164	290
Hardness, GPa	19.6	19.1	16.1	6.3	7.2	15
Bend Strength, MPa	310	296	184	206	150	410
Fracture Toughness, MN m ^{-3/2}	3 - 5	2	1.2 - 2.4	2.4	1 - 2	1.7
Refractive Index (Visible)	1.77	1.793	1.715	1.74	1.93	1.84
Transmission Limit, μm > 50% for 2.5 mm	5.56	5.12	5.69	8.2	7.9	5.78

Table 3
Ranking for
Thermal Shock Resistance

Compound	R_1	R_2
$Y_2Al_5O_{12}$	164	2137
Al_2O_3	93.3	2706
Y_2O_3	116	1508
AlON	117	1474
$MgAl_2O_4$	73.8	1077
MgO	49.7	1242

**PREPARATION AND CHARACTERIZATION OF
YTTRIA MONOSIZE POWDERS**

by

Mufit Akinc
Daniel Sordélet

PREPARATION AND CHARACTERIZATION OF
YTTRIA MONOSIZE POWDERS

ANNUAL REPORT
(Sept. 1, 1985 - June 30, 1986)

By

Mufit Akinc and Daniel Sordelet

To

GTE LABORATORIES, INC.

P.O. # 51-J3685

July 1986

ABSTRACT

Synthesis and characterization of monosize yttria powders from aqueous solutions were investigated. Emphasis was given to determination of the range of experimental conditions which would result in formation of spherical monosize powders. The role of urea in the process was determined to be the slow, homogeneous generation of carbon dioxide which causes precipitation of yttrium hydroxycarbonate. Preliminary work on sintering of monosize yttria compacts indicated that theoretical densities may be achieved at temperatures as low as 1500°C. By increasing the volume of the precipitation solution by four-fold (to 3200 ml) and optimizing the experimental conditions, the yield of the process was increased by an order of magnitude over earlier 800 ml batches. Experimental evidence is extremely promising that the process can be scaled-up to industrial production levels and will be commercially feasible.

TABLE OF CONTENTS

	Page
1. INTRODUCTION	1
2. EXPERIMENTAL	2
2.1 Powder Synthesis	2
2.1.1 Materials	2
2.1.2 Precipitation	2
2.1.3 Characterization	5
2.1.4 Packing and Sintering	5
3. RESULTS AND DISCUSSION	7
3.1 Micromorphology and Yield	7
3.2 Effect of Anions on the Micromorphology	15
3.3 Chemical Composition of the Precipitate	17
3.4 Mechanism of the Precipitation Reaction	20
3.5 Thermal Decomposition of the Precursor	22
3.6 Packing and Sintering Studies	25
4. COOPERATIVE EFFORTS WITH GTE	28
5. CONCLUSIONS	29
6. REFERENCES	31

ACKNOWLEDGMENTS

The authors acknowledge the support of Dr. W. H. Rhodes, senior staff scientist from GTE Labs, Inc. Appreciation is also extended to Ms. Elizabeth Trickett for her assistance in obtaining impurity analyses of the synthesized powders. Particular thanks are due to Dr. D. T. Peterson for making Ames Laboratory facilities available for chemical analysis of precursor powders, and to Mr. R. Bachman for carrying out the analyses. Mr. Mike Munson and Miss Kristen Persels have assisted in powder preparation and characterization; their contribution is greatly appreciated. The authors especially thank Ms. Barb Dubberke for typing this report. Finally, contributions of Professor M. F. Berard through seminal discussions and reviewing this report are greatly appreciated.

1. INTRODUCTION

A considerable amount of research effort has been given to the synthesis and characterization of submicron, monosize particles of uniform shape (1,2). The promise of these powders, with their well controlled morphology, is that they should lead to uniform green compacts which, in turn, should produce uniform and theoretically dense sintered microstructures. A limited number of experiments have verified these predictions (3).

Yttria is a potential candidate as a high temperature infrared transparent material. Rhodes (4,5) showed that La_2O_3 -doped Y_2O_3 powder compacts can be sintered to produce IR transparent material with improved mechanical properties. One of the most critical stages of the whole process was the preparation and treatment of the starting powders. Recently, monosize, spherical Y_2O_3 and La_2O_3 -doped Y_2O_3 powders were synthesized in our laboratory (6). This was achieved by homogeneous precipitation of particles through slow decomposition of urea in boiling aqueous solutions.

The goals of this study were to understand the effect of various experimental conditions on powder characteristics, and to better understand the physicochemical process which produces these uniform particles.

Results of work carried out on pure yttria will be discussed in this report, but they can be extended to lanthana-doped yttria.

2. EXPERIMENTAL

2.1 POWDER SYNTHESIS

2.1.1 Materials

Yttrium source material for this study was oxide of 99.99% purity obtained from Molycorp, Inc. (Lots #1319 and 1556). A typical chemical impurity analysis of the starting oxide is given in Table 1. Other reagents, such as nitric acid, hydrochloric acid, acetic acid, trichloroacetic acid, urea and acetone, were all of reagent grade obtained from Fisher Scientific, and were used without further purification.

2.1.2 Precipitation

A yttrium stock solution was prepared as follows: 90.3 g of yttria was dissolved in a stoichiometric amount of nitric acid and diluted to 2 liters. The stock solution had a pH of 4.0 to 5.0 and a concentration of 0.4 M with respect to the yttrium ion. The benchmark precipitation process was accomplished by adding 50 ml of stock solution and 13.0 g urea to sufficient water to make a total volume of clear solution 800 ml. The solution was heated to boiling on a magnetically stirred hot plate. Aging by mild boiling was continued for one hour after the formation of first nuclei was noticed by the appearance of a 'bluish' tint in the clear solution. During the whole aging period, no more than 10% volume reduction in the solution was observed. At the end of the aging period, the suspension was filtered through a 0.2 μ m teflon membrane, and the precipitate was washed once with water and then with acetone. During the second half of the project, the filtration step was replaced by centrifugation to expedite the separation process, as well as to improve the recovery. The washed precipitate was dried overnight in air at 110°C for filtered powder and 80°C for centrifuged powder.

The amounts of yttrium stock solution and urea described above correspond to 0.025 and 0.27 M for yttrium and urea, respectively, in the 800 ml solution. To investigate the role of yttrium ion

Table 1. Impurity analyses of raw Y_2O_3 powders

(in ppm weight)

Element	Lot #1282*	Lot #1319 [†]	Lot #1556*
Al	--	0.3	--
Co	3.0	1.7	2.0
Ba	25.0	0.8	<25.0
Sr	<6.0	--	<6.0
Zn	1.1	--	<0.5
Cr	<10.0	0.2	<10.0
Ni	<10.0	--	<12.0
Mn	<6.0	--	<6.0
Fe	1.0	1.2	0.9
Pb	<20.0	--	<20.0
La	<500.0	--	<50.0
Ce	<10.0	--	<10.0
Pr	0.8	--	<0.5
Nd	18.0	--	1.2
LOI(%)	0.56	--	0.42

* Provided by Molycorp, Inc.

[†] From Ref. (5).

concentration on the process, it was varied from 0.005 to 0.100 M by adjusting the amount of stock solution and water such that the total volume of solution remained constant at 800 ml. Other variables were also kept constant at benchmark values. In another series of experiments, urea concentration was varied from 0.027 to 0.810 M, while other variables were kept constant at benchmark values. The influence of aging time on the powder characteristics was studied by varying the time from 10 minutes to six hours, while all other variables were kept at benchmark values.

The influence on the process of the supporting anion in the stock solution was studied by replacing nitrate ions with chloride or acetate ions. This was done by simply dissolving the raw oxide in hydrochloric or acetic acid to prepare the stock solution.

To elucidate the mechanism of precipitate formation, urea was replaced with trichloroacetic acid (CCl_3COOH) and with formamide. In the case of trichloroacetic acid, 30 g of acid is added to 50 ml of nitrate stock solution and 750 ml of H_2O . The solution pH was adjusted to 4.5 by additions of NH_4OH before heating. The solution was then heated with stirring, similar to the urea case, but the temperature was maintained at only 80°C where rather strong CO_2 evolution followed by a white precipitate formation was observed. In the case of formamide, about 200 ml of the reagent was added instead of urea, and the solution was boiled for about an hour; no precipitate was formed. Another 200 ml of formamide and an additional one hour of boiling did not produce any solid phase.

A limited number of experiments were carried out to see if there was an effect of stirring rate and heating rate by changing settings on the hot plate-magnetic stirrer.

One of the limitations in the benchmark precipitation method was that only small amounts of powder were obtained per batch: typically 1 to 1.2 g of oxide per 800 ml of starting solution. Based on the results of experiments described above, urea

concentration was raised to 0.52 M, and aging time was increased to 90 minutes to improve the yield per batch without losing the desired particle morphology. Furthermore, total batch volume was quadrupled to 3200 ml in order to produce more powder per batch.

2.1.3 Characterization

One of the most critical tests for a given processing route is its reproducibility, in particular, the micromorphology of the precursor particles synthesized. It is important to establish the effect of each variable on the micromorphology. Scanning electron microscopy was utilized to evaluate the size and shape of the particles synthesized. In addition, particle size distribution was determined on selected preparations using a Microtrac Small Particle Size Analyzer (SPA). Samples for these determinations were prepared by dispersing them in dilute pyrophosphate solutions with a sonic disruptor.

TGA/DTA analysis was carried out from room temperature to 1000°C in air with a heating rate of 20°C/min. X-ray diffraction patterns were obtained for precursor and oxide powders. Loss on ignition was determined after calcining precursors at 900°C in air for 4 hours. Chemical analysis of precursor powders was accomplished by conventional methods: yttrium by complexometric titration, total carbon by absorbing CO₂ during thermal decomposition and nitrate ions by ion selective electrodes. Results of these experiments were combined with loss on ignition and electrical neutrality to estimate the chemical composition of the precursor powder. Impurity analyses of the various precursors and oxide powders were made by spark source mass spectroscopy at GTE Labs, Inc.

2.1.4 Packing and Sintering

While not the main emphasis of this research, a limited number of experiments were carried to assess the sintering behavior of the

powders synthesized. In these preliminary studies, yttria powders were dispersed in 10% Darvan 7 aqueous solutions, the pH of the suspension was adjusted to a predetermined value and it was cast into compacts by centrifuging at about 3000 rpm. These compacts were dried thoroughly before sintering. Sintering experiments were carried out in a vacuum furnace with a tungsten mesh heater. Relatively low sintering temperatures were employed for these preliminary experiments, as more in-depth sintering experiments were to be carried out by GTE. Pellets were roasted at 500°C for 2 hours and at 1475°C in vacuum with a 3 hour soak. The heating and cooling rate was ~6°C/min. Sintered pellets were reoxidized in air at 1100°C. The microstructures of the sintered compacts were observed using SEM.

3. RESULTS AND DISCUSSION

3.1 Micromorphology and Yield

One of the paramount goals in the study of homogeneous precipitation was to assess the role of individual processing variables on the shape, average size and size distribution, and yield of powders. These variables are known to drastically alter particle micromorphology (7).

The effects of yttrium ion concentration on the yield and morphology are summarized in Table 2. Micrographs of Y7, Y9 and Y11 are shown in Figure 1. Apparently, as the yttrium concentration increased over 0.05 M, the spherical shape was distorted and particles tended to agglomerate. At the lowest yttrium ion concentration, the particles were spherical, but there was a noticeable variation in size. The yield of the process decreased as the yttrium ion concentration increased. Even though the initial urea concentration was higher than the stoichiometric requirement at all yttrium ion concentrations studied, apparently only a portion of the urea was utilized for precipitating the yttrium ions. This observation was substantiated by the experiments in which urea concentration was varied. Table 2 includes loss on ignition (%LOI) for the same series. Over the range studied, LOI remained constant at $36.5 \pm 1.5\%$. The constant LOI implies that the composition of the particles formed did not vary significantly for this series. Average particle size appeared to increase as yttrium ion concentration increased. This implies that the number of nuclei did not vary with yttrium concentration, but rather that as the cation concentration increased, the size of the fixed number of particles increased. However, the scope of experiment results does not warrant further discussion and/or quantification of these observations.

The influence of urea concentration on powder characteristics is presented in Table 3. Trends observed in this series support the data presented in the previous table. That is, as the $[\text{urea}]/[\text{Y}^{+3}]$ increased (going from Y13 to Y18), the yield of the process increased.

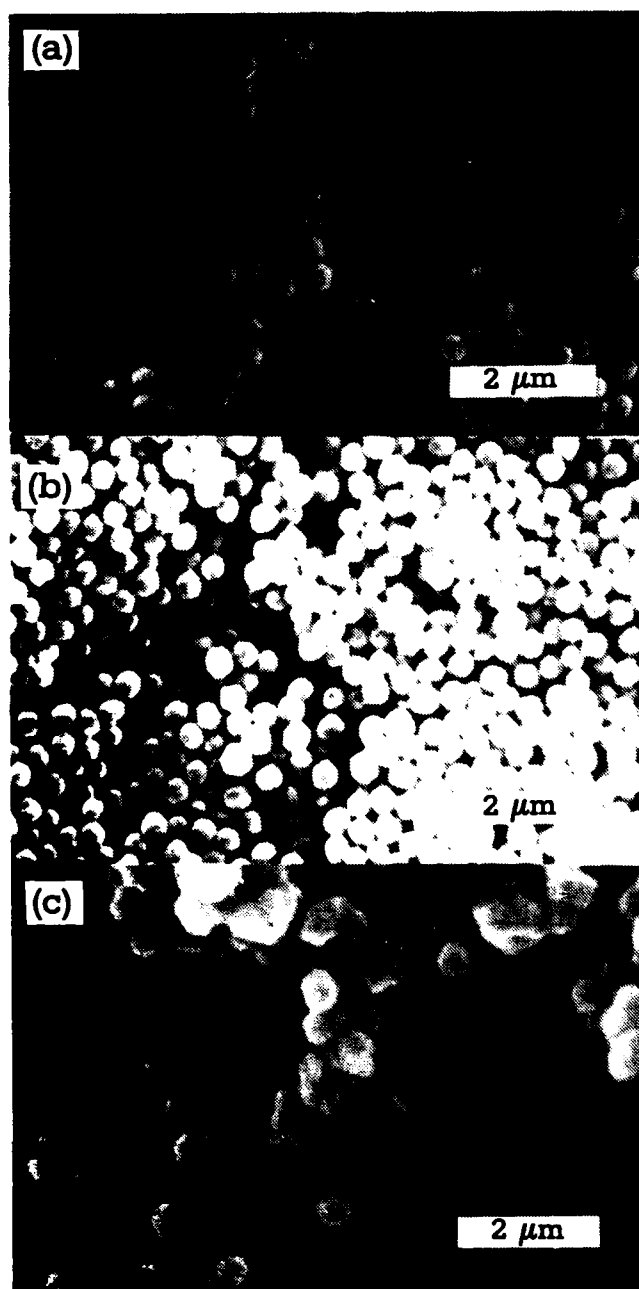


Fig. 1. Scanning electron micrographs of yttria precursor powder prepared by aging aqueous solutions with different concentrations of Y^{+3} , as follows: (a) 0.005 M, (b) 0.025 M, and (c) 0.075 M. [Urea]: 0.270 M. Aging Time: 60 min.

Table 2. The role of $[Y^{+3}]_0$ on the yield and micromorphology

Sample	$[Y^{+3}]_0$	<u>Filtered</u>		<u>Centrifuged</u>	
		% LOI	% Yield Comments	% Yield	Comments
Y7	0.005	37.1	71.6 Spherical, not monosize	99.2	Spherical, dispersed, nearly monosize
Y8	0.010	38.0	79.3 Spherical, dispersed, nearly monosize	95.7	Spherical, dispersed, monosize
Y9*	0.025	37.0	51.4 Spherical, dispersed, monosize	72.3	Spherical, dispersed, monosize
Y10	0.050	36.2	26.8 Spherical, dispersed, monosize	40.4	Spherical, dispersed, monosize
Y11	0.075	34.8	24.4 Spherical, agglomerated	31.4	Nearly spherical, agglomerated
Y12	0.100	37.1	21.1 Irregular shaped, agglomerated	23.2	Irregular shaped, agglomerated

* Represents benchmark sample, i.e., $[Y^{+3}] = 0.025$ M, [urea] = 0.27 M, aging time = 60 min.

Table 3. Influence of [urea] on the yield and micromorphology

Sample	[Urea]	<u>Filtered</u>		<u>Centrifuged</u>	
		% LOI	% Yield Comments	% Yield	Comments
Y13	0.027	36.5	10.2 Plate-like, irregular	13.6	Plate-like
Y14	0.054	33.8	13.7 Spherical, agglomerated	15.6	Spherical, dispersed, monosize
Y15	0.108	34.6	27.9 Spherical, weakly, agglomerated	28.1	Spherical, dispersed, monosize
Y9*	0.270	37.0	51.4 Spherical, dispersed, monosize	72.3	Spherical, dispersed, monosize
Y16	0.405	37.4	79.5 Spherical, dispersed, monosize	87.9	Spherical, dispersed, monosize
Y17	0.540	34.9	82.4 Spherical, large, agglomerates	98.4	Spherical, dispersed, monosize
Y18	0.810	35.5	90.8 Spherical, monosize	98.4	Spherical, dispersed, monosize

* Benchmark sample.

The increase in yield by filtration separation is less than that observed in centrifugation, indicating that recovery in filtration is incomplete. The yield approached theoretical values of $[\text{urea}]/[\text{Y}^{+3}] \approx 30$ for the centrifugation method. Loss on ignition in this series was also more or less constant, ranging between 33.8 to 37.4%, which supports the idea of an invariable precursor composition. The micromorphologies of the precursors obtained in this set of experiments are also described in Table 3, and selected examples are presented in Figure 2. Electron micrographs indicate that when the $[\text{urea}]/[\text{Y}^{+3}]$ fell below 3, particle shape deviated from spherical, and, as the ratio approached 1, the particle became plate-like and irregular. Particle size in this case did not seem to follow a simple trend, and, as will be discussed later, size may have been controlled by other variables more effectively than by the urea concentration.

Study of the yield data in Tables 2 and 3 shows that the yield increased with increasing $[\text{urea}]/[\text{Y}^{+3}]$ ratio. The variation of yield with this ratio for both filtered and centrifuged samples is given in Figure 3. Data from the filtration curve fall onto the same curve with the exception of sample #Y7. The lower-than-expected yield may be explained by incomplete recovery, more specifically, in each experiment a small amount of precipitate was either retained by the filter membrane or passed through to the filtrate. This amount may not be significant for other samples, but in the case of Y7, it represented a substantial fraction of the total precipitate.

The influence of aging time on yield was investigated on standard sample Y9. Time of aging was varied from 10 minutes to six hours; the results are summarized in Table 4. As the aging time increased, the yield increased up to 2 hours, above which a decrease was observed, followed by an increase again at 6 hours. At the present time, the cause of this anomalous behavior is unknown. The shape of the particles remained spherical for all aging periods (see Figure 7). Also, as the aging time increased, the size of the spheres increased, supporting the assumption made earlier that the number of nuclei is constant throughout the process.

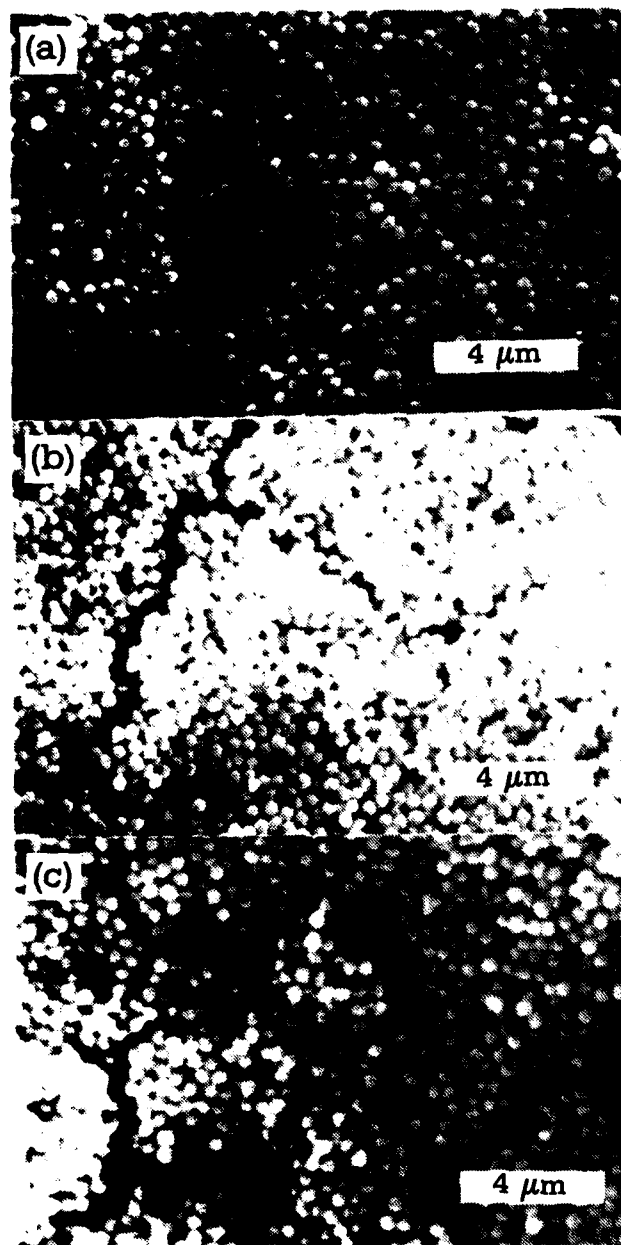


Fig. 2. Scanning electron micrographs of yttria precursor powder prepared by aging aqueous solutions with different amounts of excess urea, as follows: (a) 0.054 M, (b) 0.405 M, and (c) 0.810 M. Initial $[Y^{*3}]$: 0.025 M. Aging time: 60 min.

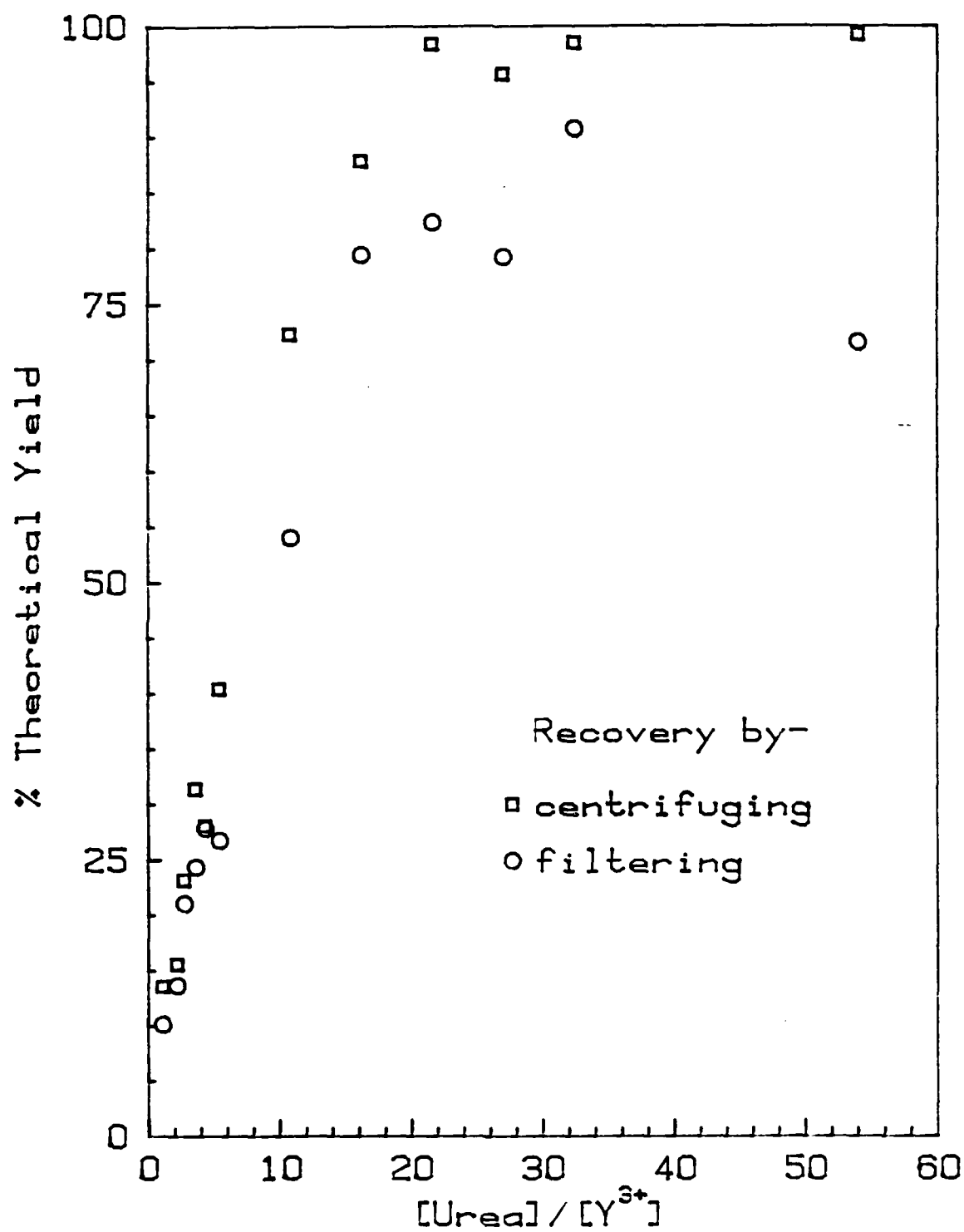


Fig. 3. Plot of % theoretical yield vs. $[\text{urea}]/[\text{Y}^{3+}]$ for both filtration and centrifugation recovery.

Table 4. Influence of aging time on the yield and micromorphology

Sample	Time, min.	<u>Filtered</u>		<u>Centrifuged</u>	
		% Yield	Comments	% Yield	Comments
Y19	10	17.3	Spherical, size distribution	18.0	Spherical, small size distribution
Y20	30	23.3	Spherical, size distribution	40.2	Spherical, dispersed
Y9*	60	51.4	Spherical, dispersed monosize	72.8	Spherical, dispersed monosize
Y21	90	63.1	Spherical, small size distribution	92.1	Spherical, dispersed monosize
Y22	120	NA	Spherical, size distribution	80.2	Spherical, dispersed monosize
Y23	240	67.0	Spherical, large size distribution	72.6	Spherical, dispersed
Y24	360	72.0	Spherical, small size distribution	99.2	Spherical, dispersed-smaller, attached spheres present

* Benchmark sample.

3.2 Effect of Anions on the Micromorphology

Numerous studies on homogeneous colloid sol preparation show that selection of anions is very crucial in development of micromorphology (1). The phenomena are complex and depend on the particular system and experimental conditions so that no generalities can be drawn. In some cases, the supporting anion may act as a weak base, thus monitoring the pH of the medium (as in the case of acetate, carbonate, and phosphate anions); in others it complexes the cation in varying strengths, which, in turn, controls the concentration of free cations that can participate in solid phase formation (as in the case of metal-organic complexes); yet in some other cases, anions may participate in the solid phase in a very pronounced way to control the micromorphology (as in the case of sulphate and phosphate anions).

In the benchmark procedure, nitrate was used as the cation supporting anion. Since nitrate is known to be noncomplexing and a very weak base, the morphology of the particles formed was not expected to be influenced by the nitrate anions. To check this assumption, a similar anion, i.e. chloride ion, was substituted for nitrate. Particles obtained from chloride-supported solutions are shown in Figure 4b. Obviously, both nitrate and chloride ions were indifferent for purposes of particle formation, and as such, they should not be present in the solid phase. This will be discussed in the next section.

The influence of acetate (CH_3COO^-) ion on the micromorphology is shown in Figure 4c. Obviously, acetate altered the morphology drastically. The exact nature of the acetate participation is not obvious. The first assumption in the selection of acetate ion was that its complexing ability would make it possible to form uniform particles at much higher concentrations. Apparently, acetate not only complexes the yttrium ions in the solution, but may in fact participate in the solid phase, or since it is a conjugate base of a relatively weak acid, it may buffer the solution at a lower pH (~4.7) than nitrate does (~6.0). The role of acetate anion in

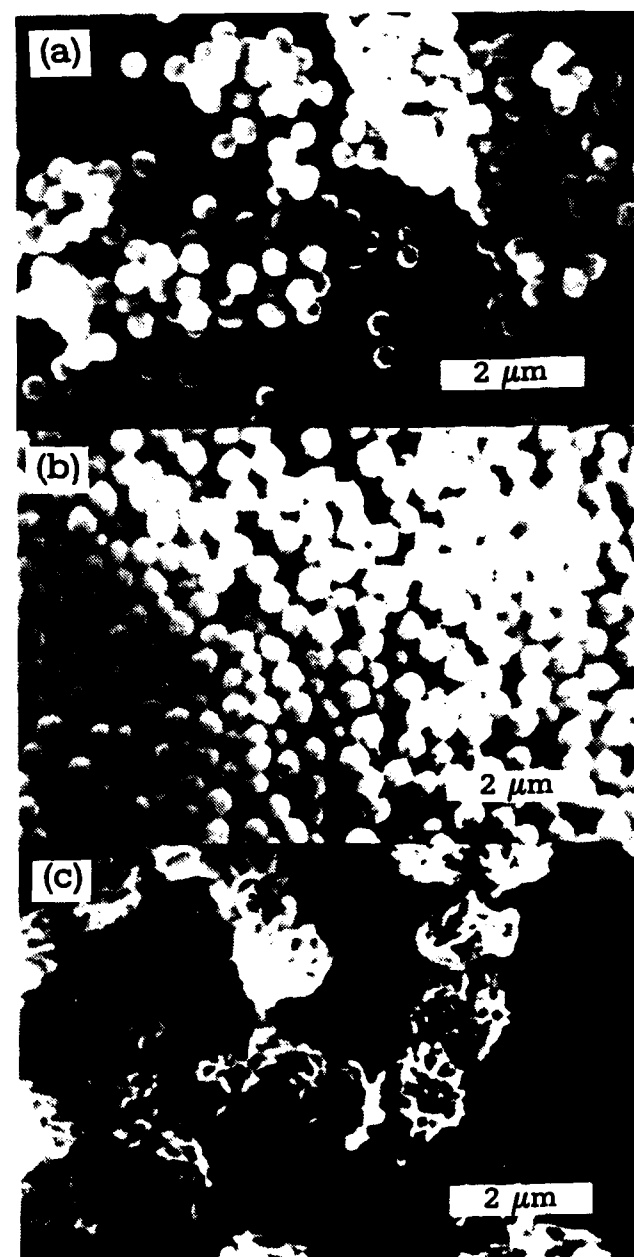
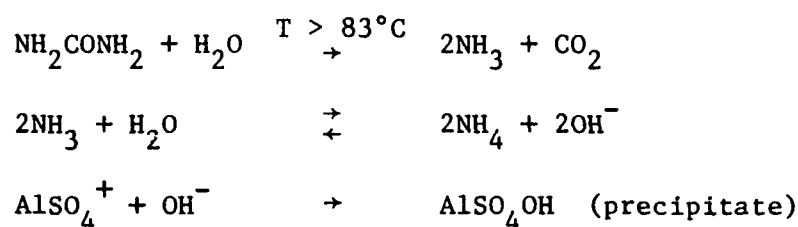


Fig. 4. Scanning electron micrographs of yttria precursor powder prepared by using different supporting anions, as follows: (a) nitrate, (b) chloride, and (c) acetate. Experimental parameters are same as standard, Y9.

influencing powder morphology is very interesting and requires further investigation. Due to constraints and priorities of this project set previously, investigations into these phenomena have not been pursued as yet.

3.3 Chemical Composition of the Precipitate

Previous work (8-10) on homogeneous precipitation of aluminum basic sulfate particles by aging of aqueous urea solutions has shown that the precipitate has an approximate composition of AlSO_4OH , and that the formation of the solid phase is governed by the controlled generation of hydroxide ions by the decomposition of urea. The chemical equations representing solid phase formation may be summarized as follows:



An analogous series of chemical reactions were proposed earlier (6) for the formation of yttria precursors from yttrium nitrate and urea solutions. In this case, since nitrate is not as strong a complexing ion as sulfate, it was assumed that precipitated particles would be merely $\text{Y}(\text{OH})_3$. Yield and loss on ignition values reported in the previous section implied that the precipitate is not a simple hydroxide. Furthermore, hydroxide should precipitate at $\text{pH} \geq 6.4$, but during homogeneous precipitation, the pH remains around 6. This observation also suggests that the precipitate is more complex than simple hydroxide.

The chemical analysis of the precursor particles is as follows:
Y: 49.84%, total C: 6.5%, N (as NH_3): 0.06%, N (as NO_3): 0.5%,
LOI: 36.7%. It is clear that the nitrate or ammonium ions are not
important constituents in the solid phase. When the chemical analysis
is combined with the charge neutrality requirement, the chemical
composition of the precursor particles appears to have the form:
 $\text{YOHCO}_3 \cdot 0.3\text{H}_2\text{O}$. The coefficient of water is determined by difference
and accounts for 3% of the total mass. This value is within the
limits of fluctuations observed in loss on ignition, therefore, one
may conclude that the presence of this molecular water in the solid
phase structure is not fully justified. It may either arise from
experimental error in loss on ignition determinations or from entrap-
ment of water in the structure during precipitation. Hydroxycarbonates
of yttrium and rare earths are not uncommon (11-12). Ancykite type
 YOHCO_3 crystals have been synthesized at elevated temperature and
pressures (14).

Impurity analyses for precursor and oxide particles are shown
in Table 5. Most of the impurities are within acceptable range
except for sample A (this sample did not exhibit monosize, spherical
morphology). Further investigations into this matter showed that
the stock solution of yttrium was badly contaminated. The source of
contamination of that particular stock solution is unknown, but it
is most likely that it originated with the water used in its prepara-
tion. Changing the cartridge on the water deionization unit solved
the problem. Using all glass or polymeric ware does not seem to
influence the impurity levels measurably (see Table 5). Calcined
powder exhibits higher Al and Si than the corresponding precursor.
It is believed that the impurity is picked up from the crucible used
in calcining. In future work, yttria calcination crucibles will be
employed to eliminate this source contamination.

Table 5. Impurities in yttria precursor powders

PPM WT.				
Element	A	B	C	D
Na	9.6	7.6	0.36	4.8
Mg	2.7	3.4	0.17	1.3
Al	200.0	0.53	0.42	3.9
Si	970.0	74.0	40.0	160.0
P	5.5	0.26	0.22	4.5
S	13.0	4.7	3.5	36.0
Cl	12.0	1.1	1.9	36.0
K	0.6	0.13	0.15	2.1
Ca	7.9	1.2	1.0	8.1
Fe	7.0	8.2	3.0	94.0
Ni	1.1	0.32	---	11.0
La	1.2	0.39	0.21	3.8

A: First 3200 ml batch sent to GTE, 4/9/86.

B: Prepared in all plastic ware.

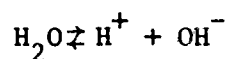
C: Stock solution prepared in teflon precipitated in glass.

D: Same as (c), but calcined.

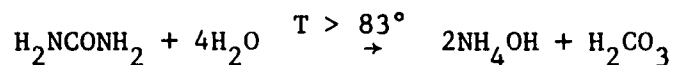
3.4 Mechanism of the Precipitation Reaction

As discussed in the previous section, precursor particles have a chemical composition of approximately YOHCO_3 . Apparently carbon dioxide evolved from hydrothermal decomposition of urea participates in the solid phase formation. The chemical reactions occurring during the homogeneous precipitation process may be quite complex. The following set of chemical equations summarizes the pertinent reactions that occur (15):

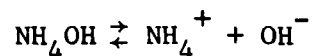
I. Dissociation of water:



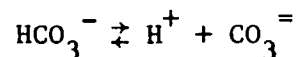
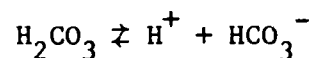
II. Decomposition of urea:



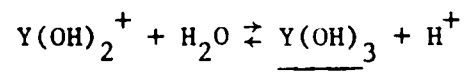
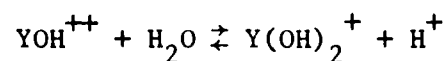
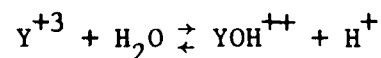
III. Dissociation of ammonium hydroxide



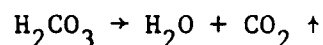
IV. Dissociation of carbonic acid:



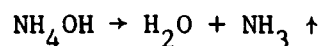
V. Hydrolysis of yttrium ion:



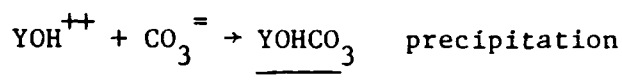
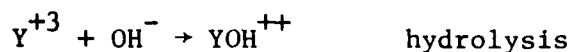
VI. Evaporation of carbon dioxide:



VII. Evaporation of ammonia:

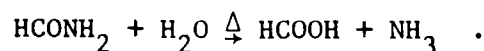


These equations are by no means all inclusive. In fact, it is known (16) that polynuclear yttrium hydroxy species form to some extent, depending on the pH of the medium. Furthermore, carbonates in the form of basic or normal may and do in fact form (13, 17). Based on the chemical analysis of the precursor and the fact that initial stock solution had a pH of about 4 to 5 and increased only to 6 on aging, a simple set of chemical reactions may be written as follows:



Unlike the precipitation of aluminum ions with urea, where hydroxide generated by decomposition of urea plays the critical role, in the case of yttrium ion precipitation, it appears that carbonate ions control the precipitation. It is interesting to note that the equilibrium ratio of $[\text{CO}_3^{=}]$ to $[\text{CO}_2]$ in aqueous solutions around $\text{pH} \approx 6$ is on the order of 10^{-2} or less. This explains, in part, why so much excess urea is needed to precipitate all the yttrium.

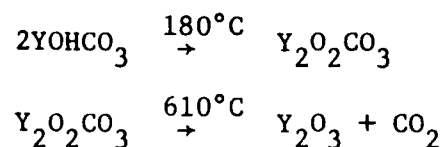
To check the validity of the above mechanism, i.e., whether CO_2 evolution controls the precipitation or not, urea was replaced with formamide (HCONH_2). Formamide decomposes to produce ammonia and formic acid according to the following reaction:



No precipitate was observed with highly-excess formamide solutions over a prolonged boiling period. This result demonstrated that evolution of NH_3 and hence presence of OH^- is not sufficient for precipitate formation. In another experiment to determine whether evolution of CO_2 is necessary for precipitation, urea was replaced with trichloroacetic acid (CCl_3COOH), and the initial pH of the solution was adjusted with ammonium hydroxide. Heating this solution with yttrium stock solution caused effervescence of CO_2 around 70-80°C and immediate precipitate formation. The morphology of the particles was completely different, however (see Figure 5). Probably the rate of decomposition of trichloroacetic acid was much higher than that of urea in this experiment. The morphological differences between urea and trichloroacetic acid derived precursors needs further investigation.

3.5 Thermal Decomposition of the Precursor

Simultaneous TGA/DTA traces of a representative YOHCO_3 sample are given in Figure 6. The differential thermogram showed two distinct endothermic peaks. The first peak appeared at 180°C and was relatively broad with a shoulder around 100°C. The second peak was very sharp and occurred at 610°C. The first peak is believed to be due to decomposition of hydroxycarbonate to oxycarbonate, and the second to transformation to the oxide by the following reactions:



Thermogravimetric data shows that the calcination of this precursor may be carried out as low as 700°C. Studies of the effect of calcination temperature on agglomerate strength have shown that (18) agglomerates become stronger only at temperatures above 1000°C, and substantial neck growth is realized at about 1200°C.



Fig. 5. Scanning electron micrograph of yttria precursor powder prepared via trichloroacetic acid thermal decomposition.

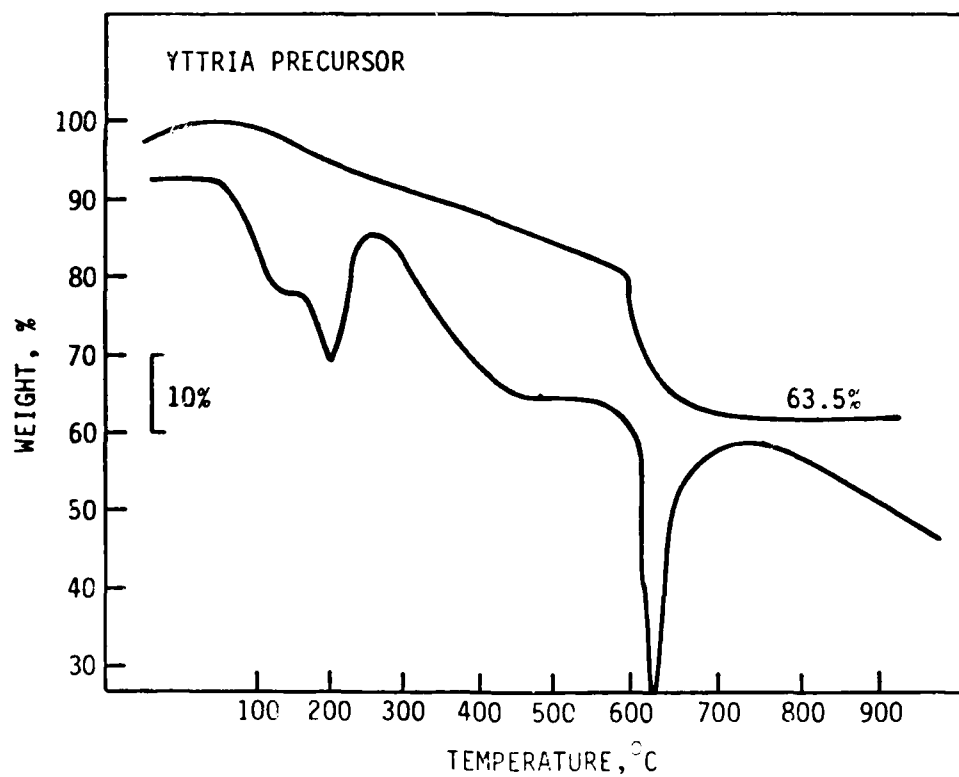


Fig. 6. TGA/DTA for a representative yttria precursor sample.
Heating rate: 20°/min.

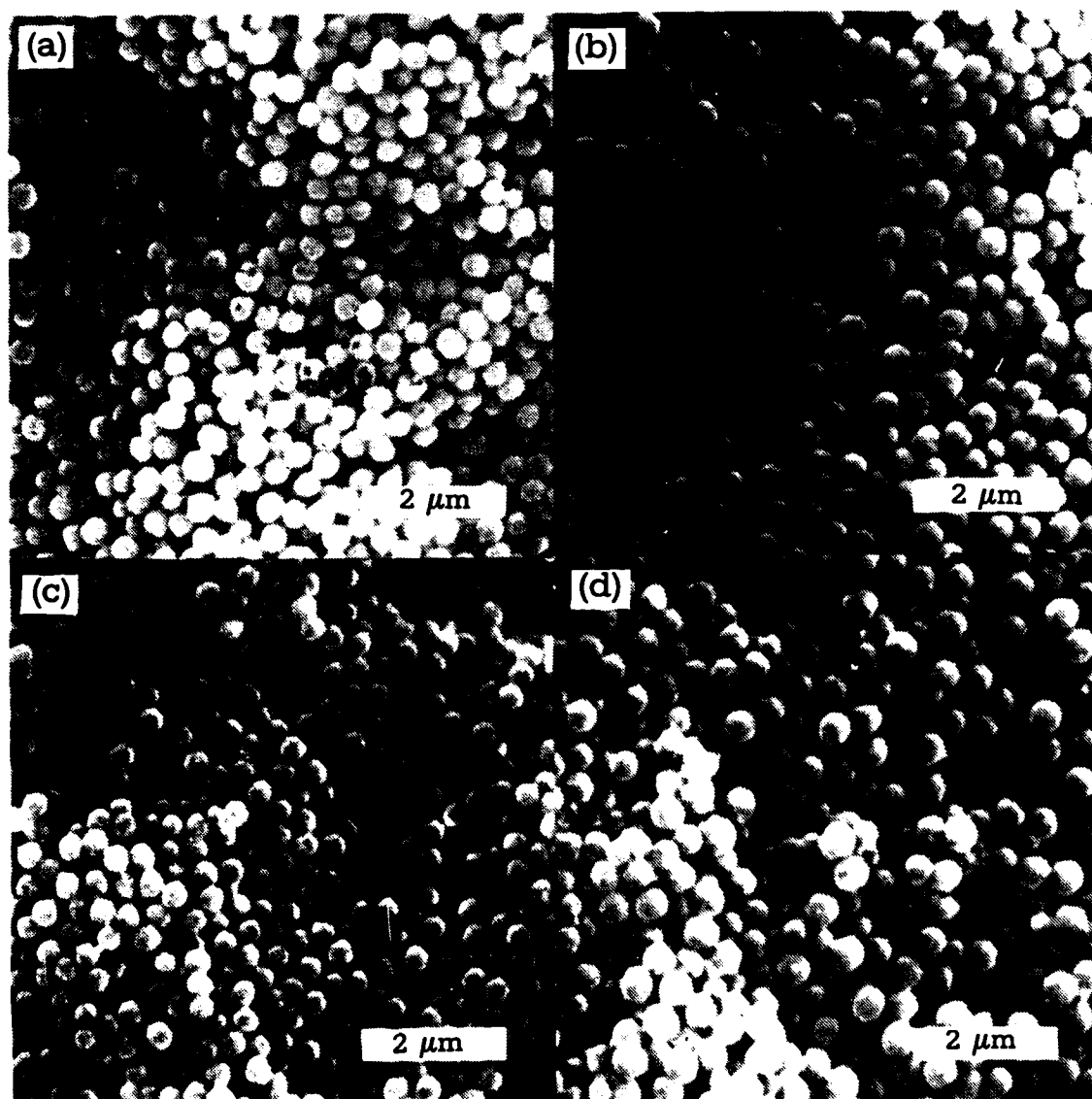


Fig. 7. Scanning electron micrographs of yttria precursor powder prepared from an aqueous solution consisting of 0.27 M urea and 0.025 M Y^{+3} aged for (a) 30 min, (b) 90 min, (c) , 240 min, and (d) 360 min.

3.6 Packing and Sintering Studies

Previous studies (19) on sintering of yttria indicate that measurable densification occurs at temperatures as low as 1200°C. There is also considerable evidence that powder compacts may achieve nearly full densification at temperatures around 1500°C (20).

Only a limited number of packing and sintering experiments were carried out during this reporting period, as most of the sintering work is to be carried by GTE Labs. Figure 8 shows the compacts obtained from centrifugal casting of oxide powders from aqueous suspensions containing 10% Darvan #7 at pH = 7.2. Compacts did not exhibit any significant ordering, yet they appeared to be agglomerate free and uniform. The size of the voids was on the order of the individual particle size (Figures 8a and b). Figure 9 shows the compact prepared from a dispersion having a pH of 8.4. The top surface of the compact is similar to one obtained at pH = 7.4. Apparently, this compact was contaminated by rather large, irregularly shaped impurities during the preparation. The bottom surface of the compact exhibited ordered regions. Figure 8 also demonstrates that a sintering temperature of about 1475°C may produce fully dense material under the proper conditions. Grain size ranged between about 1 to 3 μm . Much work remains to be done in the study of the low temperature sintering behavior of these monosize powder compacts. However, initial observations are extremely promising. It is expected that GTE Labs will continue to work on compaction, sintering and annealing of these monosize powder assemblies to produce transparent useful shapes.

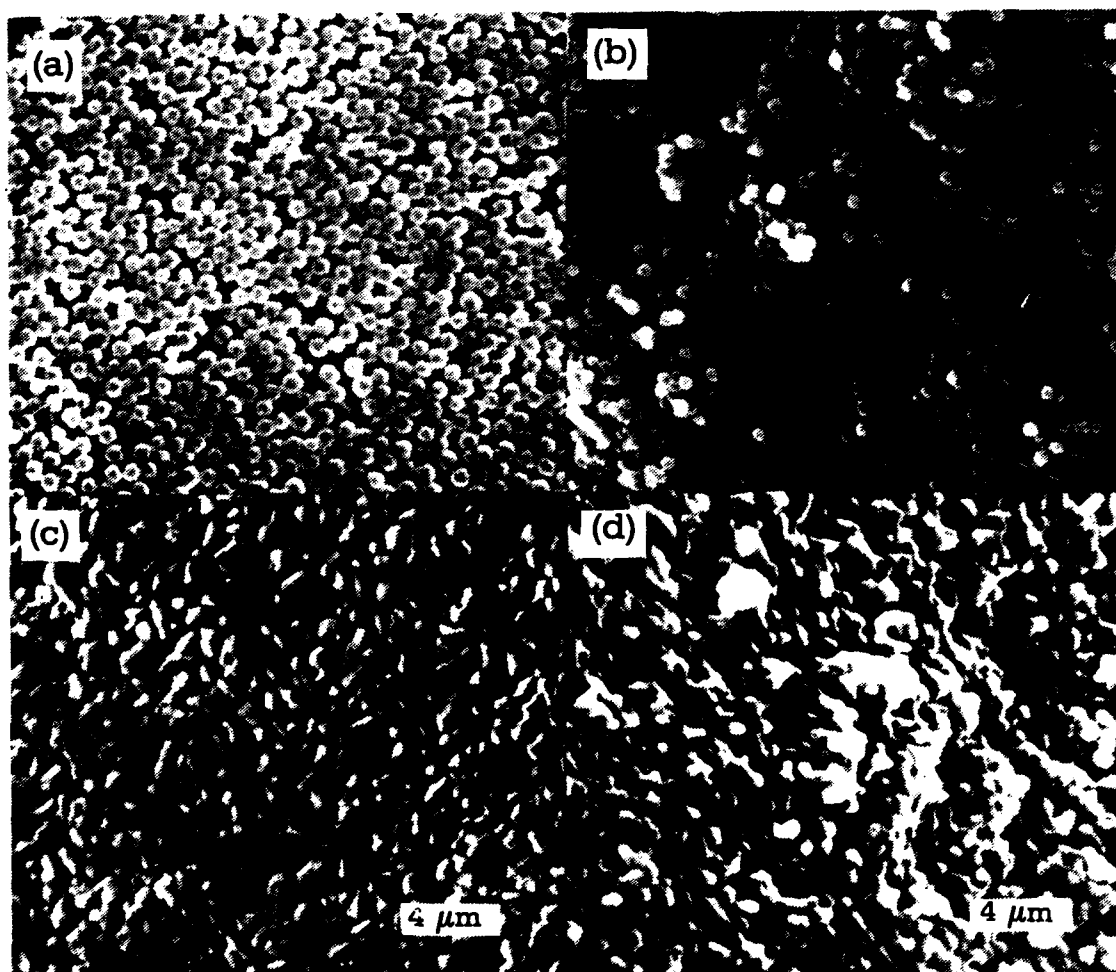


Fig. 8. Scanning electron micrographs of green compacts of Y_2O_3 powder formed by centrifuging an aqueous solution of pH 7.2 with 10% Darvan 7. (a) Top surface, (b) fracture surface, and (c) and (d), top and fracture surfaces, respectively, of compact sintered 180 min at 1475 °C.

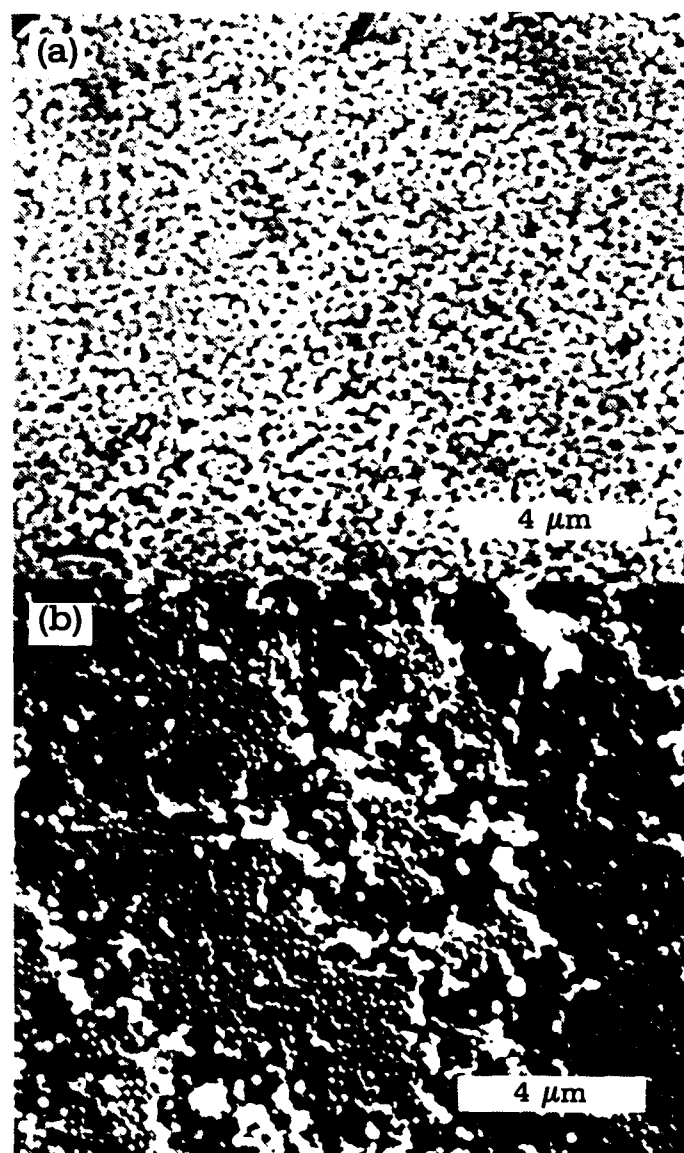


Fig. 9. Scanning electron micrographs of green compacts of Y_2O_3 formed by centrifuging an aqueous solution of pH 8.4 with 10% Darvan 7. (a) Top surface and (b) bottom surface.

4. COOPERATIVE EFFORTS WITH GTE

During the course of this study, the close cooperation that was planned with GTE Labs was realized. Impurity analyses of the powders were carried out by GTE along with some thermogravimetric and microscopic work. These efforts were quite helpful in locating the contamination source and its remedy. Several yttria powder batches were prepared and sent to GTE during this period. A large batch of lanthana-doped yttria powder is being prepared for GTE at the time this report is being written.

During this research period, Dr. W. H. Rhodes and Ms. E. Trickett visited our laboratory for discussions and progress evaluation. Ms. Trickett spent several days in our laboratory and participated in powder preparation and characterization studies.

5. CONCLUSIONS

This research resulted in the following conclusions:

1. Powders of monosize ($\sim 0.4 \mu\text{m}$), spherical shape were produced consistently, as long as reasonable care was exercised to ensure that solutions were contamination free.
2. Increasing urea concentrations increased the yield of the process to nearly theoretical values with no deterioration of the particle morphology.
3. Yttrium ion concentration could be doubled to 0.05 M without any deviation from the monosize, spherical, well-dispersed morphology. Higher yttrium ion concentrations resulted in deviation from sphericity, and caused agglomerate formation.
4. Increasing aging times improved the process yield significantly up to 2 hours.
5. By increasing urea concentration to 0.54 M, aging time to 90 minutes and scaling the total solution volume to 3200 ml, the recovery of the process per batch was increased over an order of magnitude, making it possible to produce large amounts of powder without deteriorating the morphology.
6. Particles formed were found to be amorphous to x-rays and to have a chemical composition of approximately YOHCO_3 . The precursor underwent a two-stage decomposition to form first $\text{Y}_2\text{O}_2\text{CO}_3$ at 180°C followed by another reaction around 590°C to form cubic Y_2O_3 .
7. It was found that a crucial step in the precipitation process is the evolution of CO_2 from decomposition of urea. Heating the solution with trichloroacetic acid (which evolves CO_2 upon decomposition but not ammonia) produced a precipitate, whereas formamide (which produces ammonia but not CO_2) did not form a precipitate. A paradigm for precipitate formation was offered, wherein the yttrium ion is first hydrolyzed to form YOH^{++} which further reacts with $\text{CO}_3^{=}$ to form the YOHCO_3 compound.

8. Centrifugally cast small samples were sintered to translucency at temperatures as low as 1475°C, leading to a conclusion that transparent materials could be produced at much lower sintering temperatures with improved packing and sintering procedures.

6. REFERENCES

1. Egon Matijević, "Monodispersed Colloidal Metal Oxides, Sulfides, and Phosphates". Pages 334-352 in Ultrastructure Processing of Ceramics, Glasses and Composites, L. L. Hench and D. R. Ulrich, Eds., John Wiley & Sons, Inc. (1984).
2. B. Fegley, Jr. and E. A. Barringer. Pages 187-197 in Better Ceramics Through Chemistry, C. J. Brinker, D. E. Clark and D. R. Ulrich, Eds., North Holland, New York (1984).
3. E. A. Barringer and H. K. Bowen, "Formation Packing and Sintering of Monodisperse TiO_2 Powders", J. Am. Ceram. Soc. **65** [12], Comm. C-199-201 (1982).
4. W. H. Rhodes, "Controlled Transient Solid Second-Phase Sintering of Yttria", J. Am. Ceram. Soc. **64** [1], 13-12 (1981).
5. W. H. Rhodes and E. A. Trickett, "Processing Studies for Optically Transparent La_2O_3 -Doped Y_2O_3 ", Annual Report #N0014-82-C-0452, July 1983 and 1984.
6. M. Akinc, "Preparation and Characterization of Lanthana Doped Yttria Monosized Powders", Proposal submitted to GTE Laboratories, January 1985.
7. E. Matijević, "Monodispersed Metal (Hydrous) Oxides - A Fascinating Field of Colloid Science", Acc. Chem. Res. **14**, 22-29 (1983), (and references therein).
8. H. Willard and N. Tang, "A Study of the Precipitation of Aluminum Basic Sulfate by Urea", J. Am. Chem. Soc. **59**, 1190-1196 (1937).
9. B. Cornilsen and J. Reed, "Homogeneous Precipitation of Basic Aluminum Salt as Precursors for Alumina", Am. Ceram. Soc. Bull. **58** [12], 1199 (1979).
10. J. Blendell, H. K. Bowen and R. Coble, "High Purity Alumina by Controlled Precipitation from Aluminum Sulfate Solutions", Am. Ceram. Soc. Bull. **63** [6], 797-802 (1984).
11. J. A. K. Tareen and T. R. N. Kutty, "Hydrothermal Phase Equilibria in Ln_2O_3 - H_2O - CO_2 Systems", J. Cryst. Growth **50**, 527-532 (1980).
12. T. R. N. Kutty, M. N. Wiswanathiah and J. A. K. Tareen, "Hydrothermal Equilibria in Nd_2O_3 - H_2O - CO_2 System", Proc. Indian Acad. Sci. **87A** [4], 69-74 (1978).

13. J. Sawyer, P. Caro and L. Eyring, "Hydroxy-carbonates of the Lanthanide Elements", Revue de Chimie Minerale 10, 93-104 (1973).
14. J. A. K. Tareen, M. N. Viswanathiah and K. V. Krishnamurthy, "Hydrothermal Synthesis and Growth of $Y(OH)CO_3$ -ancylite like Phase", Revue de Chimie Minerale 17, 50-57 (1980).
15. M. Akinc, "Preparation and Characterization of Lanthana Doped Yttria Monosized Powders", Proposal Submitted to GTE Laboratories, Inc., August 1985.
16. C. Baes, Jr. and R. Mesmer, The Hydrolysis of Cations, pages 129-138, John Wiley & Sons, Inc., New York (1976).
17. H. Dexpert, M. Lemaitre-Blaise and P. Caro, "Chemistry and Reactivity of the Compounds with Layered Structures in the Ternary Heterogeneous Systems: Rare Earth Oxides-Carbon Dioxide-Water". Pages 758-765 in Reactivity of Solids, J. S. Anderson, M. W. Roberts and F. S. Stone, Eds., Chapman and Hall, London (1972).
18. M. Ciftcioglu, M. Akinc and L. E. Burkhart, "Determination of Agglomerate Strength Distribution of Calcined Yttria Powder Using an Ultrasonic Technique", Am. Ceram. Bull. 64 [3], 439 (1985).
19. E. Kostic and M. M. Ristić, "Investigation in the Sintering of Y_2O_3 Powders in the Temperature Range 1000 to 1400°C", J. Matl. Sci. 7, 1322-1326 (1972).
20. M. D. Rasmussen, M. Akinc and O. Hunter, Jr., "Processing of Yttria Powders Derived from Hydroxide Precursors", Ceramics International 11 [2], 51-55 (1985).

BASIC DISTRIBUTION LIST

Technical and Summary Reports

1985

<u>Organization</u>	<u>Code</u>	<u>Organization</u>	<u>Copies</u>
Defense Documentation Center Cameron Station Alexandria, VA 22314	12	Naval Weapons Center China Lake, CA 93555 ATTN: Code 385	1
Office of Naval Research Department of the Navy 800 N. Quincy Street Arlington, VA 22217 ATTN: Code 431 Code 413	3 1	National Bureau of Standards Washington, DC 20234 Attn: Ceramics Glass and Solid State Science Division Inorganic Materials Division	1 1
Naval Air Development Center Code 606 Warminster, PA 18974 ATTN: Dr. J. DeLuccia	1	Naval Missile Center Materials Consultant Code 3312-1 Point Mugu, CA 92041	1
Commanding Officer Naval Surface Weapons Center 10901 New Hampshire Ave. White Oak Laboratory Silver Spring, MD 20910 ATTN: Mr. W. Messick Code K22	1	Army Research Office P.O. Box 12211 Triangle Park, NC 27709 ATTN: Metallurgy & Ceramics Program Chemistry Program	1 1
Air Force Materials Laboratory Wright-Patterson AFB Dayton, OH 45433 ATTN: Dr. N. Tallan	1	Scientific Advisor Commandant of the Marine Corps Washington, DC 20380 ATTN: Code AX	1
Naval Postgraduate School Monterey, CA 93940 ATTN: Mechanical Engineering Department	1	Army Materials and Mechanics Research Center Watertown, MA 02172 ATTN: Dr. R. N. Katz	1
Naval Air Systems Command JP #1 1411 Jeff Davis Highway Arlington, VA 22202 ATTN: Code 03D	1	Naval Sea Systems Command NC #2 2521 Jeff Davis Highway Arlington, VA 22202 ATTN: Code 05R	1
Space and Naval Warfare Systems Command NC#1 2511 Jeff Davis Highway Arlington, VA 22202 ATTN: Dr. S. Sacks	1	Office of Naval Technology Department of the Navy 800 N. Quincy Street Arlington, VA 22217 ATTN: Code 0712 Code 0725	1 1
Naval Oceans System Center San Diego, CA 92132 ATTN: Library	1	Air Force Office of Scientific Research/NE Building 410 Bolling Air Force Base Washington, DC 20332 ATTN: Electronics & Materials Science Directorate	1
Defense Metals and Ceramics Information Center Battelle Memorial Institute 505 King Avenue Columbus, OH 43201	1		

SUPPLEMENTARY DISTRIBUTION LIST
Optical Ceramics

Dr. H. E. Bennett
Code 38101
Naval Weapons Center
China Lake, CA 93555

Mr. J. Blair
Eastman Kodak Co.
Dept. 144, Hawkeye Plant
901 Elmgrove Road
Rochester, NY 14650

Mr. R. Bradshaw
BMD Systems Command
LEH
P.O. Box 1500
Huntsville, AL 35807

Dr. J. Burdett
Chemistry Department
University of Chicago
Chicago, IL 60637

Dr. R. Gentilman
Raytheon Co., Research Div.
131 Spring Street
Lexington, MA 02173

Dr. A. Harker
Rockwell International
P.O. Box 1085
1049 Camino Dos Rios
Thousand Oaks, CA 91360

Dr. D. C. Harris
Code 3854
Naval Weapons Center
China Lake, CA 93555

Dr. T. A. Hewston
Code 3854
Naval Weapons Center
China Lake, CA 93555

Dr. P. Klocek
Texas Instruments
Advanced E-O Systems
P.O. Box 660246
Dallas, TX 75266

Dr. D. N. Lewis
Code 6360
Naval Research Laboratory
Washington, DC 20375

Mr. C. Martin
BMD-Advanced Technology Ctr
Huntsville, AL 35807

Ms. D. J. Martin
AFWL/ARBE
Kirtland AFB, NM 87117

Dr. P. E. D. Morgan
Rockwell Science Center
1049 Camino Dos Rios
P.O. Box 1085
Thousand Oaks, CA 91360

Dr. S. Musikant
General Electric Co.
Valley Forge Space Center
P.O. Box 8555
Philadelphia, PA 19101

Mr. C. Dale Perry
US Army Missile Command
Redstone Arsenal
Huntsville, AL 35807

Dr. W. Rhodes
GTE Laboratories
40 Sylvan Road
Waltham, MA 02134

Mr. R. Rice
W. R. Grace Co.
7379 Route 32
Columbia, MD 21044

Mr. D. Roy
Coors Porcelain Co.
Golden, CO 80401

Dr. J. Savage
Royal Signals & Radar Establishment
St. Andrews Road
Great Malvern,
WORCS, WR14 3PS
England

Dr. R. W. Schwartz
Code 3854
Naval Weapons Center
China Lake, CA 93555

Mr. W. Tropf
Applied Physics Lab
Johns Hopkins Road
Laurel, MD 20810

S. Wax
Mat'l's Science Office
DARPA
1400 Wilson Blvd.
Arlington, VA 22209

Dr. W. White
Mat'l's Research Lab
Pennsylvania State Univ
University Park, PA 16802

Dr. A. Wold
Chemistry Department
Brown University
Providence, RI 02912

END

DTIC

9-86